DILUTE MAGNETIC SEMICONDUCTOR NANOSTRUCTURES

A Devin Giddings, BSc

Thesis submitted to the University of Nottingham
for the degree of Doctor of Philosophy

June 2008

Dedicated to you.

Abstract

The prospect of a new generation of electronic devices based on the fundamental quantum property of angular momentum, known as spin, has lead to the rapidly developing field of spintronics. It is envisioned that these advanced devices will have significant advantages over traditional charge based electronics in properties such as speed, power consumption and long coherence times.

By combining the properties of magnetics with that of semiconductors, the novel class of materials known as dilute magnetic semiconductors (DMSs) are considered a promising system for exhibiting spintronic functionality. These materials are created by using molecular beam epitaxy (MBE) to incorporate into traditional semiconductors a quantity of transition metal atoms sufficient that ferromagnetism is exhibited. The most widely studied DMS is (Ga,Mn)As which has well characterised behaviour and can be processed using standard III-V fabrication techniques, thus providing an excellent basis for further study.

In this research the properties of (Ga,Mn)As based systems are studied as the material dimensions are reduced to nanometre length scales. Three complementary approaches are used for this purpose. The first is to use ultra-high-resolution electron-beam lithography to construct devices. By being able to selectively remove material, laterally patterned structures can have sizes as small as 10 nm. The second approach is to exploit the atomic layer growth of MBE to allow the construction of epilayers and heterostructures with well defined vertical compositions. Thirdly, a theoretical $\mathbf{k} \cdot \mathbf{p}$ kinetic-exchange model allows the simulation of multilayer structures and an exploration of the parameter spaces available in such materials.

Two systems are considered: lateral nanoconstricted magnetic tunnel junctions and vertically defined magnetic superlattices. The nanoconstrictions are analysed using low temperature magnetotransport techniques and novel anisotropic magnetoresistance (MR) effects are measured. Primarily, tunnelling anisotropic magnetoresistance (TAMR) is observed, demonstrating that it is a generic prop-

erty of ferromagnetic tunnel devices and is therefore of wide interest for other spintronic systems. Secondarily, anisotropic switching behaviour is observed and is interpreted as Coulomb blockade anisotropic magnetoresistance (CBAMR). Additionally, the significance of the processing stages and material properties are highlighted.

The magnetic superlattices are firstly considered on a theoretical basis in order to determine structural parameters in which a new MR effect might be observed. This effect derives from the interlayer exchange coupling (IEC) between the magnetic layers which can either be in parallel or opposed orientations. Based on the calculations, samples are measured using low temperature magnetotransport and magnetometry techniques in order to explore the possibility of some of the dramatic properties predicted in magnetic superlattice structures.

List of publications

Giddings, A. D., O. N. Makarovsky, M. N. Khalid, S. Yasin, K. W. Edmonds, R. P. Campion, J. Wunderlich, T. Jungwirth, D. A. Williams, B. L. Gallagher, and C. T. Foxon, "Huge tunnelling anisotropic magnetoresistance in (Ga,Mn)As nanoconstrictions", *arXiv:0803.3416* (2008).

Giddings, A. D., T. Jungwirth, and B. L. Gallagher, "(Ga,Mn)As based superlattices and the search for antiferromagnetic interlayer coupling", *arXiv:0802.0275* (2008).

Giddings, A. D., T. Jungwirth, and B. L. Gallagher, "Interlayer exchange coupling in (Ga,Mn)As based multilayers", *Phys. Status Solidi C* **3**, 4070-4073 (2007).

Rushforth, A. W., A. D. Giddings, K. W. Edmonds, R. P. Campion, C. T. Foxon, and B. L. Gallagher, "AMR and magnetometry studies of ultra thin GaMnAs films", *Phys. Status Solidi C* **3**, 4078-4081 (2007).

Wunderlich, J., T. Jungwirth, B. Kaestner, A. C. Irvine, A. B. Shick, N. Stone, K.-Y. Wang, U. Rana, A. D. Giddings, C. T. Foxon, R. P. Campion, D. A. Williams, and B. L. Gallagher, "Coulomb blockade anisotropic magnetoresistance effect in a (Ga,Mn)As single electron transistor", *Phy. Rev. Lett.* **97**, 077201 (2006).

Sawicki, M., T. Dietl, C. T. Foxon, S. V. Novikov, R. P. Campion, K. W. Edmonds, K. Y. Wang, A. D. Giddings, and B. L. Gallagher, "Search for hole mediated ferromagnetism in cubic (Ga,Mn)N", in *Physics of Semiconductors: 27th International Conference on the Physics of Semiconductors*, volume 772, edited by José Menéndez and Chris G. Van de Walle, 1371-1372 (Flagstaff, Arizona, USA: AIP, 2005).

Novikov, S. V., K. W. Edmonds, L. X. Zhao, A. D. Giddings, K. Y. Wang, R. P. Campion, C. R. Staddon, M. W. Fay, Y. Han, P. D. Brown, M. Sawicki, B. L.

Gallagher, and C. T. Foxon, "Mn doping and *p*-type conductivity in zinc-blende GaMnN layers grown by molecular beam epitaxy", *J. Vac. Sci. Technol. B* **23**, 1294-1298 (2005).

Foxon, C. T., S. V. Novikov, L. X. Zhao, K. W. Edmonds, A. D. Giddings, K. Y. Wang, R. S. Campion, C. R. Staddon, M. W. Fay, Y. Han, P. D. Brown, M. Sawicki, and B. L. Gallagher, "Molecular Beam Epitaxy of p-type cubic GaMnN layers", *J. Cryst. Growth* **278**, 685-689 (2005).

Edmonds, K. W., S. V. Novikov, M. Sawicki, R. P. Campion, A. D. Giddings, L. X. Zhao, K. Y. Wang, T. Dietl, C. T. Foxon, and B. L. Gallagher, "*p*-type conductivity in cubic (Ga,Mn)N thin films", *Appl. Phys. Lett.* **86**, 152114 (2005).

Giddings, A. D., M. N. Khalid, T. Jungwirth, J. Wunderlich, S. Yasin, R. P. Campion, K. W. Edmonds, J. Sinova, K. Ito, K.-Y. Wang, D. Williams, B. L. Gallagher, and C. T. Foxon, "Large tunneling anisotropic magnetoresistance in (Ga,Mn)As nanoconstriction", *Phy. Rev. Lett.* **94**, 127202 (2005).

Khalid, M. N., S. Yasin, A. D. Giddings, J. Wunderlich, R. Campion, K. Edmonds, C. T. Foxon, D. Walliams, and B. Gallagher, "Fabrication of nanoconstriction to study the change in magnetoresistance of a (Ga,Mn)As strip as a function of constriction size", in *Digest of Papers: Microprocesses and Nanotechnology 2004* 166-167 (Osaka, Japan: Japan Society of Applied Physics, 2004).

Novikov, S. V., K. W. Edmonds, A. D. Giddings, K. Y. Wang, C. R. Staddon, R. P. Campion, B. L. Gallagher, and C. T. Foxon, "*P*-type conductivity in cubic GaMnN layers grown by molecular beam epitaxy", *Semicond. Sci. Technol.* **19**, L13-L16 (2004).

Acknowledgements

Many people were involved in this research. I would like to thank the following:

Without the support of my supervisors, Bryan Gallagher and Tomas Jungwirth, none of this work could have happened.

All the materials were grown by Richard Campion and Tom Foxon.

The lithography and much of the magnetotransport measurements were carried out under the guidance of Jörg Wunderlich and Mohammad Kahid of the Hitachi Cambridge Laboratory (HCL) and Shazia Yasin of the Microelectronic Reseach Centre, both based in the Cavendish Laboratory, Cambridge.

Support with characterisation, transport measurements and magnetometry were provided by Kevin Edmonds, Oleg Makarovsky and Andy Rushforth.

Much of the theoretical work was done at the Institute of Physics, Academy of Sciences of the Czech Republic.

Tunnelling transport simulations were provided by Jairo Sinova of the Texas A&M University and micromagnetic simulations were provided by Kenchi Ito of HCL.

The x-ray characterisation was performed by Sven Cornelissen of Eindhoven University and Chris Staddon.

Hall bar samples were prepared by Jas Chauhan.

Useful discussions were had with Lawrence Eaves, Mike Sawicki of the Polish Institute of Physics and David Williams of HCL.

Finally, I would like to thank the other students in the group: Adam Freeman, Victoria Grant, Jackie Hall, Chris King, Kai-You Wang, Jeanho Yang and Lixia Zhao.

Contents

List of Figures

List of Tables

Chapter 1

Introduction

1.1 Preface

A new era of quantum electronics was initiated in 1988 with the discovery of giant magnetoresistance (GMR) (Baibich *et al.*, 1988; Vélu *et al.*, 1988; Binasch *et al.*, 1989). For this, Albert Fert and Peter Grünberg were awarded the Nobel prize for physics in 1997. The great significance of the GMR effect is that it showed that the electrical resistance of a material could be altered by manipulating the spins of its carriers. In contrast, in conventional electronics carrier transport depends on charge state irrespective of spin; the spin possessed by carriers is by-and-large evenly distributed between being in up or down states, that is to say, the carriers are unpolarised. GMR found immediate application in magnetic sensor technology, and in less than a decade from its discovery the technology was being widely used in hard disk drive read heads. The field of research that has grown up around the idea of spin based transport is known by the abbreviation spintronics.

Spintronics promises to offer several key advantages over traditional charge based devices. These include improved speed, reduced power consumption and increased levels of device integration (Wolf *et al.*, 2001), enhancements continually sought by the electronics industry. However, the potential of spintronics extends much further than that. Spin can be manipulated by magnetic and electric fields, and also optically. By exploiting spin-polarisation to combine diverse fields such as semiconductor electronics, magnetoresistive effects and optoelectronics, it may be possible to realise a new paradigm of multifunctional devices such as non-volatile programmable logic (Prinz, 1998) and may even provide an avenue

to the elusive quantum computer (Gupta *et al.*, 2001).

Although the size of modern transistors is well below 100 nm (Peercy, 2000), the physics involved remains essentially classical (Devoret and Schoelkopf, 2000). However, at these tiny length scales quantum effects do play a role, but are undesired and entirely detrimental. Most notably, quantum tunnelling results in leakage currents (Taur *et al.*, 1997), which increase the power requirement and heat generation of a device, and, if unchecked, can prevent a device from operating. As sizes become smaller these obstacles become greater, and ultimately provide a limit to the extent of this technology. Since spin is a quantum effect, spintronics, in contrast to traditional electronics, works because of, rather than in spite of, quantum mechanics, and so provides a way to move beyond the established models. There is therefore considerable synergy between nanoelectronics and spintronics.

Because a ferromagnet represents an intrinsic imbalance in carrier spin states, it seems a logical place in which to consider spintronic effects. Indeed, GMR was discovered in ferromagnetic multilayer structures. However, almost all modern electronics are based on semiconductor technology. Therefore, there is considerable interest in having a ferromagnetic material that is compatible with existing semiconductor technology (Ohno, 1998). To this end, a new class of materials known as dilute magnetic semiconductors (DMSs) were developed. These are created by incorporating into a traditional semiconductor a quantity of transition metal atoms. As a result, these materials can exhibit both ferromagnetic and semiconductor properties and so provide a system with a rich phenomenological playground in which to study spintronic effects.

1.2 Thesis

The proposition explored in this monograph is that, whilst harnessing conventional semiconductor fabrication techniques, the size of DMS devices can be reduced to nanoscale lengths in order to observe spin based phenomena. The novel effects that can be observed in these nanostructures may be of interest for future spintronic functionalities. (Ga,Mn)As, being the mostly widely studied and characterised DMS, is used as the basis for this research.

The term nanostructure has a fairly broad definition, but generally is considered to refer to an arrangement smaller than microscopic but larger than atomic. The definition of nanodevice that shall be used in this research is something

with a length-scale below 100 nm. In order to achieve this order of magnitude, two routes for creating nanostructures will be utilised. Firstly, laterally defined nanostructures can be created through high-resolution lithography. Secondly, molecular beam epitaxy (MBE) growth allows the creation of heterostructures with well-defined vertical compositions.

The structure of this monograph is thus: in Chapter 2 the techniques for fabrication, via high-resolution electron-beam lithography, of lateral nanostructures will be described. Chapters 3 and 4 give an account of the measurements on nanoconstriction based devices created using these lithographic techniques. Chapter 5 sets out a theoretical study of a (Ga,Mn)As based superlattice. Based on the parameters suggested by these simulations, superlattices are examined in Chapter 6. Finally, Chapter 7 provides a summary of the results that have been found and gives a suggestion for a future experiments. Full lists of the abbreviations and notation used throughout can be found in Appendices A and B, respectively.

The rest of this chapter will now be devoted to introducing in further detail the concepts underpinning this work.

1.3 Background

1.3.1 (Ga,Mn)As

Although there are a number of different magnetic semiconductors, in the short time since its invention (Ga,Mn)As has become the most popular and widely studied for a number of reasons. Firstly, it is based on the world's second favourite semiconductor, GaAs, and as such is readily compatible with existing semiconductor technologies. Secondly, many DMSs, such as the majority of those based on II-VI semiconductors, are only paramagnetic (Furdyna, 1988). (Ga,Mn)As, on the other hand, is ferromagnetic, and hence exhibits hysteretic magnetisation behaviour. This memory effect is of importance for the creation of persistent devices. A third key feature of (Ga,Mn)As is that not only do the manganese atoms provide a magnetic moment, each also acts as an acceptor, making it a p-type material. The presence of carriers allows the material to be used for spin-polarised currents. In contrast, many other ferromagnetic DMSs are strongly insulating (Ohno *et al.*, 1992; Pinto *et al.*, 2005) and so do not possess free carriers. When all these factors are taken together, (Ga,Mn)As appears to be an exceptionally good candidate as a spintronic material.

Growth

In order to appreciate the technical challenges involved in creating good quality (Ga,Mn)As it is useful to consider the technique by which it is grown, MBE. At its most basic level MBE is a form of vacuum evaporation. Molecular beams are produced through the evaporation of liquids or sublimation of solids, and these are directed at a heated substrate (Foxon and Joyce, 1981). On reaching the substrate the resultant flux is incorporated into the growing crystal. In order to ensure the purity of growth, and that the molecular beams are able to arrive at the substrate without collision, the growth must be performed under ultra high vacuum conditions. As a result, MBE is a complex process requiring expensive specialist equipment.

Another advantage of the high vacuum conditions used in MBE is that it allows an analytical technique known as reflection high-energy election diffraction which can precisely measure growth rates *in-situ*. The rate is interpreted from oscillations in the measured diffracted intensity during the growth, which correspond precisely to the monolayer deposition rate (Joyce *et al.*, 1987). Additionally, this technique allows evaluation of surface crystallography to check that the resultant crystal is being created layer-by-layer, in what is known as a two-dimensional growth mode (Joyce and Joyce, 2004). Shutters between the growth chamber and the molecular beam sources allow for rapid changes in the composition of the resulting flux. Growth rates are low in comparison to the time it takes to turn on or off a specific molecular beam. When this is combined with precise knowledge of the growth rates, it becomes possible to create ultra-thin epilayers or complex heterostructures with well defined interfaces (Foxon, 1994).

Like other DMSs, (Ga,Mn)As is formed by doping a standard semiconductor with magnetic elements. In (Ga,Mn)As the manganese substitute into gallium sites in the GaAs crystal and provide a magnetic moment. Because manganese has a low solubility in GaAs, incorporating a sufficiently high concentration for ferromagnetism to be achieved proves challenging. In standard MBE growth, to ensure that a good structural quality is obtained, the temperature the substrate is heated to, known as the growth temperature, is normally high, typically $\sim 600°$C. However, if a large flux of manganese is used in these conditions, instead of being incorporated, segregation occurs where the manganese accumulate on the surface and form complexes with elemental arsenic atoms (DeSimone *et al.*, 1982). This problem was overcome using the technique of low temperature MBE. It was found, first in (In,Mn)As (Munekata *et al.*, 1989) and then later used for

(Ga,Mn)As (Ohno *et al.*, 1996), that by utilising non-equilibrium crystal growth techniques larger dopant concentrations could be successfully incorporated. At lower temperatures, around 250°C, there is insufficient thermal energy for surface segregation to occur but still sufficient for a good quality single crystal alloy to form (Ohno, 1998).

In addition to the substitutional incorporation of manganese, low temperature MBE also causes the inclusion of other impurities. The two other common impurities are interstitial manganese (Yu *et al.*, 2002) and arsenic antisites (Grandidier *et al.*, 2000). The former is where the manganese atom sits between the other atoms in the zinc-blende lattice structure and the latter is where an arsenic atom occupies a gallium site. Both impurities act as double donors, removing the holes provided by the substitutional manganese, and as such they are known as compensating defects. The interstitial manganese also bond antiferromagnetically to substitutional manganese, removing the magnetic moment. Both these defects are detrimental to the ferromagnetic properties of the (Ga,Mn)As, and so are undesired (Sadowski and Domagala, 2004).

The temperature below which the transition from paramagnetism to ferromagnetism occurs is known as the Curie temperature, T_C. Theoretical predictions based on the Zener model suggest that the Curie temperature scales with the quantity of manganese, so T_C above 300 K is possible if manganese doping levels as high as 10% can be achieved (Dietl *et al.*, 2000). After its discovery by Ohno *et al.* (1996), the highest reported Curie temperatures in (Ga,Mn)As rose from 60 K to 110 K (Ohno, 1998). However, despite the predictions of room temperature ferromagnetism, no improvements in T_C were made for several years.

As a result of this lack of progress, predictions started to be made that 110 K was in fact a fundamental limit for (Ga,Mn)As. The self-compensating nature of the defects would limit the possible hole concentrations, preventing further gains in T_C (Yu *et al.*, 2003). The major breakthrough came from improvements in post-growth annealing. By using annealing temperatures comparable to the growth temperature it was possible to pass the 110 K barrier (Edmonds *et al.*, 2002a; Chiba *et al.*, 2003a; Ku *et al.*, 2003). These improvements have been attributed to the removal the highly mobile interstitial manganese (Edmonds *et al.*, 2004).

Currently, the highest reported values of T_C in (Ga,Mn)As are around 173 K (Wang *et al.*, 2005a; Jungwirth *et al.*, 2005), still well below the much sought room temperature. As a result, measurements on this material must be done at cryogenic temperatures, currently precluding any application outside of the

laboratory. Naturally, considerable effort is being spent in the search for an alternative DMS that does not share this limitation (Matsumoto *et al.*, 2001; Reed *et al.*, 2001; Han *et al.*, 2002; Saito *et al.*, 2003; Sharma *et al.*, 2003). In addition to this, as MBE techniques and equipment are refined and improved it is hoped that greater control over growth conditions will allow further incremental advances in the Curie temperature of (Ga,Mn)As.

Properties

Regardless of the fact that room temperature ferromagnetism has not yet been achieved, DMS materials such as (Ga,Mn)As, have shown considerable success. Thanks to the rich interplay of physics inherent to DMSs a variety of novel phenomena and device structures have been demonstrated. It is therefore instructive to make a critical review of these main developments.

A key result in DMS technology is gateable ferromagnetism, where an electric field is used to control the ferromagnetic properties. This was achieved by Ohno *et al.* (2000) using an insulating-gate field-effect transistor with (In,Mn)As as the magnetic channel. The magnetic properties were inferred from magnetisation dependent Hall measurements of the channel. Using the gate action to either deplete or accumulate holes in the channel it was possible to change the characteristic of the Hall response to be either that of a paramagnet or of a ferromagnet. When the temperature of the sample was close to its T_C it was possible to turn the ferromagnetism on or off by applying a gate voltage which could change the T_C by ± 1 K.

A similar (In,Mn)As transistor device was used to provide further examples of gateable ferromagnetism (Chiba *et al.*, 2003b). In this experiment the electric field was used to modify the coercive field at which magnetisation reversal occurs. As a result of the dependence of the magnetic hysteresis on the gate bias the electric field could be used to assist magnetisation reversal or even demagnetise the ferromagnetic material. The combining of magnetic and electronic functionality demonstrated by this experiment is one of the goals of spintronics and may be expected to have a great technological impact.

Another important spintronic functionality that has been demonstrated in DMSs is that of spin injection. This is where the high spin polarisation inherent to these magnetic materials is used to transfer spin polarised carriers into a non-magnetic material (Ohno *et al.*, 1999). In this example, a fully epitaxial heterostructure

was used where spin polarised holes were injected from a (Ga,Mn)As layer to an (In,Ga)As quantum well where they combine with unpolarised electrons from an n-type substrate. A polarisation of 8% was measured in the resulting electroluminescence. This is again of potential technological interest as it shows the possibility that the spin states in non-magnetic semiconductors can be manipulated without the application of a magnetic field.

(Ga,Mn)As offers an excellent material to study domain wall mechanics because the domains can have a size of the order of 100 µm (Fukumura *et al.*, 2001). Several studies have been done in which lithographically defined lateral constrictions (Honolka *et al.*, 2005) or other pinning points (Holleitner *et al.*, 2005) are used to manipulate domain walls. These experiments are crucial to understanding domain wall nucleation and propagation which would be necessary for the creation of complex logic circuits based on domain wall mechanics (Allwood *et al.*, 2005). Many properties of domain walls are still not fully understood and one particularly outstanding issue is of the magnitude and size of the resistance associated with current passing through domain walls. Both positive (Chiba *et al.*, 2006) and negative (Tang *et al.*, 2004) values of domain wall resistance have been reported, leaving this an open area for future research.

An example of a simple device that utilises pinned domain walls is provided by Rüster *et al.* (2003). This experiment consisted of a lithographically defined narrow island connected to the leads via a pair of nanoconstrictions. While the device operated in a diffusive regime the constrictions would pin domain walls, resulting in a GMR signal. The properties when the device operates in a tunnelling regime will be discussed in Chapters 3 and 4.

A further interesting property of domain walls is that of current induced domain wall motion. This reversal is believed to occur as a result of the spin-transfer torque exerted by a spin polarised current (Slonczewski, 1996). It was demonstrated by Yamanouchi *et al.* (2004) in a lateral (Ga,Mn)As device containing three regions which had been patterned to have different coercive fields, allowing the easy formation of a domain wall. The central region was designed to have the lowest coercivity so that the application of current pulses could cause the orientation of the magnetisation to be switched. Interestingly, this experiment showed that the current required to achieve this reversal in (Ga,Mn)As was two orders of magnitude lower than that of metal systems. It has also been demonstrated that current-induced magnetisation reversal can occur across a (Ga,Mn)As/GaAs/(Ga,Mn)As vertical tunnel junction (Chiba *et al.*, 2004).

Another novel spintronic effect, which was first observed in (Ga,Mn)As based tunnel devices, is tunnelling anisotropic magnetoresistance (TAMR). This effect arises from the intricate dependence of the tunnelling density of states on the magnetisation, and can result in magnetoresistances (MRs) of several orders of magnitude. This will be discussed in more detail in Chapter 3. Similarly, the dependence of the single electron charging energy on the magnetisation has resulted in another dramatic MR effect. This Coulomb blockade anisotropic magnetoresistance (CBAMR) will be examined in Chapter 4.

There are many excellent review articles about the properties and applications of DMSs and (Ga,Mn)As in particular. If further information is required on the topic, the following publications are recommended: Sarma *et al.* (2003); Gould *et al.* (2007).

1.3.2 Spin-orbit coupling

Because of its importance in understanding spintronic phenomena it is fruitful to describe in some detail the effect known as spin-orbit coupling (SOC). Many effects, including anisotropic magnetoresistance (AMR) (Campbell *et al.*, 1970) and magnetocrystalline anisotropy (Abolfath *et al.*, 2001), originate from the SOC, and so it will be frequently referred to in the following chapters. At the simplest level, SOC is an interaction between the spin angular momentum, $\mathbf{S}$, and the orbital angular momentum, $\mathbf{L}$, of a particle. It originates from a relativistic effect of the Dirac equation. The basic derivation included here is based on that of Griffiths (1995, p. 239-242) and Davies and Betts (1999, p. 118-121).

From the perspective of an electron orbiting a hydrogen atom, the proton will have a circular motion around the electron. The magnetic field, $\mathbf{B}$, generated by the motion of the proton can be given by

$$\begin{aligned} \mathbf{B} &= \frac{1}{4\pi\epsilon_0}\frac{e}{m_e c^2 r^3}\mathbf{L} \\ &= \frac{1}{e m_e c^2}\frac{1}{r}\frac{dV(r)}{dr}\mathbf{L}, \end{aligned} \tag{1.1}$$

where r is the orbital radius of the electron and $dV(r)/dr = e^2/4\pi\epsilon_0 r^2$; $V(r)$ is the potential energy of the electron.

The magnetic dipole moment, $\boldsymbol{\mu}$, of the electron is proportional to the spin angular

momentum, $\mathbf{S}$, with a proportionality factor known as the gyromagnetic ratio. For the electron this relationship is given as

$$\boldsymbol{\mu} = -\frac{e}{m_e}\mathbf{S}. \tag{1.2}$$

The energy associated with the torque from a magnetic dipole, $\boldsymbol{\mu}$, in a magnetic field, $\mathbf{B}$, gives the Hamiltonian

$$\mathcal{H} = -\boldsymbol{\mu} \cdot \mathbf{B}. \tag{1.3}$$

Substituting Equations 1.1 and 1.2 into Equation 1.3 gives

$$\mathcal{H} = \frac{1}{2m_e^2c^2}\frac{1}{r}\frac{dV(r)}{dr}\mathbf{S} \cdot \mathbf{L}. \tag{1.4}$$

This equation is known as the spin-orbit interaction and describes the SOC. Note that there is an additional factor of 1/2 included in Equation 1.4. This factor is called the Thomas precession, and must be included to account for the fact that the analysis was done from the rest frame of the electron, which is accelerating and hence not an inertial frame.

Because of this coupling between the spin and the orbit, when an external field attempts to reorientate the spin of a carrier it also has the effect of attempting to reorientate the orbit. However, in crystalline materials this reorientation is strongly opposed by the coupling between the orbit and the crystal lattice. This is the result of the quenching of the orbital magnetic moment, which keeps the orientation of the orbits tightly bound to the lattice (Cullity, 1972, p. 214). In most materials the SOC is weak in comparison to the lattice-orbit coupling and as a result the energy required to overcome the spin-orbit interaction is low. This energy is known as the magnetocrystalline anisotropy. (Ga,Mn)As, however, has a strong SOC, and so by comparison has a significant magnetocrystalline anisotropy. The SOC is responsible for a host of anisotropic properties such as AMR, which is the transport phenomenon analogous to the magnetocrystalline anisotropy (Jungwirth *et al.*, 2006). By considering the SOCs in the valence band, many of the anisotropic properties of (Ga,Mn)As can be explained and predicted (Dietl *et al.*, 2001b; Abolfath *et al.*, 2001).

1.3.3 Zener kinetic-exchange model

Although there are many complementary models that can be used to describe the origin of ferromagnetism in DMSs, the Zener kinetic-exchange model has been particularly useful in explaining many experimental results. This mechanism was proposed by Zener (1951) in order to provide a description of ferromagnetism in transition metals. It has since been found to provide a poor description because it did not account for the itinerant character of the d electrons nor for the Friedel oscillations of the electron spin polarisation around the localised spins (Dietl *et al.*, 2000). However, the Zener kinetic-exchange has returned to prominence because it provides a good model of carrier mediated ferromagnetism in DMSs where the distance between the carriers is greater than that of the spins (Dietl *et al.*, 2001b).

The Zener model is a mean-field approach that describes ferromagnetism in (Ga,Mn)As through indirect exchange between local d-shell moments of the manganese atoms. This exchange is mediated by the hybridisation between these moments and p-band itinerant carriers. The model can be used to encompass both SOC and the interaction between angular momentum states and the delocalised atomic orbitals described by $\mathbf{k} \cdot \mathbf{p}$ theory, as well as carrier correlation, confinement, weak disorder and antiferromagnetic interactions (Dietl, 2003). The kinetic-exchange mechanism therefore provides a powerful and versatile approach for describing DMSs.

Many experimentally observed properties of (Ga,Mn)As, and other DMSs, have been successfully described or predicted using the Zener kinetic-exchange model. Examples of this include Curie temperatures (Jungwirth *et al.*, 2002b, 2005), the magnetic anisotropies (König *et al.*, 2001), domain structures (Dietl *et al.*, 2001a), anisotropic magnetoresistances (Jungwirth *et al.*, 2003), the effects of strain engineering (Jungwirth *et al.*, 2002a) and other direct current (DC) transport properties (López-Sancho and Brey, 2003; Hwang and Sarma, 2005).

For a comprehensive overview of the theory of ferromagnetic (III,Mn)V semiconductors the review by Jungwirth *et al.* (2006) is highly recommended.

Chapter 2

Lithography and Fabrication

2.1 Introduction

Since the invention of the integrated circuit almost 50 years ago, the ability to miniaturize transistors to build complex logic circuits on a single crystal has been considered magic, even (perhaps especially) by those working within the electronics industry. The driving technology behind the ever-increasing levels of integration required in the fabrication of modern electronics is that of the process of lithography. This technique, whose name derives from the Greek words for stone and writing, was developed in the 18th Century as an artistic method. Today, micro- and the more modern nanolithographic procedures are vastly complicated fusions of physics, chemistry and engineering, allowing transistors to be created on sub-µm length scales. However, modern lithography is no less an art today than it was 300 years ago, and if large scale integration is indeed magic, then nanolithography must surely be the voodoo behind it.

This Chapter gives an overview of the lithographic techniques and processes necessary for the creation of nanostructures. This will provide an insight into the technological limitations and pitfalls in achieving ultra-high-resolution fabrication and, importantly, provide a context in which to consider the experimental lateral nanostructures used in Chapters 3 and 4. Additionally, some of the recipes and "tricks" used, seemingly passed on only by oral tradition, are included for posterity, and it is hoped that this may be of assistance in future fabrication work. This is in no way intended to be a comprehensive review of lithography, but a record of the nanofabrication used for this research and an explanation of the reasoning for specific choices. Fabrication is a rapidly changing field, and

techniques are largely determined by the equipment available. Regardless, the underlying principles are generic, making this of wide interest.

Furthermore, it is becoming apparent that the fabrication techniques themselves can affect the sensitive thin (Ga,Mn)As films that were researched, even to the point of altering the observed anisotropies (Ciorga *et al.*, 2007a). Indeed, in Chapters 3 and 4 it will be noted that the resistivity of post-processed material is greater than that as-grown. Therefore, it is important to focus on the exact processing steps made and to have them recorded for future reference.

2.2 Principles

The purpose of lithography is to make an imprint into a surface by selectively removing material in order to leave only a desired pattern. This is done by creating a mask over the substrate material, and then using a process to remove material which remains unmasked. The action by which the undesired material is removed is known as etching and can be chemical or physical. The mask is called the resist due to the necessity that it must be able to withstand the etching, either wholly or at a reduced rate in comparison to the substrate material that is being removed. When the material has a high resistance to the etch it is known as a hard mask, whilst otherwise it is a soft mask.

Depending on the resist that is chosen the processing stages and expected outcomes may be different. For example different resists require differing post application baking or curing and after exposure some may require post exposure baking to fix the resist. Additionally the developer, which selectively dissolves resist depending on whether it has been exposed, must be chosen appropriately so that the resist-developer system has sufficient sensitivity and resolution for the desired result.

The key to successful lithography is accurately creating the desired pattern in the resist. This is typically done by exposing the resist to a radiation source to which it is sensitive, in a process called exposure. The most common form of exposure is optical lithography, where the resist is irradiated with light of ultra-violet or higher frequency. A newer technique, which offers several key advantages, is electron-beam lithography, where the resist is exposed to a focused cathode ray. This method is very popular for research purposes since it is possible to create electron-beam systems from converted electron microscopes and much higher resolutions can be achieved with this method in comparison with conventional

optical lithography.

If electrical measurements of a device are to be made further lithographic steps are required in which metal contacts for wired connections are made. The process of depositing contacts is known as metallisation. Here, instead of using the resist mask to define where etching is to take place, it is used to define where the metal contacts are to be deposited by evaporation. Unwanted metal is removed by performing a lift-off, which will be discussed later.

During a complete device fabrication there will typically be one or more fabrication stages and one or more metallisation stages, and not necessarily in that order. There are many variables to consider for successful production. Typically these are method of exposure, choice of resist, choice of developer, etching method and the metallisation. Each of these must be compatible and appropriate.

A typical nanofabrication process is illustrated in the chart in Figure 2.1.

All these steps are considered in detail below. For ease of flow, and to mirror somewhat how this might actually be performed, the fabrication steps have been split into two main phases: pre-exposure and post-exposure. The pre-exposure phase considers the resists and resist deposition and the post-exposure phase considers the etching and metallisation.

2.2.1 Pre-exposure processing

The first stage of device fabrication involves coating the chip with resist. The term chip is used to describe a semiconductor wafer that has been scribed into smaller pieces. Industrially, when semiconductor devices are mass produced, the wafers are typically patterned whole and then scribed into chips. For the purposes of this work, however, the wafers were scribed first into 5 mm $\times$ 5 mm pieces due to the stage size requirement of the electron-beam machines.

Although resist deposition may at first seem a trivial step, it is vitally important that it is done accurately for the subsequent lithography to be successful. There are various factors to consider, particularly the choice of resist which will determine how the fabrication is performed and what sort of features it might be possible to create. This section will therefore focus on resists and resist deposition.

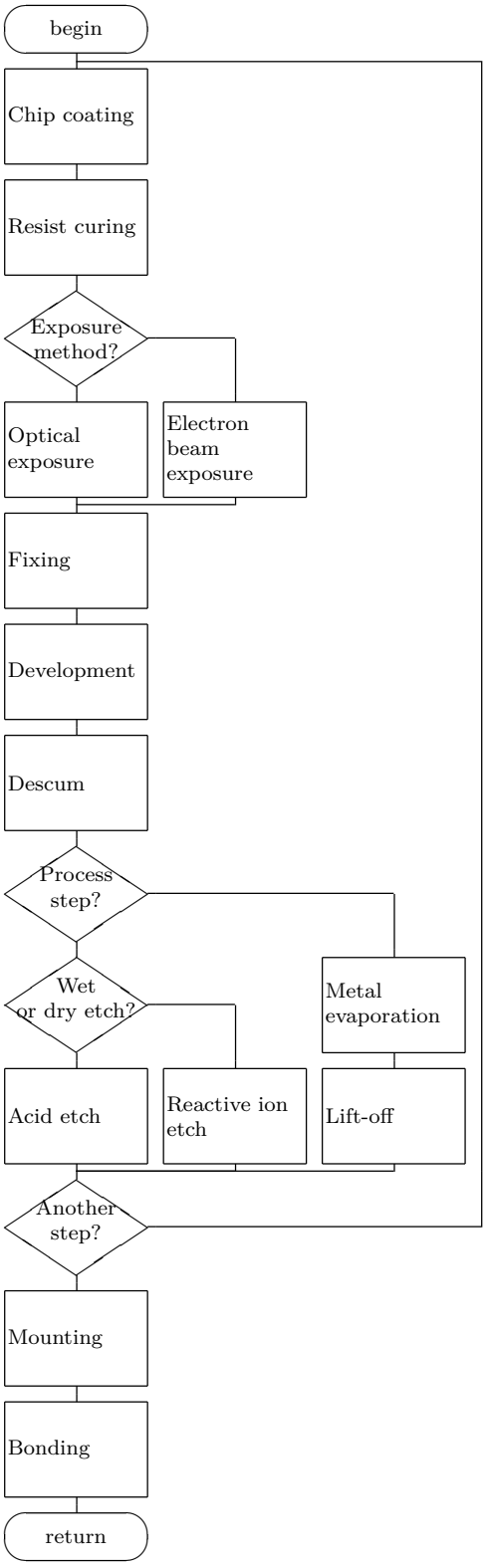

Figure 2.1: Flow diagram illustrating the typical process steps involved in nanostructure fabrication.

Resists

The lithographic exposure does not act on the substrate itself but rather on a reactive layer covering the substrate, the resist. Exposure will cause a change in the solubility of the resist to its developing solution, so by selection of the areas that are exposed, a desired pattern can be created. The type of reaction caused by exposure depends on the resist, but resists are broadly classified into two types, positive and negative.

A positive resist is one which is initially insoluble, but the exposed area becomes more soluble and so can be removed by the developer; this typically is caused by the radiation breaking bonds in the resist. A negative resist is one which is initially soluble, but exposure causes it to become less so. Therefore, the developer can dissolve the unexposed areas and leave only the exposed resist. In this type of resist the incident radiation typically causes a polymerisation reaction.

The two resists mainly used for nanoconstriction fabrication were poly(methyl methacrylate) (PMMA) and UVIII so these will be discussed in detail. Additionally, two alternative resists that were tested will be mentioned as they highlight some important points about the processing procedure.

PMMA The organic positive resist PMMA is widely used for *e*-beam lithography. It comes dissolved in Anisole solvent, the concentration of which is indicated by the A-rating, the percentage by weight of PMMA to Anisole solvent. For example, A8 resist can be diluted to A4 by mixing it with an equal mass of solvent. In addition to coming in different concentrations the PMMA also comes as different types, the two most commonly commercially available are 495 and 950; these numbers refer to the molecular weight, 495k and 950k respectively. These types offer slightly different properties, specifically the higher molecular weight is less sensitive. This can be useful in the application of multilayer resist structures but generally only the 950k is used for high-resolution lithography because of its better resolution.

The thickness of the PMMA layer resulting from spin deposition is dependent on both the concentration and molecular weight. Further details on this are given in the next section. For PMMA a typical post application bake is 120°C for at least an hour. For exposure a typical dosage is 500 $\mu C\,cm^{-2}$ when using a beam current of 60 pA with a spot size of 150 nm. With a smaller spot for small features a larger dose of about 600 or 700 $\mu C\,cm^{-2}$ might be used, while with a large spot

size a 300 $\mu C\,cm^{-2}$ would be sufficient.

The usual developer for PMMA is a methyl isobutyl ketone (MIBK):isopropyl alcohol (IPA) solution. However, in this work a IPA:H_2O solution was used instead. This co-solvent developer gave better sensitivity and contrast than the MIBK:IPA solution, making it favourable for nanolithography (Khalid *et al.*, 2004). The development time of A4 PMMA was about 30 s in 7:3 IPA:H_2O cooled to 20°C.

Although PMMA is usually a positive resist, under very high exposure doses cross-linking between the polymer chains can cause it to act as a negative resist (Zailer *et al.*, 1996). The high dosage involved with this, combined with the associated backscatter and proximity effects, mean that using PMMA in this manner is of little use in high-resolution lithography.

UVIII Another positive resist is UVIII, which is the trade name of chemically amplified resist designed for optical lithography. However, because it is also very sensitive to *e*-beam it offers an excellent alternative to optical lithography when creating low-resolution structures rapidly (Yasin *et al.*, 2005).

Before the UVIII is applied, in order to improve the cohesion of the resist the substrate is primed for 2 minutes in Hexamethyldisilazane (HMDS) vapour. Spin deposition of UVIII at 5000 rpm for 30 seconds should give a thickness of 700 to 800 nm. After the resist is spun on it must be prebaked immediately before exposure for 1 minute at 130°C. A typical exposure dose for low-resolution features is 23 $\mu C\,cm^{-2}$. After exposure the resist must be fixed by heating on a hot-plate at 145°C for 1 minute. Development is with CD26 at 20°C for 1 minute after which it is rinsed with deionised water. This would have to be done carefully as a long exposure to CD26 was found to attack (Ga,Mn)As.

hydrogen silsequioxane (HSQ) The inorganic negative resist HSQ potentially offers sub-10nm resolutions (Baek *et al.*, 2005). Like UVIII, HSQ is developed in CD26 and the sensitivity is similar to PMMA. HSQ also has the interesting additional property that it has a very high etch selectivity and so can be converted to a SiO_2 hard mask (Kretz *et al.*, 2005). However, for the purposes of this research this was not a desirable property. After fabrication with HSQ a residue was left that was extremely difficult to remove.

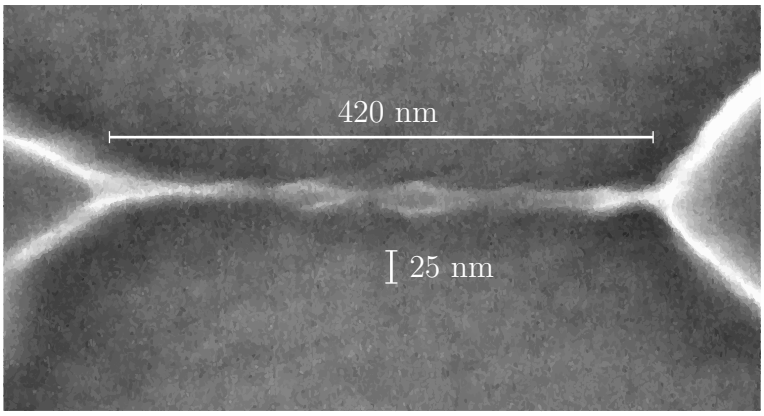

Figure 2.2: An ultra-thin wire created using Calixarene resist.

Calixarene Another negative resist, Calixarene, which describes a family of cyclic phenolic compounds named after their resemblance to a calyx-krater vase (Sailer *et al.*, 2002), can offer very high-resolutions for *e*-beam lithography. However, it has a very low sensitivity compared to PMMA, requiring a much higher dose and a subsequent long exposure time (Ochiai *et al.*, 1999). Several developers are suitable for Calixarene including xylene (Fujita *et al.*, 1996) and MIBK:IPA (Buhlmann *et al.*, 2005). An example of the kind of ultra-thin wire type structure than can be created using Calixarene is shown in Figure 2.2. This wire represents a single line scan of the electron-beam, the width being limited by the spot size.

Despite this very promising result offered by Calixarene, the high dose required by this resist could cause problems. If write times become long then beam drift can become a significant issue, so Calixarene offered a poorer solution when large structures such as side gates were being considered. So, while negative resists excel at making narrow wires, positive resists are better at narrow trenches, more suitable for the structures being considered in this work. Additionally, PMMA works well for writing large areas, offering a good versatility. For these reasons, PMMA would be the resist principally used for the nanofabrication.

Resist deposition

Chip coating It is important that the resist is evenly distributed over the chip's surface so that fabrication will be consistent over the whole chip. In order to achieve this, the resist is dripped onto the chip, which is then spun at high speeds, uniformly spreading the resist over the surface. A speed of 5000 rpm for 30 s is a typical value for spreading resist onto 5 mm $\times$ 5 mm chips.

The thickness of the resist is an important consideration for the fabrication step.

Molar weight	Dilution	Thickness / nm
950k	A8	770
	A4	190
	A2	54
	A1	19
495k	A7	380
	A6	260
	A4	130
	A2	48
	A1	15

Table 2.1: Thicknesses of different PMMA solutions spun onto silicon chips at 5000 rpm for 30 s.

For metallisation the resist typically needs to be thicker in order to accommodate the depth of metal. If the resist is not thick enough for a given metal deposition then the lift-off, the process in which unwanted metal is removed, may not be successful; the metal thickness should be no more than $\frac{2}{3}$ of the resist thickness (Smith, 1974). When etching occurs both the resist and the substrate will be removed at rates determined by their vulnerability to the etching method. This could be a particular consideration for deep etches or where the resist is vulnerable to the etching method. However, making the resist too thick can limit the smallest feature size obtainable, so for high-resolution lithography a thinner resist layer is preferable. The thickness of resist can be tailored by adjusting the rotational speed of the spinner, the length of time of spin and the amount of solvent in the resist mixture. The thicknesses of various PMMA resists, measured using an α-stepper, after being spun onto 5 mm $\times$ 5 mm silicon chips are shown in Table 2.1.

Resist Curing After the resist is spun on it is cured in an oven. The purpose of this pre-exposure bake is to evaporate the solvent and harden the resist. A PMMA resist would typically be cured in an oven for 1 hour at a temperature of 125°C.

2.2.2 Post-exposure processing

Once the resist has been patterned through exposure and subsequent development the next step is to transfer the pattern onto the substrate. There are two primary ways in which this can be done. The first is by using the resist as a mask and

etching away the uncovered material. A common technique for high-resolution lithography is the use an additional hard mask, an intermediate layer between the resist and the substrate with a high resistance to etching. The pattern from the resist is first replicated on the hard mask, and the hard mask is then used to protect the substrate during a second etch. However, in this research due to the added complications of removing a hard mask without damaging the ultra-thin (Ga,Mn)As film, etching was performed directly using the resist as a soft mask. PMMA is particularly vulnerable to plasma etching (Cui, 2005, p. 107) but because the required etch depth was low in comparison to the resist thickness no significant issues would arise from this.

The second pattern transfer technique is metallisation, whereby a metal layer is deposited onto the chip. Where no resist is present the metal sticks to the substrate, but where resist is present the metal is deposited on the resist. The unwanted metal is then removed using a lift-off technique whereby the resist is dissolved in solvent so the metal covering it is removed.

Before either technique is applied it would be usual to "descum" or clean away excess resist in oxygen plasma. This would have the effect of uniformly thinning the resist, and importantly removing any unwanted residual resist remaining after development. This residual resist may not be visible under a microscope (Gritz *et al.*, 2003) but could hamper a uniform etch and is particularly a problem for achieving a clean lift-off. The oxygen plasma would be applied for only brief periods, 60 s or less, so that not too much of the resist is removed.

Etching

Two methods of etching were used, the so-called "wet" etch, which uses acids and the "dry" etch, which uses ion bombardment. Each method has differing advantages; wet etching is very isotropic and so can give a significant undercut while dry etching is more directional.

Wet etching In this study the (Ga,Mn)As layer could be etched with H_2SO_4. Dilute HCl would be used before the etch in order to remove any oxide layer. The etching solution consisted of 1:8:1000 H_2SO_4:H_2O_2:H_2O. For GaAs this etch system offers a slow etch rate of 0.038 µm min^{-1} and a low relative anisotropy for etching between different crystalline orientations (Williams, 1990, p. 105).

The etch rate was tested with two pieces of 25 nm $(Ga_{0.94},Mn_{0.06})As$, shown in

Etch time / s	Resistance / kΩ
0	8
20	14
40	100
60	∞
0	9
50	∞

Table 2.2: Etch rate test for (Ga,Mn)As in dilute H_2SO_4.

Table 2.2. Prior to etching, the samples were first immersed in 1:3 HCl(37%):H_2O for 20 s to remove the oxide layer. Etching was performed using a 1:8:1000 H_2SO_4(98%):H_2O_2(30%):H_2O solution. The samples were held in tweezers and manually stirred during the etching. Because removing and re-immersing the chip will result in a different etch rate in comparison to a continual etch of the same length of time, the first chip was etched in 20 s increments to get an impression of the rate, while the second chip was subject to a continuous etch of 50 s. These data show a good agreement with the published etch rate of GaAs. Subsequently, during actual processing a weaker 1:10 HCl:H_2O solution would be used for oxide removal.

Dry etching There are several dry etching techniques, of which reactive ion etch (RIE) was used in the processing for this research. RIE offers an extremely anisotropic etch where the vertical etch rate far exceeds the lateral rate, resulting in an excellent etch profile with very little undercut (Williams, 1990, p. 186). The gas that was used for this purpose was silicon tetrachloride ($SiCl_4$) which has shown itself to be suitable for high-resolution GaAs fabrication (Stern and Liao, 1983).

An etch test was again carried out on a piece of 25 nm ($Ga_0.94$,$Mn_0.06$)As. Testing showed that after a 35 s etch using $SiCl_4$ the resistance increased from 7 kΩ to 13 kΩ. This was followed by a wet etch of 20 s HCl and 20 s H_2SO_4, after which the magnetic layer was fully etched. Based on the wet etch rate found previously this showed that a 35 s etch would be sufficient to etch a 5 nm layer. An atomic force microscope measurement of a 5 nm ($Ga_{0.94}$,$Mn_{0.06}$)As film that had been dry etched for 35 s showed the etch depth to be 20 nm. Unfortunately, the RIE machines used were seemingly strongly influenced by environmental factors and did not always give very consistent results.

Metallisation

Metallisation is performed for two main purposes. The first is to create alignment marks. By using a metallic layer the contrast of the alignment marks could be greatly improved, making alignment of subsequent lithographic steps significantly easier. The second use of metallisation is to create bond pads, which are large areas to which wiring can be bonded for electrical measurements. Gold is used for both purposes.

Deposition The metallic layers are deposited using an evaporator under ultra-high vacuum. Pieces of high purity metal are heated with a high current so that atoms are emitted from them with a uniform ballistic distribution, resulting in a uniform covering of all surfaces in line-of-site of the source. Deposition could be prevented by placing a shutter between the source and the sample; initial heating of the source would be done with the shutter closed until the rate and pressure had stabilised in order to outgas and remove any surface impurities. The deposition rate and thickness is measured via a piezoelectric crystal and the rate is controlled through the applied current.

To improve adhesion between the gold and the substrate, a wetting layer of chromium is evaporated on first. For alignment marks approximated 10 nm of chromium followed by 30 nm of gold was deposited. The bond pads require thicker metallisation so about 30 nm of chromium followed and 300 nm of gold was used. The deposition rate would initially be kept below 0.3 $\mathrm{nm\,s^{-1}}$ to ensure an even deposition. Other adhesion improving metals such as titanium are a suitable alternative to chromium.

Lift-off Once the sample is covered with a uniform metallic layer the process by which parts of the metal are selectively removed is the lift-off. In this step the sample is immersed in solvent to remove all of the resist. The metallic layers that are adhered to the substrate will remain, whilst the metal layers that were previously on the resist will now become free-standing in the solvent. With some gentle agitation this layer should separate away or lift-off from the sample. Using a pipette was the preferred way to assist the lift-off for this material; ultrasonic assistance could be very effective but it was found that because GaAs is very brittle this should be used only as a last resort for a recalcitrant lift-off. Accurate exposure and development leaving the resist with well defined smooth edges would help the lift-off process immensely.

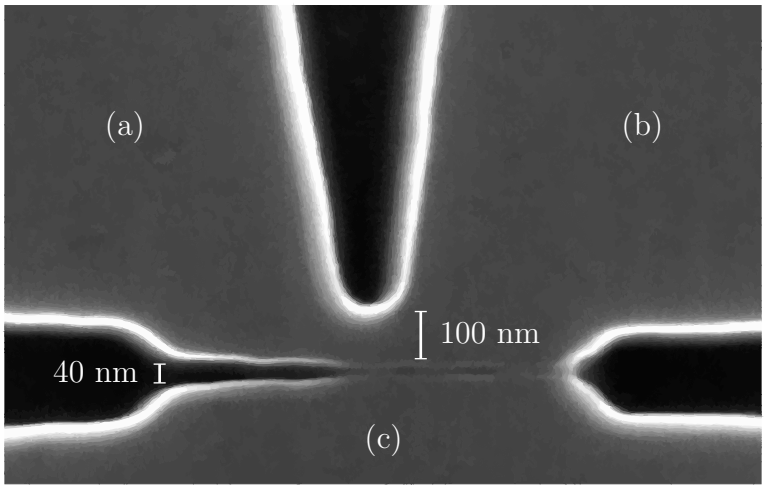

Figure 2.3: SEM micrograph of an attempt at creating a gated nanoconstriction. The dark area has been etched and the lighter area is the unetched (Ga,Mn)As epilayer. (a) is the source, (b) is the drain and (c) is the gate. The constriction has a lateral width of 100 nm, and the gate is separated by a 40 nm channel. Unfortunately, the etch of the channel was only partial, so the gate was not electrically isolated.

Cleaning As a point of record, the solvents used to clean the samples were Acetone followed by IPA. After cleaning a sample would be often be baked at 120°C for at least 5 minutes to dehydrate it, depending on what the next processing stage would be. It is clear that during processing the material would be subject to several exposures to heating.

2.3 Creating nanostructures

Having described the various steps that fabrication involves, the focus shall now be on how specifically the nanoconstriction devices investigated in Chapter 3 were processed. The nanoconstrictions in Chapter 4 were created in an almost identical manner, and represent only a refinement of this process. The exact timings and doses would vary depending on the outcome of the prior stages, and thus be adjusted heuristically in order to achieve the desired result. The values given here are based on those actually used in the processing, which were carefully recorded in contemporaneous notes. As mentioned, it was found that the electron-beam and RIE equipment could be somewhat idiosyncratic, apparently very sensitive to imperceptible changes in conditions.

Creating nanostructures offers two distinct challenges. The first is creating small

structures, where material must be selectively preserved during etching so that a specific design is left. The second is removing selected material to create nano sized gaps. Both of these challenges are shown in the scanning electron microscope (SEM) micrograph in Figure 2.3 which is of a gated nanoconstriction. In such a structure the material to form the constriction must not be etched, while the channel itself needs to be sufficiently etched. As can been seen from the Figure 2.3, this can be difficult to achieve.

A five-stage lithographic process was used to manufacture the nanoconstriction devices. The first stage involved creating the registration marks which are used for determining alignment. This is of vital importance for a multi-staged fabrication process as the alignment of all subsequent exposures would be done relative to those marks. Without these being created accurately it would not be possible to position all the other parts of the device correctly in relation to each other. Also during this stage the optional inner metallic contacts were deposited. The central part of a partly processed chip showing only the inner alignment marks and a Hall bar structure can be seen in Figure 2.4. The second stage was the creation of the bond pads. The third and fourth stages were where the Hall bar and nanoconstrictions were defined. This was performed in two stages due to the disparity in feature size requiring different exposure conditions. The fifth, and final, lithographic step was the creation of isolation trenches between the bond pads. With the exception of the first step, there was some flexibility as to the order in which these stages were done. Due to the fact that metallisation steps could be problematic it was preferable to have these done before creating nanoconstrictions. A full fabricated sample with various features labelled is shown in Figure 2.5.

Also note that the use of many stages is partly a consequence of the limitations of the electron-beam apparatus available. A suite of three machines, each offering different capabilities, with varying spot size, beam current and maximum field size were used. A raster write method was used with a 16-bit DAC, hence in order to ensure smooth features it was necessary to tailor the spot size and field size to the feature size. Therefore, for small features a small working field with a small spot size is needed, while for larger areas a large working field with a wider spot size would be used. The dwell time was automatically calculated by the software controlling the beam. The capabilities of the high-resolution electron-beam system used can be read about in Chen *et al.* (1988).

Although it was possible to use optical methods for low-resolution stages one, two

and four, using only electron-beam exposure had some principle benefits. The first was that photoresist developer MF319 would act as a etchant for GaAs and so also for (Ga,Mn)As. This is not an issue when creating the registration marks since those areas were not functional parts of the device, but it could result in very poor bond pads. An additional disadvantage of this aspect of optical resists is that if the exposure did not go perfectly on the first attempt then the chip would no longer be in a pristine condition for further attempts due to the action of the developer. Through experience it was found that the alignment was better when all stages of lithographic exposure were performed exclusively via *e*-beam.

First stage This stage involved low-resolution lithography and metallisation. The registration marks and inner connects were defined with a low-resolution electron-beam system. Three sets of alignment marks, inner, middle and outer were created for the high-resolution, low-resolution and coarse alignment. Figure 2.5 shows both the inner and middle registration marks, giving a sense of the scale between then. Although the registration marks could be formed by etching only, thereby rolling the first and third stages together, using metal for the registration marks gave a greatly improved contrast making alignment much simpler. PMMA positive resist was used. Low molecular weight (495k) PMMA was spin coated onto the square 5 mm × 5 mm chips for 30s at 5000 rpm followed by high molecular weight (950k) at the same speeds. This gave a resist layer of about 200 nm. The beam diameter, or "spot-size", was approximately 160 nm and the beam voltage was 40 kV. Current of 100 pA and a dose of 325 $\mu C\,cm^{-2}$ was used for all features except the inner registration marks which were exposed with 350 $\mu C\,cm^{-2}$. If a lower current of 50 pA was used then a smaller spot-size of 120 nm could be achieved. Development was for 30 s in a 7:3 IPA:H_2O solution at a temperature of 20°C. Prior to deposition, the sample was put in oxygen plasma for 1 minute to remove any unwanted resist. Metallisation was performed via evaporation. 15 nm chromium was deposited first as a wetting layer to improve cohesion, followed by 40 nm of gold.

Second stage During this stage the bond pads were defined. These were large features so UVIII resist was used as it requires a lower dose, thus allowed a higher throughput. It was spun on at 5000 rpm for 30 s, giving a resist thickness of about 800 nm. Prior to spinning, the chips were immersed in HMDS vapour for 3 minutes to improve the adhesion of the resist. Exposure was with a beam current of 1 nA and a dose of 23 $\mu C\,cm^{-2}$. Development was performed using

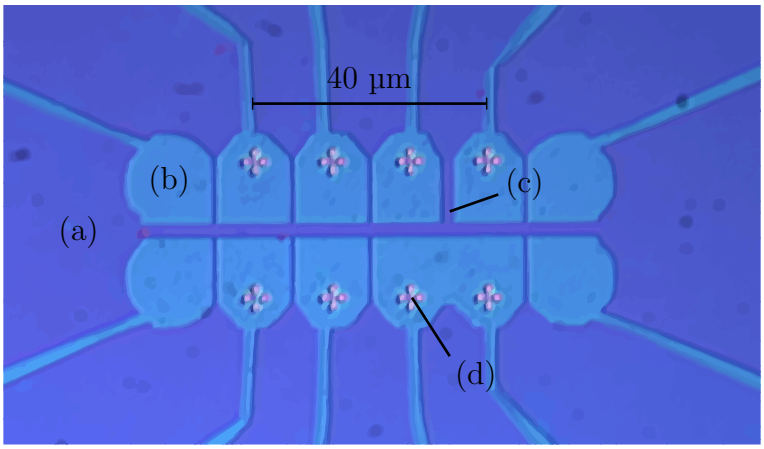

Figure 2.4: Optical microscope image of a device in the middle of the second stage of processing. The Hall bar structure has been exposed and the PMMA resist developed, but it is not yet etched. The darker coloured parts, such as (a), are the remaining resist, and the lighter coloured parts, such as (b), have had the resist removed. This wider leg, labelled as (c), of the bar was intended to be used for a side-gate. The inner registration marks from the first fabrication stage are labelled as (d). This device has no inner metallised connects.

CD26 at a temperature of 20°C for 60 s. Oxygen plasma for 60 s was used to remove residue resist immediately prior to evaporation. The metal layer was deposited via evaporation and had a thickness of 27 nm of chromium and 280 nm of gold. The deposition rate was 0.2 nm per minute for the first 10 nm, and then 0.6 nm per minute for the rest. For later chips PMMA A8 would be used instead of UVIII due to the potential problems with CD26. In this case a 4 nA current and a dose of 300 µC cm^{-2} would be applied. The very high current was in order to minimise writing times. Development was for 30 s in a 7:3 IPA:H_2O solution at a temperature of 20°C.

Third stage In this stage the Hall bar and inner isolation trenches are defined. The chip was coated in high molecular weight (950k) PMMA resist via spin deposition at 5000 rpm for 30 s. The exposure conditions were similar to the first stage. After the exposure the chips were developed and etched. Development was, as usual, 30 s in a 7:3 IPA:H_2O at a temperature of 20°C. Oxygen plasma was applied for 30 s prior to a dry etch for 20 s in an $SiCl_4$ plasma.

Fourth stage In this stage the high-resolution features such as the nanoconstrictions or lateral gates were defined. As with the third stage, 950k PMMA was used as the resist. With the high-resolution *e*-beam machine it was possible

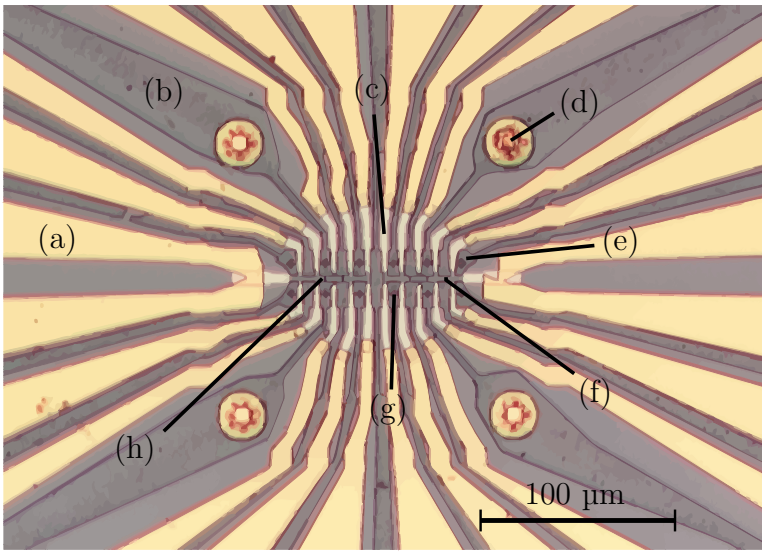

Figure 2.5: Optical microscope image of a complete nanostructure device. The labelled components are (a) bond pad, (b) outer isolation trench, (c) inner metal connect, (d) middle registration mark, (e) inner isolation trench, (f) Hall bar, (g) inner registration mark, and (h) a nanoconstriction. The middle registration marks are obscured by a second layer of gold since they are exposed when they are used for alignment of the second metallisation stage.

to achieve a spot diameter of 12 nm at an accelerating voltage of 70 kV. The dosage was varied from 500 to 750 $\mu C\,cm^{-2}$ depending on the feature size aimed for; smaller feature sizes would have higher doses. After exposure the sample was developed for 30 s in 7:3 IPA:H_2O solution at a temperature of 20°C. After development the resist was cleaned with oxygen plasma for 6 s and the features were etched using RIE with silicon tetrachloride ($SiCl_4$) gas for 12 s.

Fifth stage The final stage was to create the trenches around the bond pads so that they would be electrically isolated. Again, A4 PMMA resist was used, spun on at 5000 rpm for 30 s. As these were very coarse features a large spot size, about 400 nm, and a high current, 2 nA, could be used. The dose was 450 $\mu C\,cm^{-2}$. In order to speed up this process the current could be increased to 4 nA at which the smallest achievable spot size was about 500 nm. Such a low-resolution was not a problem as the features were relatively very large and it did not matter if the edges were rough. As before, this was developed in 7:3 IPA:H_2O solution at a temperature of 20°C. The etching method was not important as the trenches were not functional parts of the device; their creation could be performed with either wet or dry methods.

Chapter 3

Ultra-thin Films and Nanoconstrictions

3.1 Introduction

In metallic based systems nanocontact devices have been used to demonstrate MR effects of several orders of magnitude (García *et al.*, 1999; Hua and Chopra, 2003), although the origin of this MR is controversial. As a candidate for future spintronic functionality there is, unsurprisingly, considerable interest in the properties of DMSs, such as (Ga,Mn)As, as the lateral dimensions are reduced to nanoscale lengths. The epitaxial nature by which (Ga,Mn)As is grown readily lends itself to the creation of vertical devices with discrete well defined layers with sizes from several nanometres in the growth direction. Vertical tunnel junction devices created in this manner have already been used to demonstrate large MR effects (Tanaka and Higo, 2001; Chun *et al.*, 2002).

In addition to vertical devices, by utilising high resolution electron-beam lithographic techniques, as described in Chapter 2, it is possible to fabricate structures with lateral dimensions of sub-100 nm lengths. The first successful application of this in (Ga,Mn)As was reported by Rüster *et al.* (2003), in which lithographically defined nanoconstrictions were fabricated each side of a thin, and comparatively long, island. In this experiment the authors believed that the magnetisation reversal of the island and the leads were controlled by their shape anisotropy; the geometry of the island caused it to have a higher coercive field than the leads. However, it now seems probable that the higher coercivity was due to uniaxial strain relaxation (Wenisch *et al.*, 2007). When the transport through

the nanoconstrictions was in the Ohmic regime MR effects of up to 8% were reported. This was interpreted as a GMR effect, whereby domain walls became pinned at the nanoconstrictions, increasing the spin scattering of carriers and thus the resistance.

When the size of the nanoconstrictions was reduced in size to sub-10 nm the device entered a non-Ohmic transport regime and a much larger MR was observed, reaching sizes of $\sim 2000\%$. This was interpreted as a tunnelling magnetoresistance (TMR) effect in which the nanoconstrictions acted as tunnel barriers, magnetically decoupling the island and the leads. Instead of being due to scattering at domain walls, the large observed MR was due to variations of the magnetisation either side of the constriction, changing the tunnelling probability through it (Rüster *et al.*, 2003).

There has been further interest in (Ga,Mn)As tunnel junctions as result of the discovery of a novel effect, the so-called TAMR. This was first discovered in a normal-metal/insulator/ferromagnetic semiconductor (Au/AlOx/(Ga,Mn)As) vertical tunnelling device (Gould *et al.*, 2004). The new TAMR effect offered a rich phenomenology in which both normal and inverted spin-valve-like features could be exhibited with respect to the applied field orientation and temperature. The effect was explained as arising from the anisotropies in the (Ga,Mn)As density of states (DOS), caused by the strong SOC inherent in this material, as a function of the magnetisation orientation. The tunnelling is dominated by a small range of k states close to the Fermi energy which have a complex dependence on the magnetisation (Gould *et al.*, 2004). Therefore, as the magnetisation orientation is changed the tunnelling probability, and hence the conductance, can change dramatically.

The TAMR effect was further explored in a fully epitaxial (Ga,Mn)As/GaAs/(Ga,Mn)As stack by Rüster *et al.* (2005). In addition to the inverted spin-valve response and dependence on field and temperature, a further characteristic of the TAMR was demonstrated: low-bias amplification. By exploiting this a MR of over 150 000% was achieved at a temperature of 1.7 K.

In this Chapter lateral nanoconstriction devices fabricated from an ultra-thin (Ga,Mn)As epilayer via high resolution electron-beam lithography will be used to explore the MR effects that can exist in DMS nanostructures. This "double-pronged" approach takes advantage of the capabilities of e-beam lithography to create lateral nanostructures and also the ability of MBE to create vertical nanostructures. The geometry that will be considered is one where the domain

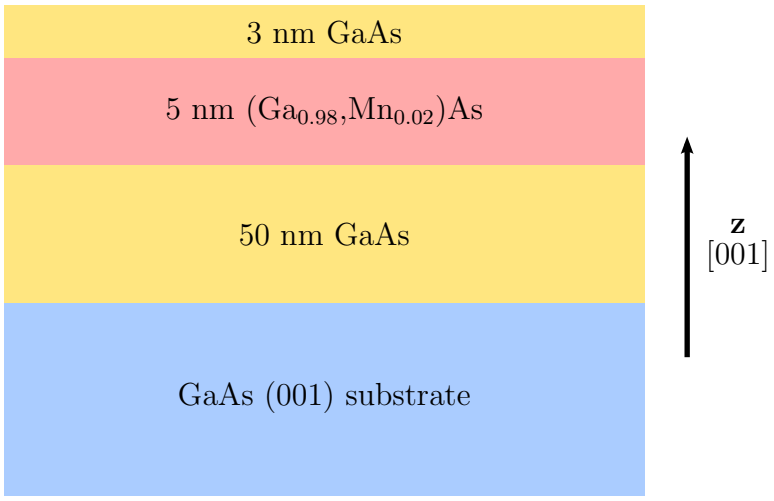

Figure 3.1: Schematic showing the epitaxial growth details of epilayer Mn-174.

wall and TMR effects are diminished. However, large and dramatic effects shall be demonstrated. These will be discussed within the context of the TMR and TAMR experiments.

A note about terminology: the term AMR is usually used to refer to an MR effect, known in metals for well over a century (Thomson, 1857), that occurs in the Ohmic transport regime. However, as shown by TAMR, there are anisotropic MR effects that occur with different physical origins. Therefore, in the interests of precision and clarity, the well known AMR effect will be referred to as normal AMR (NAMR), while AMR will refer to any MR that is anisotropic.

This work is summarised in Giddings *et al.* (2005).

3.2 Experimental details

All the devices in this Chapter were fabricated from a single $(Ga_{0.98},Mn_{0.02})As$ epilayer, sample number Mn-174, which was grown along the [001] crystal axis by low temperature MBE (Campion *et al.*, 2003). The level of manganese doping was estimated by flux gauge readings during growth. However, subsequent secondary ion mass spectroscopy (SIMS) and flame spectroscopy measurements suggest that the actual value was 10-20% higher. Although the (Ga,Mn)As epilayer was 5 nm thick, there was a 3 nm GaAs capping layer grown on top. Figure 3.1 shows a schematic of the sample composition.

The material was characterised using an as-grown piece of epilayer approximately 5 mm × 5 mm in size, processed into a van der Pauw geometry. From measuring

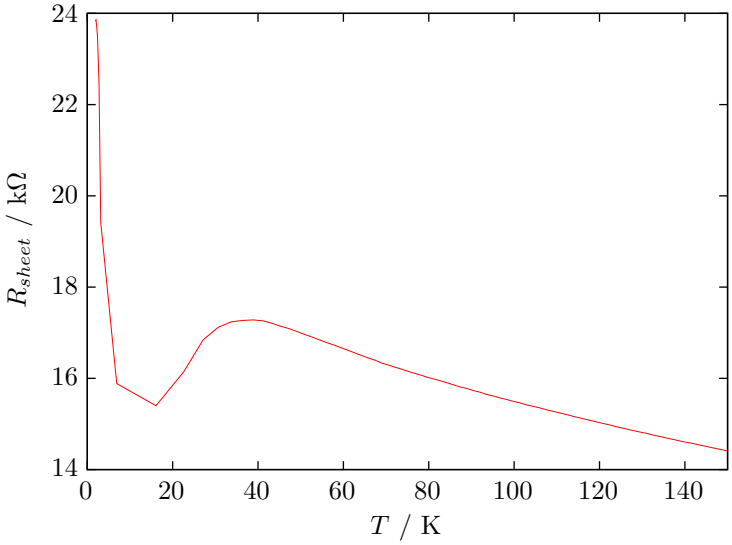

Figure 3.2: Sheet resistance, R_{sheet}, against temperature, T, as bulk as-grown (Ga,Mn)As sample Mn-174 is cooled down. Below 30 K the cooling process became very rapid, resulting in few measurement points.

the sheet resistance, R_{sheet}, as a function of temperature, T, shown in Figure 3.2, the Curie temperature, T_C, was estimated to be 40 K. Although $R_{xy}(H)$ measurements were taken, Arrott plot (M^2 against H/M) analysis did not give a more precise estimate. The room temperature conductivity was 150 $\Omega^{-1}\,\mathrm{cm}^{-1}$, which is comparable to thicker layers with 2% Mn doping. However, unlike thicker epilayers, the resistance tended to diverge at low temperatures, with conductivity reduced to about 100 $\Omega^{-1}\,\mathrm{cm}^{-1}$ at 4.2 K. For comparison, an epilayer with only a 1 nm GaAs capping layer, but otherwise identical, became highly insulating below 20 K. This highlights the technical challenges in producing consistently well behaved ultra-thin films. The low manganese doping and ultra-thin nature of the epilayer meant that there was a low quantity of magnetic moments which precluded characterisation by superconducting quantum interference device (SQUID) magnetometry.

The devices were fabricated using a five stage *e*-beam lithography process featuring complementary low and high resolution exposures. The inner alignment marks, Hall bar, and constrictions were patterned in PMMA positive resist and developed using a IPA:H_2O co-solvent developer. Etching was performed using a silicon tetrachloride ($SiCl_4$) RIE dry etch. The bond pads were patterned using UVIII positive resist. See Chapter 2 for further details about the fabrication process.

The geometry of the device is shown in optical microscopy image Figure 3.3(a).

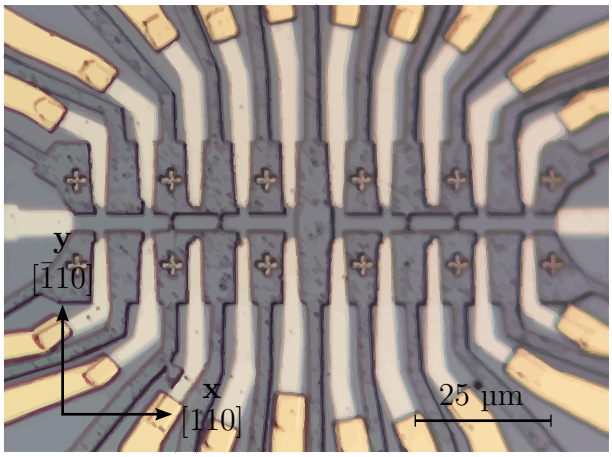

(a)

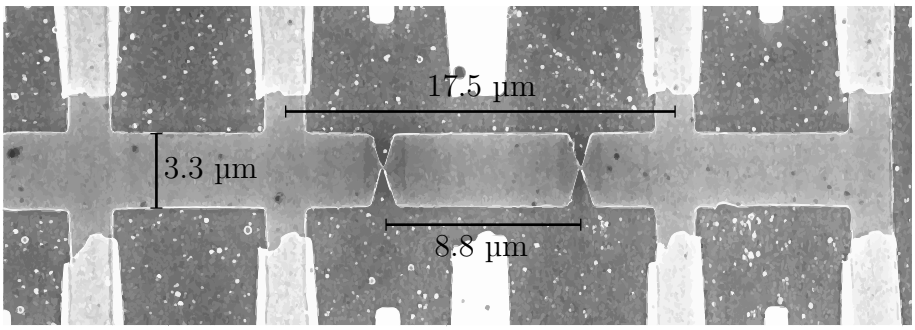

(b)

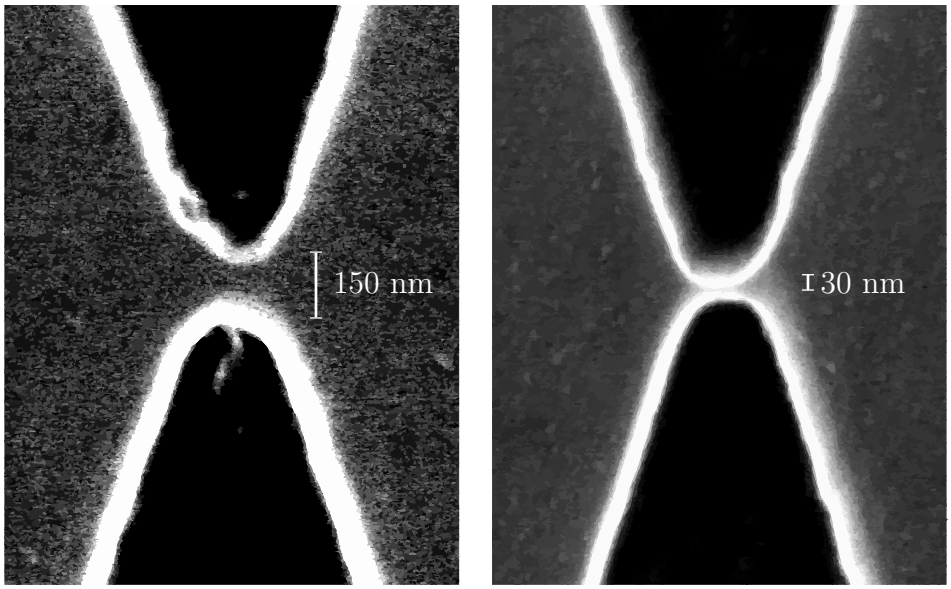

(c) (d)

Figure 3.3: (a) Optical microscope image of the inner area of a sample, showing the parallel to current, **x**, and in-plane perpendicular to current, **y**, axes and their corresponding crystalline direction. (b) SEM micrograph of the Hall bar showing the principle dimensions. (c) and (d) show high-resolution SEM micrographs of 150 nm and 30 nm constrictions, respectively.

Two devices were fabricated per field in order to improve fabrication efficiency and nanoconstriction yield. The Hall bar was self-aligned to the [110] cleaved axis, and had a width of about 3 µm as seen in Figure 3.3(b).

The Hall bars featured pairs of constrictions separated by 9 µm. These ranged in width from 400 nm down to sub-20 nm. Figures 3.3(c) and (d) show SEM micrographs of 150 nm and 30 nm constrictions, respectively. Although the high-resolution lithographic step was successful in producing a sub-20 nm constriction, unfortunately the device in which it featured was in other ways unsuccessfully fabricated. This meant the smallest measurable pair of constrictions on any device had an apparent width of 30 nm. Of the devices fabricated in parallel, one did not undergo the high-resolution lithographic step, preserving its Hall bar structure. This unconstricted sample was used to conduct reference NAMR measurements. During the fabrication process the samples were exposed to growth/annealing level temperatures.

Sample measurements were carried out in a Helium-4 cryostat with an integrated superconducting magnet capable of fields up to 14 T. Although the sample probe was capable of rotating the sample in and out-of-plane, the mechanism proved to be unreliable. As a consequence, a full thermal cycle was required in order to alter the orientation of the sample with respect to the field. Unless otherwise stated, all measurements were conducted at a temperature of 4.2 K.

The principle measurement method was with standard low-frequency (17 Hz) lock-in techniques, using EG&G 5210 lock-in amplifiers. The alternating current (AC) measurement techniques were used in order to maximise the signal-to-noise ratio. The applied 2-point signal, generated by an HP 3245A Universal Source, was 0.05 V with either an 8.2 MΩ or an 100 MΩ resistor in series to give a pseudo constant current. The four-point potential difference was measured across the devices. Where necessary, pre-amplifiers were used to improve the signal-to-noise. In addition, four point current-voltage (I-V) curves and resistances were measured for the unstructured Hall bar and the constrictions. These were measured using an Agilent 4155B Semiconductor Parameter Analyzer, which was also used for some DC transport measurements on the unstructured bar.

3.3 Results

The results shall be presented in two parts. The first will deal with the bulk magnetotransport properties of the ultra-thin (Ga,Mn)As epilayer used by all

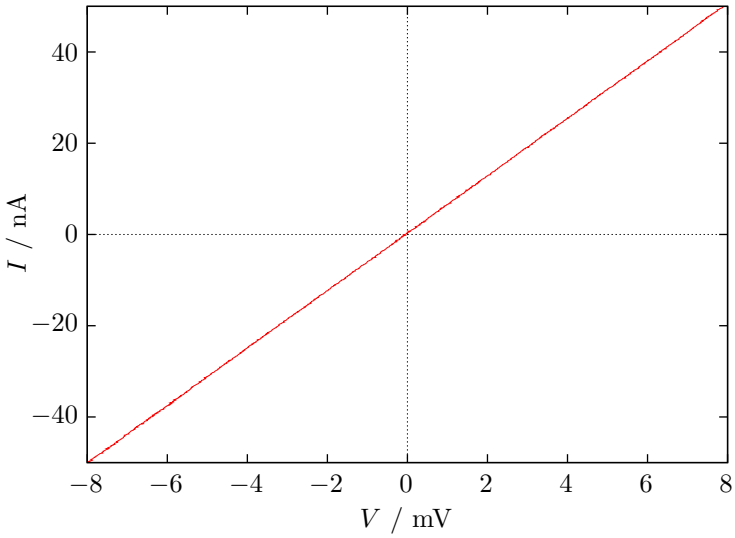

Figure 3.4: Four-point I-V curve for the unpatterned 3.3 µm Hall bar at T = 4.2 K.

devices in this Chapter. This is of particular interest as these were the first ever published measurements of a (Ga,Mn)As epilayer as thin as 5 nm. This will provide an important basis for considering the data presented in the second part. Due to the difficulty in reliably creating such thin films they are, to this day, still poorly characterised. However, the expected properties of (Ga,Mn)As are well understood from systematic measurements in thicker films (Esch *et al.*, 1997; Ohno, 1998; Sadowski *et al.*, 2000).

The second part of the results will consider devices featuring the nanoconstrictions. The effect of constrictions as their lateral dimensions are reduced will be studied. Particular attention will be paid to the startling MR effects seen in the smallest sized nanoconstrictions.

3.3.1 Unstructured bar

The unstructured Hall bar was fabricated in parallel with the nanoconstriction devices, on the same (Ga,Mn)As chip. The only difference was that the final high-resolution lithographic step to form the nanoconstrictions was not performed on that field. The stripe was aligned along the [110] axis and the dimensions are as shown in Figures 3.3(a) and (b).

The I-V characteristics for the unstructured bar when T = 4.2 K are shown in Figure 3.4. The sample exhibits Ohmic behaviour with a conductivity of 66 $\Omega^{-1}\,\mathrm{cm}^{-1}$.

The post-processing sheet resistivity is therefore higher than that of the as-grown material. Changes in conductance and Curie temperature are an expected result of heating, as interstitial manganese are out-diffused from the material (Edmonds *et al.*, 2004). However, in thicker films this annealing causes an increase in conductivity. No explanation is given for this anomaly, although it is noted that, given the fragility of the ultra-thin film, the fabrication steps may have had an adverse effect on the quality of the layer. It is possible that the exposure to the variety of solvents and conditions that processing entails could have inadvertently etched or induced additional inhomogeneity in the surface of the epilayer. To put it in perspective, the size of the unit cell of GaAs is 0.565 nm so even a small change to the top layer could be significant to the 5 nm film.

Figure 3.5 shows the NAMR characteristics of the unstructured bar at $T = 4.2$ K with the magnetic field applied along the three cardinal axes. As per Figure 3.3(b), the following notation shall be used to describe these axes: parallel to the direction of current is **x**, perpendicular to the current but still in-plane is **y** and perpendicular to the current and out-of-plane is **z**. When the field was applied along the **x**-axis there were positively orientated hysteretic features, while for $\mathbf{H} \parallel \mathbf{y}$ and $\mathbf{H} \parallel \mathbf{z}$ the hysteretic features were negative. Additionally, for $\mathbf{H} \parallel \mathbf{z}$ the hysteretic feature was comparatively very broad, starting around $\mu_0 H = \pm 0.2$ T. This hysteretic low field switching is associated with magnetisation reversal, and since the magnitude and sense change with orientation, it is therefore a manifestation of the NAMR. The isotropic (independent of applied field orientation) negative background part of the MR is attributed to the suppression of the magnetic disorder at high fields (Baxter *et al.*, 2002) or to weak localisation effects (Matsukura *et al.*, 2004).

Previous SQUID magnetometry measurements in thicker (Ga,Mn)As epilayers shows that there exists competition between the [100]/[010] biaxial and [110] uniaxial easy axes (Sawicki *et al.*, 2005). Typically, below the Curie temperature the epilayers are initially uniaxial but as temperature is reduced the epilayers undergo a transition and the biaxial behaviour comes to dominate. However, SQUID magnetometry of these ultra-thin films were not feasible due to their low quantity of moments. If it is assumed that at 4.2 K, as in the thicker films, the cubic anisotropy dominates in the ultra-thin epilayer, in the unstructured bar which is orientated along the [110] direction magnetisation, reversal can proceed via the stable intermediate [100] and [010] orientations (Tang *et al.*, 2003). Therefore, the positive hysteretic feature in Figure 3.5 for $\mathbf{H} \parallel \mathbf{x}$ is interpreted as a rotation from [110] into an orientation close to the [100] easy axis. Similarly, the negative

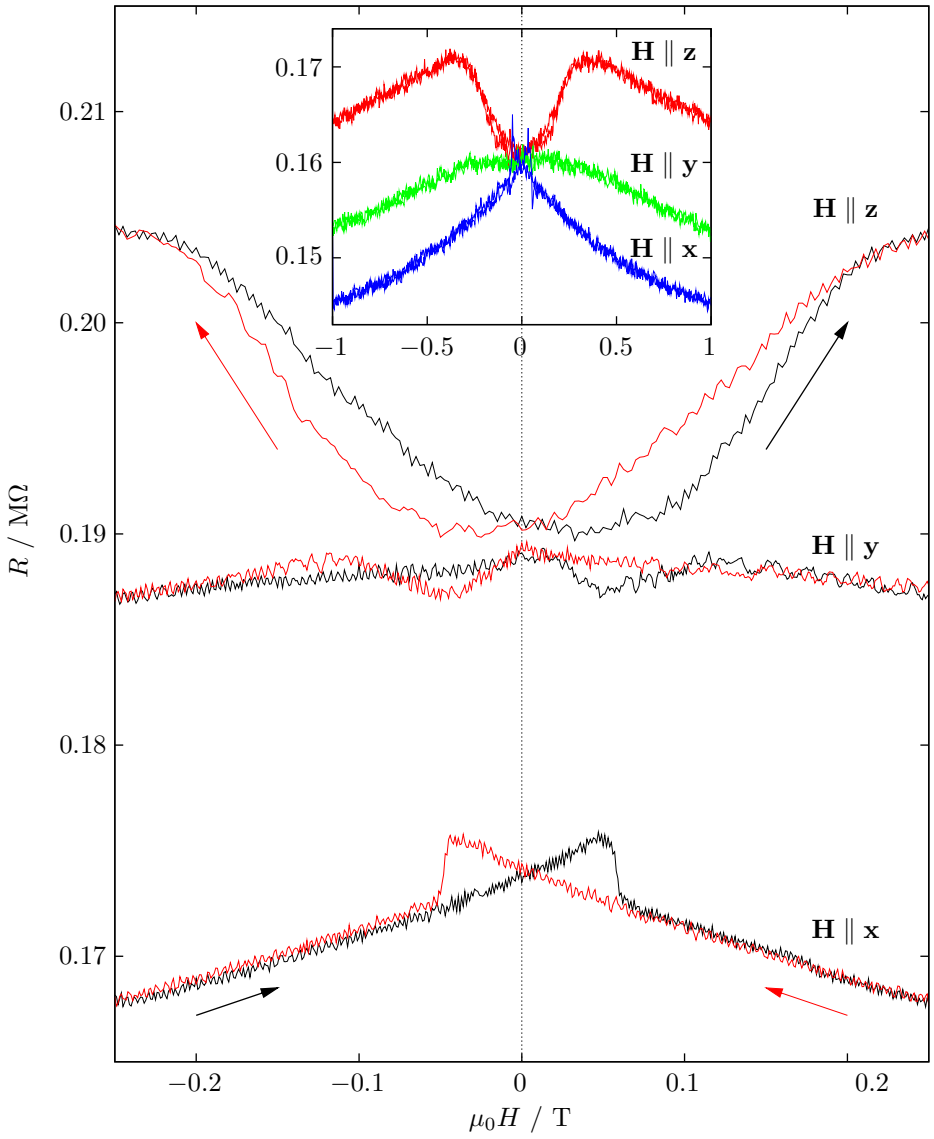

Figure 3.5: Low-field AC MR measurements for the unstructured 3.3 µm bar patterned from the 5 nm thick epilayer, with field applied along the three cardinal directions. $\mathbf{x} \parallel [110]$ and $T = 4.2$ K. The black curves represent increasing field and the red curves represent decreasing field. The inset shows DC MR measurements for a greater field range. As discussed in the text, the AC measurements have a good signal-to-noise ratio but are affected by spurious resistance offsets. The offsets are absent in the DC measurements but the signal-to-noise ratio is poorer, obscuring the low-field hysteretic behaviour.

hysteretic feature for $\mathbf{H} \parallel \mathbf{y}$ would be a rotation from $[\bar{1}10]$ to the [010] easy axis. This is consistent with $\mathbf{M} \parallel \mathbf{x}$ being a low resistance state and $\mathbf{M} \parallel \mathbf{y}$ being a high resistance state (Baxter *et al.*, 2002; Jungwirth *et al.*, 2003; Rushforth *et al.*, 2007b).

Despite $\mathbf{M} \parallel \mathbf{y}$ being a high resistance state, a much larger MR was observed for $\mathbf{H} \parallel \mathbf{z}$ than for $\mathbf{H} \parallel \mathbf{y}$. Assuming that, at $\mu_0 H = 1$ T, the magnetisation was saturated along the direction of applied field, then, from the data in the inset of Figure 3.5, the in-plane NAMR, defined as $\mathrm{AMR}_{ip} = (R(\mathbf{M} \parallel \mathbf{y}) - R(\mathbf{M} \parallel \mathbf{x}))/R(\mathbf{M} \parallel \mathbf{x})$, is found to be 5%. The out-of-plane NAMR, $\mathrm{AMR}_{op} = (R(\mathbf{M} \parallel \mathbf{z}) - R(\mathbf{M} \parallel \mathbf{x}))/R(\mathbf{M} \parallel \mathbf{x})$, is 12%. In previously studied $(Ga_{0.98},Mn_{0.02})$As epilayers there was virtually no difference between the MR for the two perpendicular-to-current orientations (Jungwirth *et al.*, 2003).

The large observed out-of-plane MR is therefore attributed to the strong vertical confinement in the ultra-thin 5 nm $(Ga_{0.98},Mn_{0.02})$As epilayer, breaking the symmetry between states with magnetisation $\mathbf{M} \parallel \mathbf{y}$ and $\mathbf{M} \parallel \mathbf{z}$. Another indication of confinement effects is the presence of hysteresis in the $\mathbf{H} \parallel \mathbf{z}$ MR. In thicker (Ga,Mn)As epilayers the growth direction is magnetically hard with zero remanence due to compressive strain induced by the GaAs substrate and shape anisotropy (König *et al.*, 2003). The strain can have significant influence on the characteristics of the NAMR, and particularly it has been previously observed that there is a dependence of the AMR_{ip} and AMR_{op} to the current direction as a function of the level of strain (Matsukura *et al.*, 2004). In experiments with laterally defined wires, shape anisotropy has been found to have a significant effect on the magnetic configuration of (Ga,Mn)As when the lateral widths of the wires is as large as 0.8 µm (Hamaya *et al.*, 2004). However, the effect of local strain relaxation (Wenisch *et al.*, 2007) was not taken into account in that interpretation and may have in fact been the dominant contribution. In these 5 nm layers the shape anisotropy can still be expected to play some role, though. These effects compete in the epilayer with an increase in the relative population of the heavy-hole states due to confinement, which tends to favour spin polarisation along the growth direction (Lee *et al.*, 2002).

An important remark concerning the low-field AC measurements shown in the main panel of Figure 3.5 is that they were affected by spurious resistance offsets. This lead to the apparent splitting of the MR at low fields, which was particularly evident in the case for $\mathbf{H} \parallel \mathbf{x}$. The advantage of these measurements was their good signal-to-noise ratio, allowing clear presentation of the hysteretic features.

To overcome the issue of the spurious offsets, DC measurements are shown in the inset of Figure 3.5. The offsets were absent in the DC measurements, allowing an estimation of the NAMR, but the signal-to-noise ratio was significantly poorer, which tends to obscure the hysteretic behaviour. The offsets are field-independent and are a result of the AC lock-in technique combined with the thermal cycling of the sample. As previously mentioned, *in situ* rotation of the sample was not viable with the experimental apparatus, so a full thermal cycle had to be performed in order to change the field orientation. However, the shape of the individual MR curves was fully reproducible.

3.3.2 Nanoconstrictions

Having examined the properties of the bulk (Ga,Mn)As 5 nm epilayer the devices containing the constrictions will be considered.

Figures 3.6 shows the MR characteristics with $\mathbf{H} \parallel \mathbf{x}$ for (a) the unstructured bar and constrictions of (b) 100 nm, (c) 50 nm and (d) 30 nm widths, at $T = 4.2$ K. The 100 nm constrictions showed behaviour typical of (Ga,Mn)As epilayers (Baxter *et al.*, 2002) and were otherwise very similar to the unstructured bar. The resistance across the device with the 100 nm constrictions was approximately double that of the unstructured bar. Given that the geometry of the unstructured bar was of 5.3 "squares" then the increase in the current path would correspond with the two constrictions increasing the number of squares of material by about 6.6. This seems consistent with the known geometry of the constrictions, as shown by SEM micrographs in Figures 3.3.

The MR of the 50 nm constrictions (Figure 3.6(c)) deviates partly from the normal bulk (Ga,Mn)As seen in the unstructured bar. The low-field hysteretic features are as expected, but the isotropic background now contains an inflection point near $\mu_0 H = 0.3$ T after which the gradient of the non-hysteretic background MR increases. The resistance of the device was approximately triple that of the unstructured bar. Using the previous analysis, this would correspond to the two 50 nm constrictions increasing the apparent length of the devices by 10 squares.

In Figure 3.6(d) the 30 nm constrictions show a dramatic deviation from the previously observed MR behaviour. The low-field hysteretic features have now changed in sign to become negative going, and are much greater in size. Additionally, the resistance of the device was an order of magnitude greater than that of the unstructured bar. This is too great to be accounted for through the

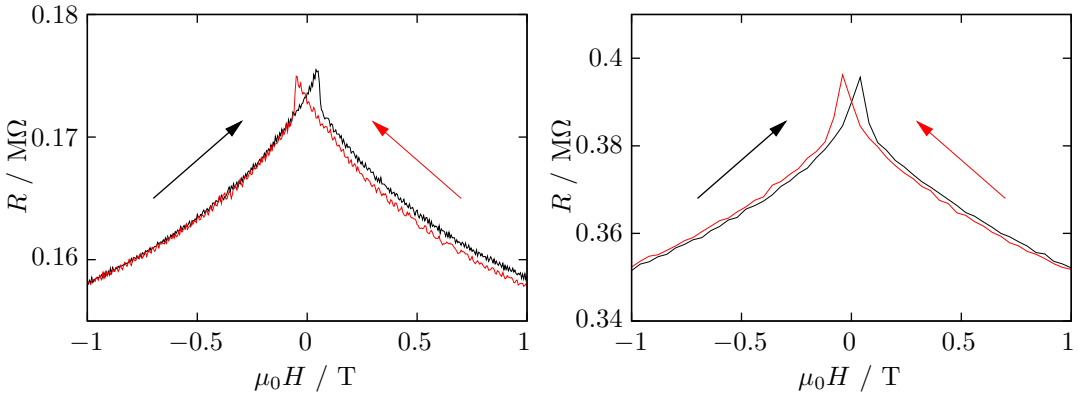

(a) unstructured bar

(b) 100 nm

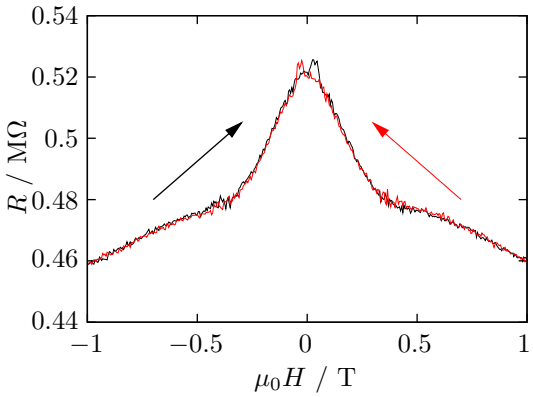

(c) 50 nm

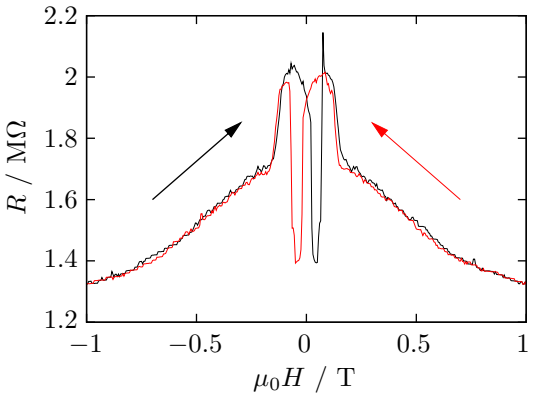

(d) 30 nm

Figure 3.6: AC MR measurements at $T = 4.2$ K for (a) the unstructured 3.3 µm bar, (b) 100 nm constrictions, (c) 50 nm constrictions and (d) 30 nm constrictions, each patterned from 5 nm epilayer. The alignment of the field is $\mathbf{H} \parallel \mathbf{x} \parallel [110]$ in each case. The black curve represents increasing field and the red curve represents decreasing field.

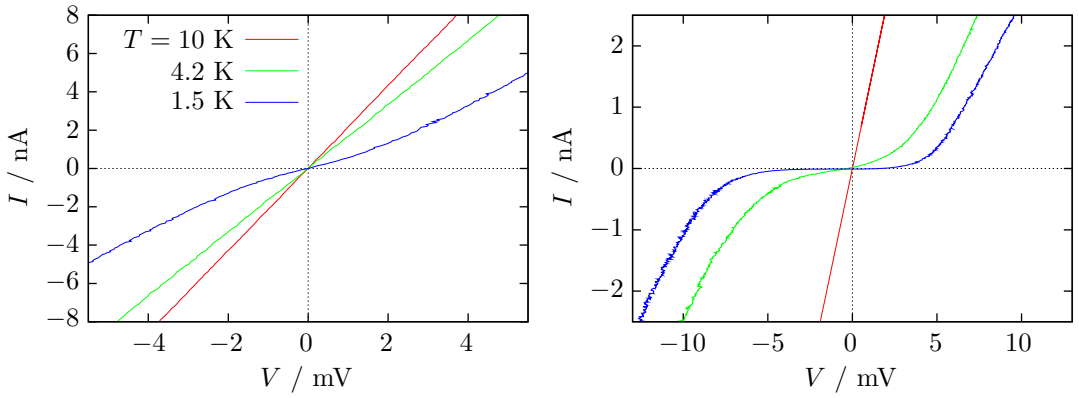

(a) 50 nm (b) 30 nm

Figure 3.7: I-V characteristics for (a) the 50 nm constrictions and (b) the 30 nm constrictions at temperatures, T, of 10 K, 4.2 K and 1.5 K. $B = 0$ T.

constrictions simply increasing the current path.

The measured temperature dependent I-V curves are shown in Figures 3.7 for the (a) 50 nm and (b) 30 nm constrictions. While the devices with constrictions of a size greater than 100 nm show Ohmic behaviour, deviations from this become more pronounced as the constriction size and temperature were reduced. The 50 nm constriction was very slightly non-linear at $T = 4.2$ K and considerably more so at $T = 1.5$ K. At low temperature and bias, conduction through the 30 nm constrictions was by tunnelling. This strongly suggests that the anomalies observed in the AMR in Figures 3.6(c) and (d) are the result of the onset and formation of tunnel junctions across the constrictions. The occurrence of tunnelling in such a wide constriction suggests that disorder in the very thin, low manganese density, (Ga,Mn)As material leads to a local depletion and so the tunnel barrier has an effective lateral width considerably smaller than the nominal physical width.

In Figure 3.8 the measured AMR characteristics of the 30 nm constrictions are shown for magnetic fields applied in the three orthogonal directions. The main panel focuses on the low field switching behaviour while the inset shows the same measurements over a larger field range. As with the NAMR measurements of the unstructured bar (see Figure 3.5), these AC measurements are affected by spurious field-independent resistance offsets. As a result, it is not possible to determine accurately the size of the AMR effect in this non-linear regime, and unfortunately, the device was rendered inoperable before DC measurements could be taken. However, an order of magnitude increase of the anisotropic MR in the

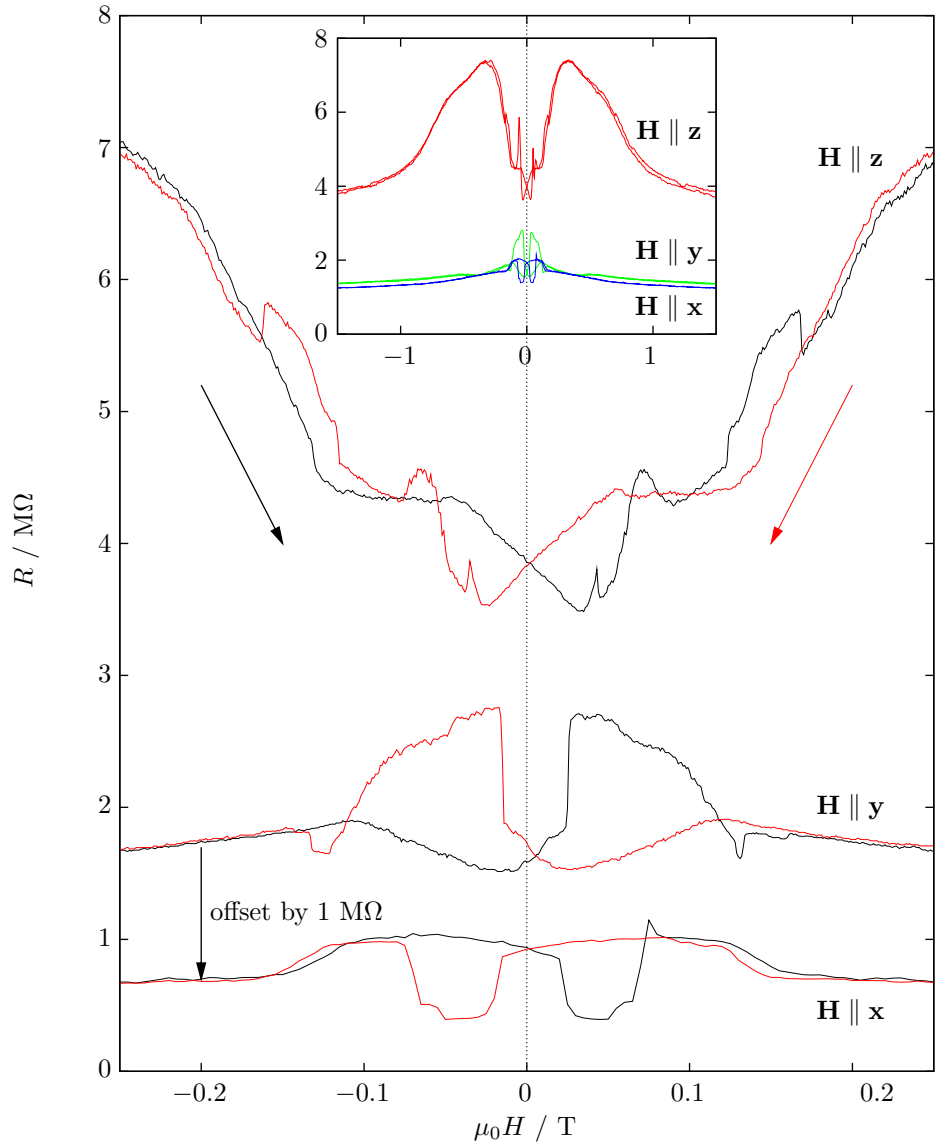

Figure 3.8: Low field AC MR measurement of the 30 nm constrictions fabricated from a 5 nm thick epilayer, with the field applied along the three cardinal directions. $\mathbf{x} \parallel [110]$ and $T = 4.2$ K. The black curves represent increasing field and the red curves represent decreasing field. The $\mathbf{H} \parallel \mathbf{x}$ curve is offset 1 MΩ downwards for clarity. The inset shows the same measurements over a wider field range.

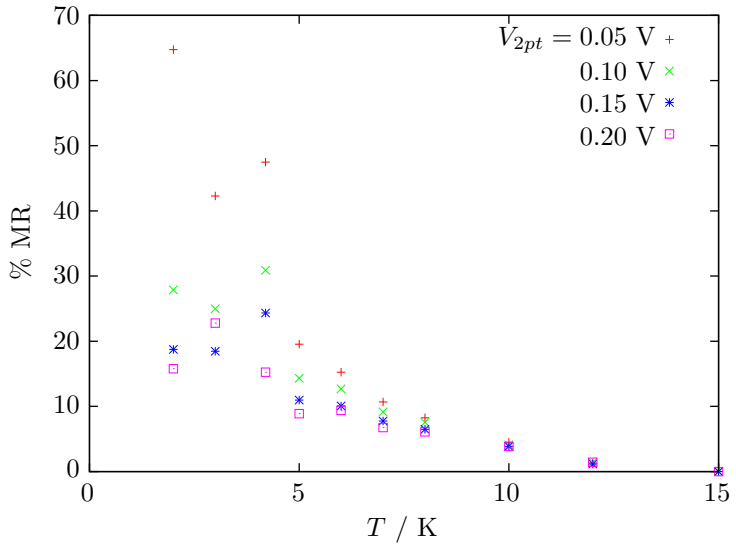

Figure 3.9: Temperature, T, dependence of the hysteretic low-field MR of the 30 nm constriction for four different applied 2-point voltages, V_{2pt}, with magnetic field orientated $\mathbf{H} \parallel \mathbf{x}$.

tunnelling regime is clearly visible from the $\mathbf{H} \parallel \mathbf{z}$ and $\mathbf{H} \parallel \mathbf{y}$ traces shown in the inset of Figure 3.8.

It is important to note that the results of the measurements shown in Figure 3.8 were made using a fixed 2-point excitation which, in this device, would result in a current in the range of 1 to 1.5 nA. Although this method was suitable for measuring the nanoconstrictions operating in the Ohmic regime, because of the large MR effects inherent in the tunnelling device, particularly in the $\mathbf{H} \parallel \mathbf{z}$ orientation, the current could deviate somewhat. As a result of the non-Ohmic I-V characteristics of the tunnel junction, this may have lead to a relative suppression of the magnitude of the measured MR.

The other important point concerns the reproducibility of the data. Within a thermal cycle all MR traces in the tunnelling device had very good reproducibility. However, thermal cycling could have significantly altered the details of the MR, although the same general trends remained, giving at least reasonable qualitative agreement. In Chapter 4 the effects of the thermal cycling will be discussed in more detail.

In Figure 3.9 the % MR of the low-field hysteretic feature is plotted as a function of temperature for four different applied 2-point voltages, V_{2pt}: 0.05 V, 0.10 V, 0.15 V and 0.20 V. These correspond to an excitation for $\mu_0 H = 0$ T at $T = 4.2$ K of 2.3 mV, 4.4 mV, 6.3 mV and 8.0 mV respectively. % MR is defined as $(R_{max}(H) - R_{min}(H))/R_{min}(H)$, for low values of H, i.e. $\mu_0 H < \pm 0.1$ T, so that

only the hysteretic part of the curve is considered. The magnitude of low field hysteretic MR increases strongly as temperature and excitation voltage decrease. Again, because of the measurement scheme, the size of the % MR is suppressed in comparison to a constant potential measurement scheme. Despite this, the data show that there is a strong dependence of the size of the MR effect on both the temperature and excitation voltage across the device.

3.4 Discussion

The close correspondence between the NAMR of the unstructured bar in Figure 3.5 and the AMR of the 30 nm constrictions in Figure 3.8 is evident. Firstly, the switching events in the in-plane MR traces occur at comparable magnetic fields in the case of both devices. Secondly, in both devices the hysteretic effects of the in-plane $\mathbf{H} \parallel \mathbf{x}$ and $\mathbf{H} \parallel \mathbf{y}$ have similar magnitudes but are of opposite sign. Thirdly, the MR for when $\mathbf{H} \parallel \mathbf{z}$ in both experiments is considerably larger than for the in-plane field orientations, and both MR traces are similar in general form and field scale.

However, there are also several key differences between the character of the NAMR in the unstructured bar and that of the AMR in the non-linear regime of the 30 nm constriction. Firstly, with the onset of tunnelling transport there is a radical departure from the basic NAMR low-field hysteretic features. Particularly, the orientation of the hysteretic features for the in-plane orientations is now reversed; for $\mathbf{H} \parallel \mathbf{x}$ the orientation switched from positive to negative, while for $\mathbf{H} \parallel \mathbf{y}$ the orientation switched from negative to positive. This indicates that the high and low resistance in-plane magnetisation states have switched places. Secondly, the size of the hysteretic features increased dramatically when transport entered the tunnelling regime. Thirdly, it is important to emphasise that even at large fields, where the magnetisation should be saturated, the resistances in the three orientations are still very different. This is a strong indication that the transport mechanisms in the Ohmic and non-linear regimes have different anisotropies.

Despite having a double constriction system, similar to the device of Rüster *et al.* (2003), the negative low-field hysteretic effect in this tunnelling device is not compatible with a TMR system. In a TMR device, if there is a parallel alignment of the magnetisation on either side of the constriction then the device would be in a low resistance state, while an antiparallel alignment would lead to a high

resistance state. Although in some metal tunnel junctions a negative TMR can be observed if the minority spin carriers carry more current than the majority spin carriers (De Teresa *et al.*, 1999; Sharma *et al.*, 1999), this will not occur in a fully (Ga,Mn)As system since the spin polarisation on both sides of the tunnel barrier will be positive. Therefore, magnetisation reversal could only lead to a positive hysteretic effect as alignment flips from a parallel alignment to an antiparallel alignment and then back as the field is swept.

Furthermore, the TMR signal reported in Rüster *et al.* (2003) is a property of the special geometry of that device. In that experiment the bar was orientated along the [100] easy axis, and the TMR corresponded to the subsequent 180° magnetisation reversal in the leads and central island. Because of the geometry of the narrow central island the contributions to the anisotropy from the shape and local strain relaxation caused it to have a significantly larger coercive field than the wider (Ga,Mn)As leads on either side of the constrictions. As a result, the magnetisation switching of the island and leads was not simultaneous. In the device studied in this Chapter the central region does not have a long thin geometry, but is rather shaped similarly to the leads; there is no reason to expect anything other than near-simultaneous switching events.

Additionally, the (Ga,Mn)As in Rüster *et al.* (2003) was much thicker (19 nm) than in this experiment, so the additional complexities in the anisotropy landscape introduced by the confinement effects, as previously discussed, are excluded. Therefore, the AMR behaviour that dominates in this Chapter's tunnelling nanoconstriction devices is distinct from the TMR effect. Hence, these data are interpreted as being TAMR, which can give both normal and inverted spin-valve-like behaviour depending on the applied field orientations (Gould *et al.*, 2004; Rüster *et al.*, 2005).

The strong link between the NAMR of the epilayer and the TAMR of the nanoconstrictions is demonstrated by the $\mathbf{H} \parallel \mathbf{z}$ MR. The field dependence in both transport regimes is analogous; the considerably larger out-of-plane anisotropies of the epilayer results in the extremely large out-of-plane TAMR. This is similar to the effect seen in Gould *et al.* (2004) where the strain in the growth direction is attributed to the stronger MR when the magnetisation is out-of-plane.

Hysteretic MR responses in the unstructured bar for purely in-plane magnetisation are relatively easy to explain and can give useful information on magnetisation reversal processes (Tang *et al.*, 2003). MR traces in the nanoconstriction can have a more complex dependence on the orientation of the magnetisation

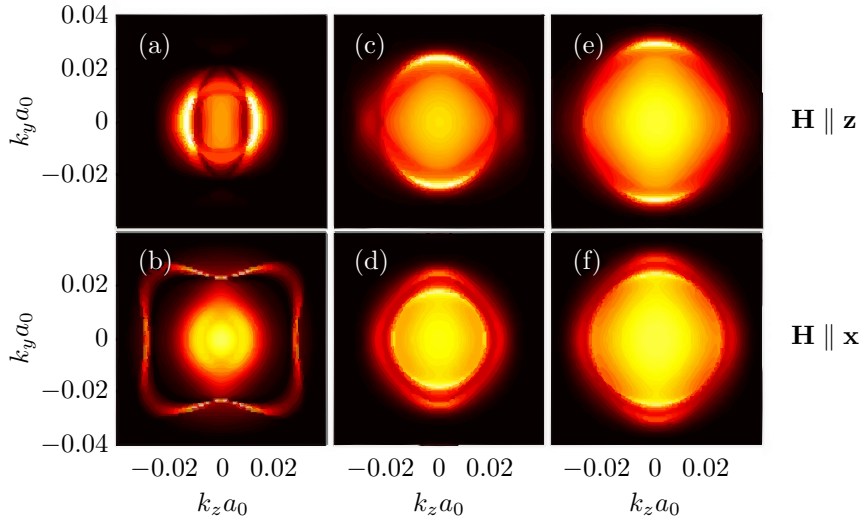

Figure 3.10: Plot of the calculated tunnelling transmission probabilities against the conserved in-plane momenta at the Fermi energy. The carrier densities are (a) and (b) 0.01 nm^{-3}; (c) and (d) 0.05 nm^{-3}; and (e) and (f) 0.1 nm^{-3}. The barrier height is 1 eV and the width is 2 nm. Bright yellow is the highest probability for a given density, red is medium and black is zero. The tunnelling current is along the **x** direction and the magnetisation is along **z** direction for the first row and along the **x** direction for the second row.

with respect to the crystallographic axes and current direction (Rüster *et al.*, 2005) depending on the tunnelling DOS. Detailed interpretation of the low-field hysteretic MR response of the nanoconstrictions is not possible without detailed information on the magnetisation reversal sequence near the constriction. Furthermore, the dependence of the size of the MR on temperature is consistent with the increasing dominance of tunnelling, and the low-bias amplification effect reported in vertical TAMR devices (Rüster *et al.*, 2005) is also observed. This seems to indicate the dominance of the TAMR effect in the tunnelling regime of this device.

In Figure 3.10 the results are shown of calculations by Jairo Sinova and Tomas Jungwirth which attempt to model the TAMR effect in the experimental structure. In the Figure the Landauer transmission probabilities at the Fermi energy is plotted as a function of conserved momenta in the (k_z,k_y) plane, illustrating the effects of confinement on the TAMR. Further details of the modelling can be found in Giddings *et al.* (2005).

The plots show the intricate dependence of the theoretical TAMR on the position in the (k_z,k_y) plane and so is highly sensitive to the magnetisation. When

integrated over all the states at the Fermi energy the TAMR ranges between $\sim 50\%$ and $\sim 1\%$ for the studied hole densities of 0.1 - 1 $\times 10^{20}$ cm^{-3} (Giddings *et al.*, 2005). However, these calculations depend on the assumption that the strong vertical confinement will reduce the number of k_z states, while the constriction will reduce the number of k_y states. At such low assumed hole densities the (Ga,Mn)As would be near the metal-insulator transition and that suggests a highly disordered system. As a result of the spreading of k states the size of the MR would be severely diminished. Furthermore, the mean free-path of carriers is much smaller than the size of the nanoconstrictions, making it doubtful that its geometry could play a significant role in restricting the momentum states. The possibility thus remains that additional physics is at work which could more satisfactorily explain the large MR. This is discussed further in the next chapter.

3.5 Conclusion

The existence of large anisotropic MR effects has been demonstrated in laterally defined (Ga,Mn)As nanoconstriction tunnel junctions. The relationship between the basic NAMR of the material and the anisotropic MR of the tunnel junction has been shown. The effect has been shown clearly not to be a manifestation of TMR, but is consistent with the TAMR effect. This seems to establish TAMR as a generic property of tunnel devices in ferromagnetic materials with strong SOC. Importantly, AMR is present in many metallic ferromagnets (Jaoul *et al.*, 1977) so this may have consequences outside ferromagnetic semiconductors.

Chapter 4

Nanoconstrictions Revisited

4.1 Introduction

In conductors there can exist many forms of MR, whereby the electrical resistance is modified via the application of a magnetic field. When the size of a MR is a function of the angle between the magnetisation and direction of flow of carriers or crystallographic axes it is known as either the non-crystalline or crystalline AMR, respectively (McGuire and Potter, 1975; Rushforth *et al.*, 2007b). The origin of this effect is the SOC. As before, this well known AMR in the Ohmic regime shall be referred to as the NAMR.

When a non-Ohmic tunnelling regime is considered instead, a much more dramatic effect known as TAMR can occur, as explored in Chapter 3. This is caused by the dependence of the tunnelling density of states on the direction of the magnetisation of the material; thus the tunnelling probabilities can be directly manipulated with the application of a magnetic field, resulting in large MR effects. This was demonstrated initially in vertical structures based on the DMS (Ga,Mn)As (Gould *et al.*, 2004; Rüster *et al.*, 2005). Shortly after, data consistent with TAMR in lateral nanoconstriction devices were reported (Giddings *et al.*, 2005). As a consequence of this, it was predicted that TAMR could be a generic property of tunnel devices with ferromagnetic contacts (Shick *et al.*, 2006). This prediction has proved to be correct; since then, the TAMR phenomenon has also been reported in transition metal tunnel junction systems (Bolotin *et al.*, 2006; Gao *et al.*, 2007; Shi *et al.*, 2007; Park *et al.*, 2008).

In further work on (Ga,Mn)As lateral tunnelling devices another novel magnetoresistance effect was reported, the so-called CBAMR (Wunderlich *et al.*, 2006).

The origin of CBAMR is anisotropic shifts in the Fermi energy with respect to magnetisation in an inhomogeneous system. This can be achieved by patterning a nanoscale single electron transistor (SET) type structure from a ferromagnetic material with strong SOC. This observation occurred in an accidentally inhomogeneous constriction with an associated gate that allowed tuning of the local electrostatic conditions; as a result of the patterning the necessary inhomogeneity was created in the form of extremely low capacitance "islands" isolated from the rest of the structure by a tunnel barrier. In systems with strong SOC, such as (Ga,Mn)As, magnetisation rotation can cause large changes in the electronic configuration. As a result of the non-uniform local carrier concentration in these structures, changes in the magnetisation orientation causes differential changes in the chemical potential of the nanoscale island and leads. The Gibbs free energy associated with transmission of charge through the island can be written as a function of these different chemical potentials and as such is dependent on the magnetisation. Furthermore, the difference in the chemical potential between the island and the leads is of a similar order to the single-electron charging energy (Wunderlich *et al.*, 2006), resulting in potentially dramatic changes in conductivity.

A possible third mechanism for large magnetoresistance effects in DMS tunnel devices has since also been suggested, in the form of a magnetisation orientation induced metal-insulator transition (Pappert *et al.*, 2006). This can occur when a high localisation of carriers, such as at low temperatures or in highly depleted regions, causes transport to go from a diffusive to an Efros-Shklovskii hopping regime. If the structure is therefore close to a metal-insulator transition, and is highly anisotropic due to the strong SOC, then changing the magnetisation orientation could trigger the transition.

Putting this in the context of the previous two magnetoresistance effects, it is interesting to note that the ultra-thin (Ga,Mn)As films similar to those used by Giddings *et al.* (2005); Wunderlich *et al.* (2006) and in Chapter 3 become very resistive and exhibit hopping-like conductivity at very low temperatures ($T <$ 4 K). Additionally, they have unusually strong magnetocrystalline anisotropies (Rushforth *et al.*, 2007a), making this effect of interest in regard to these kinds of lateral structures.

Bearing in mind the diverse mechanisms for magnetoresistances that non-Ohmic devices in ferromagnets with strong SOC can acquire, in this Chapter further evidence of extremely large effects in laterally defined (Ga,Mn)As nanoconstric-

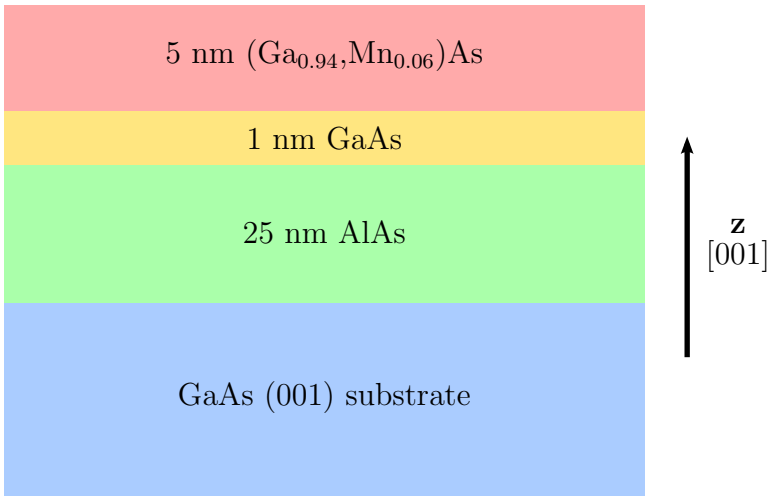

Figure 4.1: Schematic showing the epitaxial growth details of epilayer Mn-213.

tion devices will be demonstrated and so cast further light on these issues. The experimental devices contains many improvements over the results in Chapter 3. Firstly, the devices tested contain only a single nanoconstriction, making the device geometry easier to consider. The second improvement is that the measurement apparatus allowed for the rotation of the applied magnetic field. This is important for the understanding of anisotropic effects. Finally, thanks to the previous experience, the measurement setup was better suited for the examination of these lateral tunnelling devices. As a consequence, this allows for a reappraisal of the previous nanoconstriction work in the light of more recent theories.

The results of this Chapter are summarised in Giddings *et al.* (2008b)).

4.2 Experimental details

The devices were fabricated from a 5 nm thick $(Ga_{0.94},Mn_{0.06})As$ epilayer grown on a (100) GaAs substrate by low temperature (210-230°C) MBE, sample number Mn-213. The manganese doping was originally estimated at 5% through flux gauge readings made during growth. As a result of subsequent SIMS and flame spectroscopy measurements made on samples grown with the same apparatus this figure has been revised to 6%. As shown in the schematic of the epitaxial details, Figure 4.1, the (Ga,Mn)As layer was grown on a 25 nm AlAs layer, separated by a 1 nm GaAs buffer layer. The purpose of this AlAs layer was to increase the vertical confinement of the carriers in the magnetic layers. This was done primarily to aid the development of gated structures. The magnetic layer was grown with a

pre-deposition of gallium for 6 s, equivalent to 2 monolayers, followed by 20 s of manganese, equivalent to 0.4 monolayers. The intention of the pre-deposition was to improve the vertical consistency of the manganese concentration.

The as-grown sheet conductivity was 110 $\Omega^{-1}\,\mathrm{cm}^{-1}$ at room temperature, although at low temperatures ($T \sim 4$ K) the sample became insulating. After annealing at 170°C for 8 hours the material's room temperature conductivity was 200 $\Omega^{-1}\,\mathrm{cm}^{-1}$, and at 4.2 K was 60 $\Omega^{-1}\,\mathrm{cm}^{-1}$, with a Curie temperature of 120 K. The change in conductivity was the result of the removal of interstitial manganese (Edmonds *et al.*, 2004).

Sample fabrication was carried out on as-grown material via high-resolution electron beam lithography using a PMMA positive resist (see Chapter 2). This was developed using an IPA:H_2O solution and etching was achieved with a silicon tetrachloride ($SiCl_4$) RIE dry etch. During the fabrication process the sample was exposed to annealing level temperatures.

The devices consist of a Hall bar type structure with a single nanoconstriction, as shown in Figure 4.2(a). The bar was aligned along one of the cubic easy axes, which shall be denoted as the **x** axis. Differentiation between the [100] and [010] axis was not preserved during processing, so it shall be assumed that the bar is aligned along the [100] axis. The perpendicular in-plane axis is **y** and the perpendicular out-of-plane axis is **z** (see Figure 4.2(c)). Note that, while this is the same axis notation as used in Chapter 3, the crystalline orientation that the in-plane axes correspond to has now changed; the current, and hence **x** axis is now parallel to [100]. Scanning electron microscope measurements of the nanoconstriction, shown in Figure 4.2(b), estimate it to have a physical width of about 30 nm. However, carrier depletion and interface effects would make the effective width of the channel smaller. Non-linear current-voltage (I-V) characteristics developed below ~ 4 K are consistent with the development of tunnel barriers or hopping conduction (see Figure 4.5 in section 4.3).

Sample measurement was carried out in a Helium-4 cryostat down to 1.5 K, achieved by pumping on the Helium. An external magnetic field of up to 0.7 T could be rotated 180° in the **x**-**y** plane around the sample. Additionally, the sample could be rotated *in situ* via a manual rotation system on the sample rod, moving the **z** axis through 180° with respect to the field. This provided the possibility for any 3D angle of the applied magnetic field to the sample. Using a 4-point sensing measurement scheme, the potential across the constriction was kept constant and the current was measured across a resistor in series with the

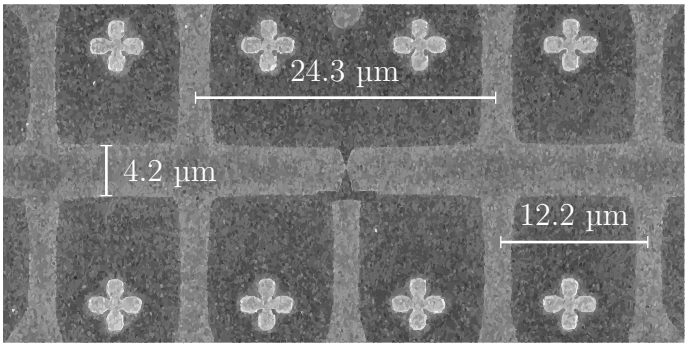

(a)

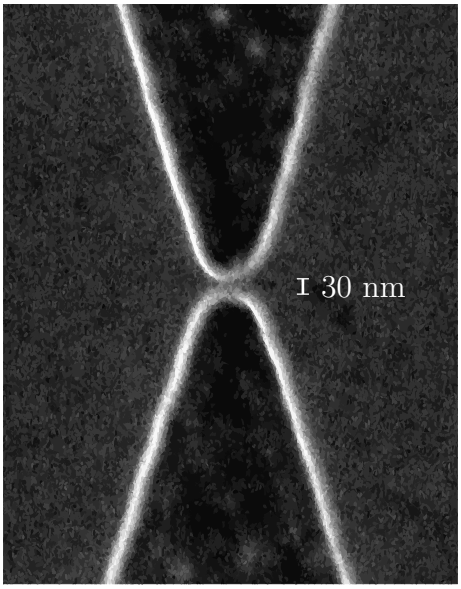

(b)

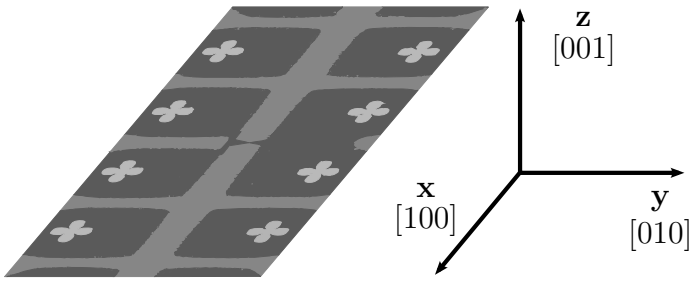

(c)

Figure 4.2: SEM micrographs of the device, showing (a) the Hall bar geometry of the device and the positioning of the nanoconstriction within it, and (b) a high-resolution image of the nanoconstriction showing it to have a width of about 30 nm. The orientation of the Hall bar with respect to the crystalline axes is shown in cartoon (c).

device. The voltage was generated by a Keithley 2400 sourcemeter, and HP 3457A and HP 3458A multimeters measured the potential difference across the constriction and serial 1 MΩ resistor, respectively.

4.3 Results

The MR measurements at $T = 4.2$ K for an unstructured bar and a nanoconstriction of about 40 nm are shown in Figure 4.3(a) and (b). The I-V characteristics in Figure 4.3(c) show the transport in these devices to be Ohmic, although some non-linearity is exhibited by the nanoconstriction. Despite the unstructured bar showing very linear Ohmic behaviour, the resistance was much higher than expected from the measured properties of the unprocessed material. Assuming the epilayer is still 5 nm, conductivity at 4.2 K has reduced to around 14 $\Omega^{-1}\,\mathrm{cm}^{-1}$, with some inhomogeneity between different devices. This could indicate that the processing steps have resulted in a thinning of the epilayer.

While larger nanoconstrictions show behaviour very similar to the unstructured bar, the magnetotransport for the 40 nm constriction starts deviating from that. In the unstructured bar the AMR, judged from the resistance at $\mu_0 H = 0.6$ T, between the in-plane $\mathbf{H} \parallel \mathbf{x}$ and $\mathbf{H} \parallel \mathbf{y}$ orientations is about 3%, while rotating field out of plane to the $\mathbf{H} \parallel \mathbf{z}$ yields an AMR in excess of 20%. In the nanoconstriction the out-of-plane AMR is comparable to the unstructured bar, while the in-plane AMR has increased to about 6%. Even more significant changes are identified in the AMR when the field is applied along the 45° orientations. These directions represent the [110]/[1$\bar{1}$0] magnetically hard axes. The $\mathbf{H} \parallel \mathbf{x} + 45°$ orientation has become less resistive with the nanoconstriction to the extent that it has become a lower resistance state than $\mathbf{H} \parallel \mathbf{y}$. Although the $\mathbf{H} \parallel \mathbf{y} + 45°$ was the highest resistance in-plane state in both cases, the AMR between it and $\mathbf{H} \parallel \mathbf{x}$ has increased from 7% to 10%.

In addition to the modification of the AMR at high field, the low field switching behaviour has also been altered by the 40 nm nanoconstriction. Firstly, hysteresis spikes were introduced to the out-of-plane $\mathbf{H} \parallel \mathbf{z}$ magnetotransport trace. These spikes did not align with any of the hysteretic features or resistances of other orientations and occur at a higher coercive field than the hysteretic features of the in-plane orientations. The second new feature occurred with the field applied $\mathbf{H} \parallel \mathbf{y} + 45°$. Although a negative hysteretic feature was observed in this orientation in the unstructured bar, is has become exaggerated with the nanoconstriction.

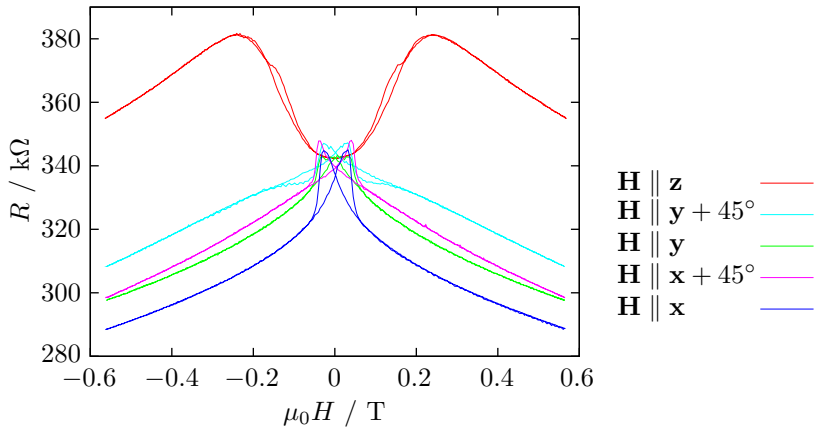

(a)

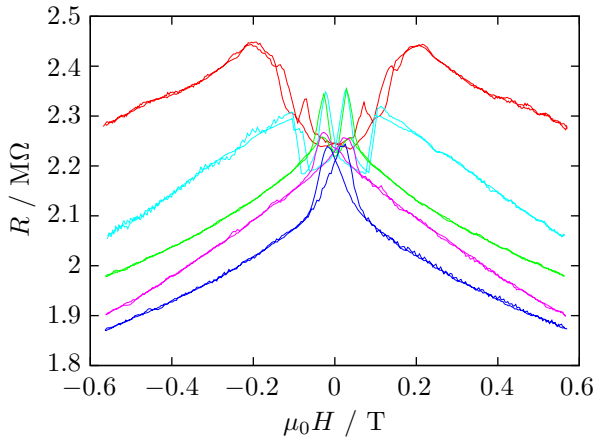

(b)

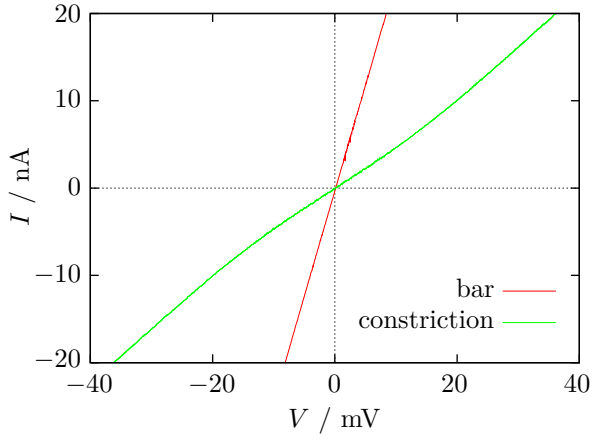

(c)

Figure 4.3: MR measurements of (a) the unstructured bar and (b) a 40 nm nanoconstriction. Field was shown applied along the cardinal directions and also the in-plane 45° angles. A 40 mV excitation was applied, $\mathbf{x} \parallel [100]$ and $T = 4.2$ K. A 5 point running average has been applied to the data in (b) to remove high frequency noise. The I-V characteristics of both devices are shown in (c).

The resistance increases until it matches that of $\mathbf{H} \parallel \mathbf{z}$ before rapidly switching to be close to the $\mathbf{H} \parallel \mathbf{x} + 45°$ and then following the hysteretic feature of the $\mathbf{H} \parallel \mathbf{y}$ orientation. Note the averaging used in Figure 4.3(b) obscures somewhat this rapid switching. Note also the rapid switch occurs at a coercive field similar to that at which the new $\mathbf{H} \parallel \mathbf{z}$ hysteretic spikes occur. Although the AMR is manifested in the low-field hysteretic switching, the additional structure is likely to be demonstrative of an additional complexity introduced by the constriction geometry into the magnetisation reversal process.

Two mechanisms are offered to explain the modifications seen in the AMR. The first is that lithographically introduced strain relaxation of the compressively strained (Ga,Mn)As layer (Wenisch *et al.*, 2007) may contribute to the anisotropy. Because of the low profile of these ultra-thin films the strain relaxation would not be expected to be great in wide structures. However, as the constrictions become smaller this profile advantage diminishes. Secondly, it is likely that shape anisotropy due to the geometry of the nanoconstriction may play a role; as the constriction is reduced in size laterally the aspect ratio of the channel formed becomes greater. Shape anisotropy has been shown to contribute to the magnetic configuration of (Ga,Mn)As for wires as large at 800 nm (Hamaya *et al.*, 2004), although it is not clear how much of that effect was actually due to local strain relaxation. However, not only may both effects be contributing to the already complex anisotropy landscape in these very small structures, but as the structure sizes are reduced the significance of the contributions from both would be expected to increase. It appears that this becomes the case when the nanoconstriction width are around 50 nm or less, yet still wide enough that the transport regime remains Ohmic.

Considering now the smaller nanoconstriction through which tunnelling transport occurs, a much greater deviation from the bulk behaviour is observed. Figure 4.4 compares the measured resistance of the unpatterned section of the Hall bar, at a constant 1 µA current, with that of the 30 nm constriction, with an excitation of 40 mV, as a magnetic field of 0.2 T was rotated in the **x**-**y** plane of the epilayer. The field strength was greater than that for which hysteresis was observed: putting the measurement outside the range of the large hysteretic effects could give a clearer indication of the AMR. The constriction showed a much larger MR than the unstructured bar, up to $\sim$ 300%. There was also much greater richness in features in the measured MR of the constriction. At such small sizes these would be strongly influenced by local fluctuations of electrostatic potential, which could change between thermal cycles or even hysteric field sweeps. De-

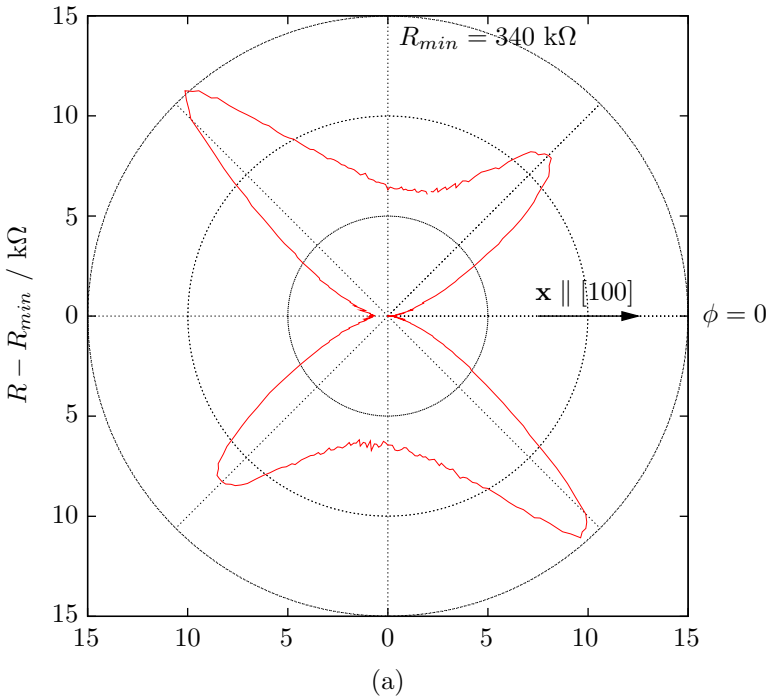

(a)

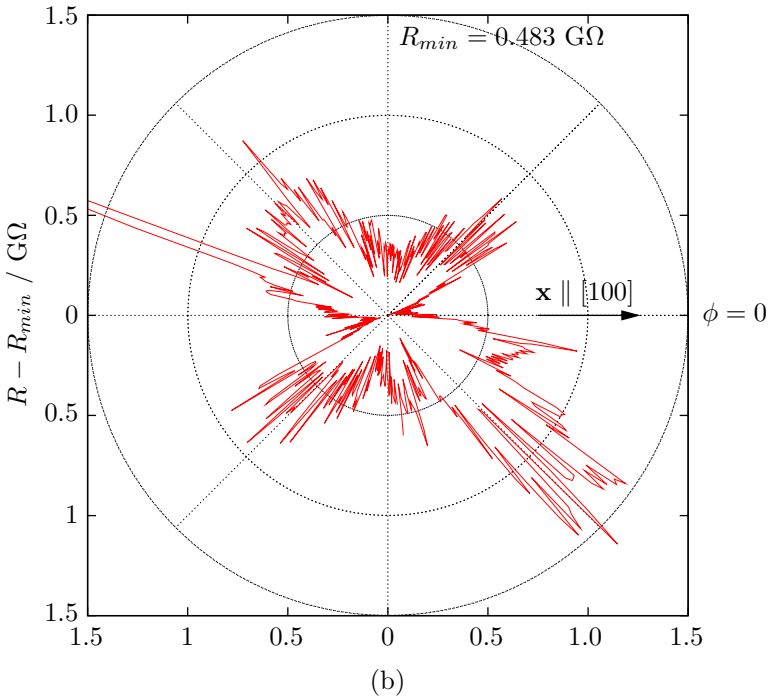

(b)

Figure 4.4: MR measurements as a 0.2 T field is rotated in the **x**-**y** plane. The angle given is between the current and field, ϕ. **x** $\parallel$ [100]. (a) unstructured bar at 4.2 K with a constant 1 µA current. (b) the 30 nm constriction at 1.5 K with an excitation of 40 mV.

spite this, there are qualitative similarities between the two traces presented in Figure 4.4(a) and (b); in both parts of the sample the highest and lowest conductances occurred along the same orientations, indicating a close link between the anisotropic magnetic properties of the constriction and bulk material. Since the magnetocrystalline components of the NAMR are dominant in these materials (Giddings *et al.*, 2005) this indicates that the observed AMR in the constriction arises from an anisotropic response of the (Ga,Mn)As material as is the case in TAMR, CBAMR and induced metal-insulator transitions. Note that the data for an unstructured bar shown in Figure 4.3(a) and that shown in Figure 4.4(a) are from different samples produced in parallel from the same substrate material. The slight differences in resistance between them, around 10%, may partly have been due to imperfections in fabrication leading to slight variations in geometries of the bars but also it may be due to spacial inhomogeneity in resistance over the surface of the wafer, something noted to occur in other devices fabricated in parallel.

The most interesting characteristic of the device is shown in Figure 4.5, where the magnetoresistance measurements of the constriction for two different thermal cycles are shown in (a)/(c) and (b)/(d), along with their respective zero field current-voltage (I-V) characteristics, (e) and (f). The exponential form of the I-V indicates tunnelling type conductivity. The differences in resistance at $\mu_0 H = 0$ T of the two cases can be partially accounted for as being due to local fluctuations of electrostatic potential during cool down, resulting in different preferred conduction paths and also the thermal cycling having potentially caused physical changes to the very sensitive nanoconstriction region (Shi *et al.*, 2007). In Figure 4.5(a)/(c) the measurement with field $\mathbf{H} \parallel \mathbf{z}$ was the highest resistance state, which was the usual behaviour for these ultra-thin films (Giddings *et al.*, 2005). In (b)/(d) this was reversed, and $\mathbf{H} \parallel \mathbf{z}$ had become the low resistance state. It is also worth pointing out that the hysteretic $\mathbf{H} \parallel \mathbf{z}$ magnetoresistance in (b)/(d) was over 1300%, which is comparable to the MR effects seen in vertical TAMR devices (Rüster *et al.*, 2005; Ciorga *et al.*, 2007b). In addition, although the $\mathbf{H} \parallel \mathbf{z}$ magnetoresistance had changed dramatically, that for the other orientations showed a much smaller deviation and $\mathbf{H} \parallel \mathbf{y}$ remained a higher resistance state than $\mathbf{H} \parallel \mathbf{x}$. This is in contrast to the effects seen in Chapter 3, where the $\mathbf{M} \parallel \mathbf{x}$ and $\mathbf{M} \parallel \mathbf{y}$ switched high and low resistance state in the TAMR regime, but $\mathbf{M} \parallel \mathbf{z}$ remained the highest resistance state.

Further insight into the unusual behaviour of this device is shown in Figure 4.6(a). This shows measurements with the field at 45° to the current, that is, along one

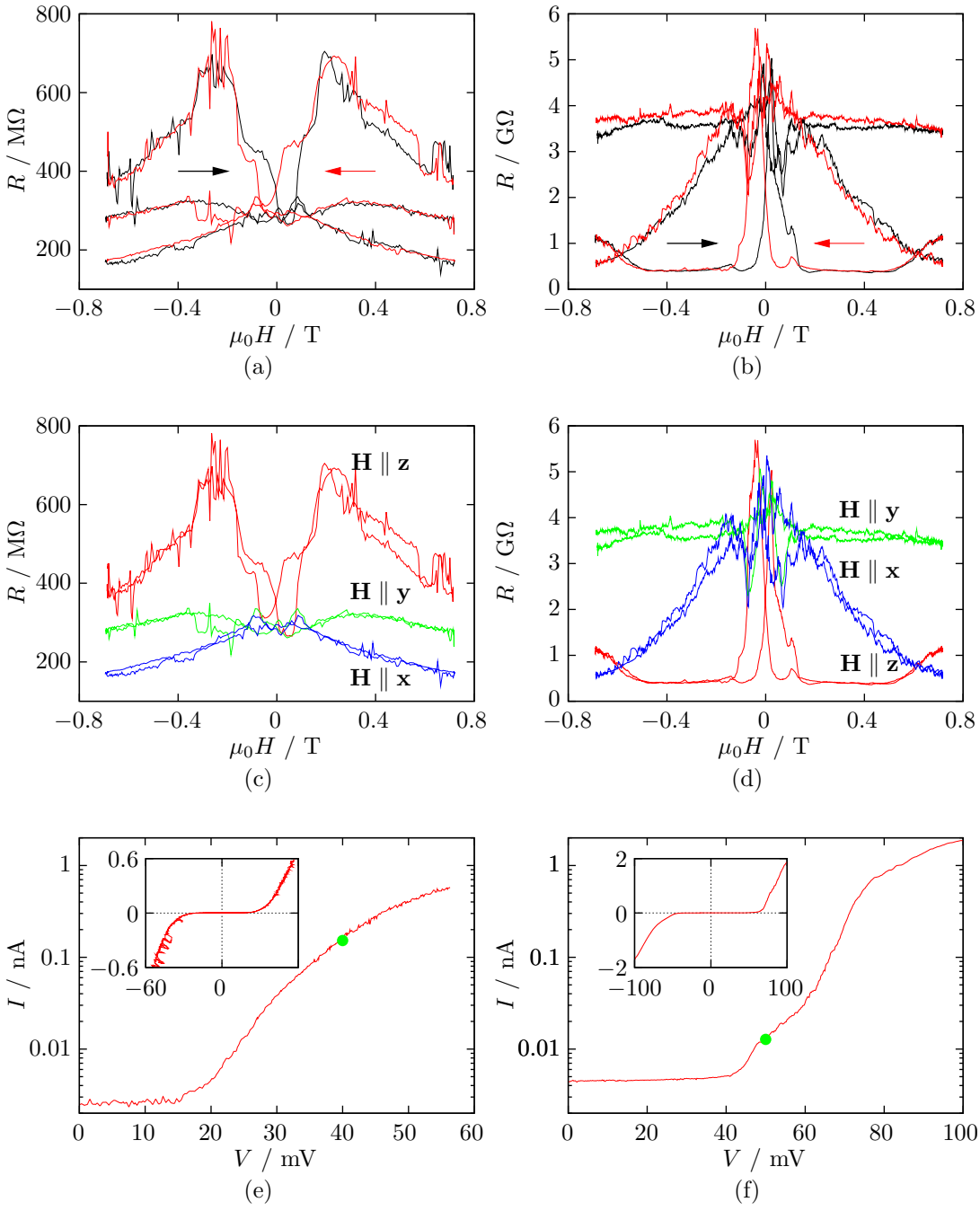

Figure 4.5: MR measurements of the 30 nm, with the field applied along the three cardinal directions **x**, **y** and **z**, but during two different thermal cycles, and the corresponding I-V characteristic at $\mu_0 H = 0$ T. To highlight the hysteretic behaviour, in (a) and (b) the black curve represents increasing field and the red curve represents decreasing field. To emphasise the anisotropic behaviour the data is replotted in (c) and (d) with the three field orientations distinguished by the different colouring. In the I-V figures, (e) and (f), the green circle marks the excitation across the nanoconstriction used for that measurement. The I-V curves have been averaged between up and down sweeps except in the case of the inset in (e) so as to preserve the switching behaviour. $T = 1.5$ K and **x** ∥ [100].

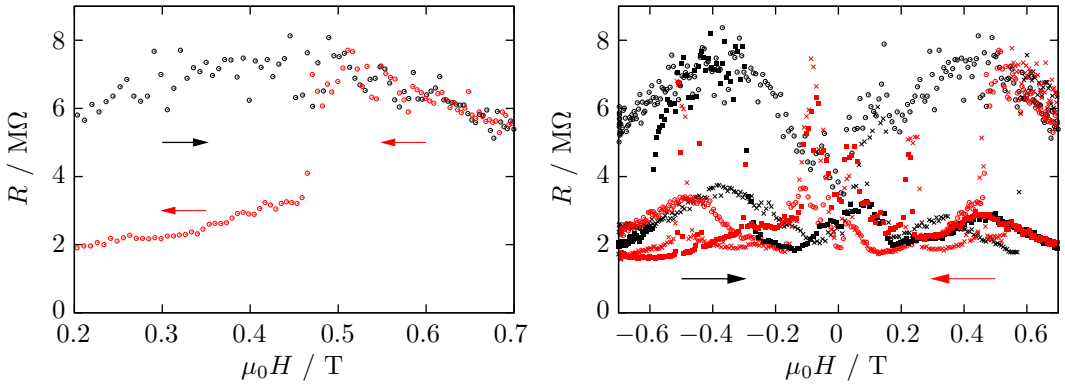

Figure 4.6: MR measurements across the 30 nm constriction fabricated from 5 nm epilayer, with the magnetic field in-plane at 45° to the direction of current, showing switching events. The excitation across the device was 40 mV and the temperature, T was 1.5 K. $\mathbf{x} \parallel [100]$. (a) focuses on a single switching event and (b) shows three sequential sweeps superimposed, highlighting the various resistance states. Black points represent increasing field and red points decreasing field.

of the in-plane $\langle 110 \rangle$ axes. Switching behaviour was observed during the measurement, whereby the sample changed between high and low resistance states, with the switching occurring on a time scale from several minutes. By overlaying several consecutive field sweeps, as shown in Figure 4.6(b), it appears that the switching was occurring between a high resistance state and several similar low resistance states. This behaviour is very reminiscent of early work in SET structures, where background charge noise would strongly feature in measurements, with telegraphic switching between two or more states (Zorin *et al.*, 1996).

4.4 Discussion

In a traditional SET structure the resistance oscillates as a function of the gate potential on the island, leading to the so-called Coulomb diamonds. In the structure studied in this Chapter there was no gate and the potential of the nanoconstriction and any nano-islands will be at an arbitrary level, depending on local electrostatic conditions which vary over different thermal cycles. It was demonstrated that the charge trapping causes large changes in the resistance in the form of multistable telegraphic switching, strongly suggesting that the movement of localised charge around the tunnelling region was changing the local potential.

This is similar to the effect of a gate in changing the local potential (Wunderlich *et al.*, 2006), and demonstrates the great sensitivity the device has to such changes.

A key feature of SET devices is the Coulomb staircase current-voltage characteristic (Matsumoto *et al.*, 1996; Smith and Ahmed, 1997), whereby discrete steps in the conductivity occur as the applied voltage is increased. This effect is due to the increasing bias overcoming the charging energy of the island, which increases by one the quantised number of charges on the island. The points of inflection in the I-V characteristic shown in Figure 4.5(f) are tantalisingly reminiscent of this. Disorder and multiple islands could be used explain the blurring of the steps, if this really were a Coulomb staircase; further investigation may be warranted. However, as discussed in Chapter 3, the TAMR mechanism in the lateral geometry of these nanoconstrictions only predicts MR of up to about 50%. This is not adequate to explain the larger MR effects seen in this device. Taking these factors together, a Coulomb blockade based transport mechanism seems to provide a better explanation of the observed behaviour.

Therefore, the dominant contribution to the MR can be considered to arise from the CBAMR mechanism (Wunderlich *et al.*, 2006; Fernández-Rossier *et al.*, 2007). In an effect analogous to the application of an electric field to the Coulomb blockade nano-island, during different thermal cycles the electrostatic configuration of the nanoconstriction can change dramatically resulting in large changes in the AMR observed. There is a strong observed link between the form of the in-plane NAMR of the bulk material and that of the constriction, and this can be accounted for through the dominance of the magnetocrystalline component of the AMR. When the field is rotated out-of-plane the shift in the chemical potential is expected to be much larger due to the strong out-of-plane anisotropies inherent in the ultra-thin films. This results in the extremely large MR effects observed in the constriction with the field in an out-of-plane configuration. Also, it would then be expected that the greatest sensitivity to charge fluctuation was for the $\mathbf{H} \parallel \mathbf{z}$ direction, as was observed.

As an aside, the TMR effects previously reported in other (Ga,Mn)As nanoconstriction devices (Rüster *et al.*, 2003; Schlapps *et al.*, 2006) shall be considered yet again. They are of particular interest as those devices contain nanoconstrictions comparable in size to the one reported in this Chapter. Recall that, in those devices there was a (Ga,Mn)As island, several orders of magnitude larger than the CBAMR nano-islands, separated from (Ga,Mn)As leads by a pair of tunnel

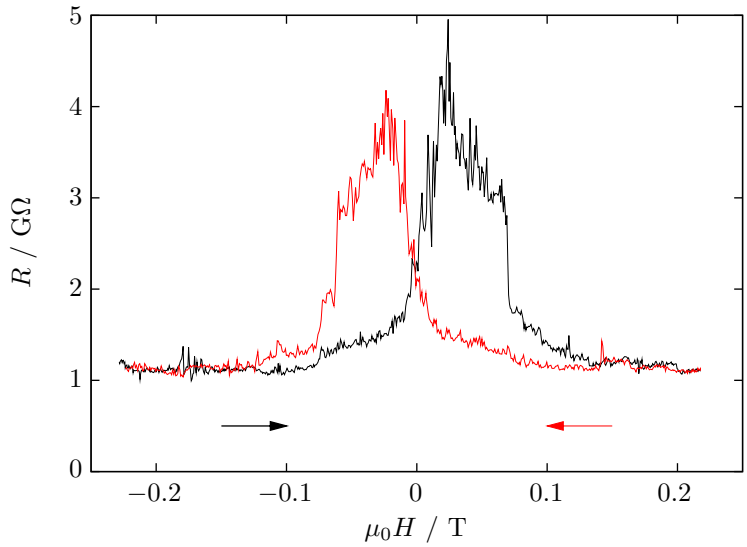

Figure 4.7: MR measurement of the 30 nm nanoconstriction with **H** ∥ **z**. **x** ∥ [100]. The four-point excitation is 40 mV and the temperature, T, is 1.5 K. The black curve is for increasing field and the red curve is for decreasing field.

barriers, that is, a pair of nanoconstrictions. Large spin-valve effects were seen, and the explanation for this was that the island and the leads would have different coercive fields due to shape anisotropy, and so this could result in either parallel or antiparallel alignment of magnetisation between the island and the leads as the field was swept. Parallel alignments were associated with a low resistance state, while an antiparallel alignment was associated with the high resistance state (Rüster *et al.*, 2003).

In Figure 4.7 the magnetoresistance trace is shown for a case with the single nanoconstriction when the field is swept with **H** ∥ **z**. Without reference to the other field orientations, the signal appears to be of a qualitatively similar nature to the spin-valve effect that a TMR device would exhibit. However, in this case the device only contains a single constriction. The leads either side were otherwise identical and as such should have identical coercive fields. Therefore, the magnetisation of the (Ga,Mn)As either side of the constriction should remain parallel. This, precludes a TMR mechanism, and suggests that the magnetoresistance effect was a property of the transport across or within the nanoscale area of nanoconstriction itself. Note that the mean free path of (Ga,Mn)As is less than 1 nm at temperatures lower than 1 K (Edmonds *et al.*, 2002b; Sørensen *et al.*, 2003) and the 5 nm film behaves as a 3D system. This highlights the difficulty in analysing TMR transport data in (Ga,Mn)As devices containing nanoconstrictions, as there is otherwise nothing to distinguish true spin-valve behaviour from

that seen in Figure 4.7.

4.5 Conclusion

Anisotropic switching behaviour has been demonstrated in (Ga,Mn)As ultra-thin film nanoscale devices, similar to those of recent interest. This has resulted in an observation of magnetoresistance effects of up to $\sim 1400\%$. The diverse MR effects that can be exhibited in lateral DMS nanostructure devices have been considered, and the results discussed in the context of those effects. By framing the phenomenology in terms of CBAMR a likely explanation for the effects is provided; this demonstrates how the bulk anisotropies of the material control transport behaviour in the tunnelling regimes of nanostructured devices.

Chapter 5

Interlayer Exchange Coupling

5.1 Introduction

The exciting new prospect of spin based electronics, known as spintronics, was initiated in 1988 with the discovery of GMR in metallic multilayer structures (Baibich *et al.*, 1988; Vélu *et al.*, 1988; Binasch *et al.*, 1989). These structures consist of interposed ferromagnetic (FM) and non-FM layers. When the magnetisation of adjacent FM layers is aligned in antiparallel directions, enhanced spin scattering of carriers causes an increased electrical resistance through the layers, while when they are parallel the resistance is lower. Although typical GMR devices today consist of a trilayer structure with a pinned magnetic layer and one in which the magnetisation is free to rotate, another method of implementation is with a superlattice structure where adjacent layers have an antiparallel magnetisation unless an external field is applied to align them.

In multilayer structures containing ferromagnetic layers, in addition to the ferromagnetic order within the layers, there can also exist magnetic exchange between the layers. The mechanism which causes the magnetic order between the layers is known as interlayer exchange coupling (IEC), and has been shown in metallic systems to be due to the spin polarisation of conduction carriers (Bruno, 1995).

Because the IEC energy considers the spin dependent changes in total energy, it thus determines which magnetic alignment of adjacent layers is energetically favourable. Although complicated helical arrangements can exist (Nunez *et al.*, 1995), typically the interlayer exchange coupling will either be FM, where there is a parallel alignment of magnetisation, or antiferromagnetic (AFM) where there is an antiparallel alignment. Therefore, in such a system, achieving AFM interlayer

coupling is of high importance for technological applications.

In addition to existing in metal systems, IEC is a generic property of magnetic multilayers, and AFM IEC has even been demonstrated in non-metallic FM semiconductor systems based on all-semiconductor EuS/PbS superlattices (Kępa *et al.*, 2001a). AFM IEC in DMS based superlattices was theoretically predicted in 1999 using a $\mathbf{k} \cdot \mathbf{p}$ kinetic-exchange model for carrier mediated ferromagnetism (Jungwirth *et al.*, 1999). This approach considers delocalised charge and adds extra modulation induced by spin-polarised effects. A large MR was predicted due to the large difference in miniband dispersion for the cases of ferromagnetically and antiferromagnetically aligned layers. Recently, IEC has been further explored using a tight-binding model (Sankowski and Kacman, 2005). This complementary microscopic approach, although not self-consistent, takes into account atomic orbitals for all the constituent atoms, leading to more accurate descriptions of the band structure. Despite the different approaches used, both methods provide qualitatively similar results for the IEC which shows oscillatory Ruderman-Kittel-Kasuya-Yosida (RKKY)-like behaviour.

Although IEC has been shown to exist in DMS systems based on (Ga,Mn)As/(Al,Ga)As trilayers (Chiba *et al.*, 2000), there have been no reports of AFM interlayer coupling. Experimental work into (Ga,Mn)As based multilayer and superlattice structures has only succeeded in demonstrating FM IEC (Kępa *et al.*, 2001b; Chung *et al.*, 2004). In order to test the prediction of a phenomenon analogous to GMR in metals in DMS materials, with a potentially much greater MR ratio, it is essential that AFM interlayer coupling is obtained.

Having explored two MR effects novel to DMS nanostructures, a somewhat abrupt departure will be taken from laterally defined structures in order to consider theoretically a fully epitaxial system. The aim of this study is to provide a comprehensive description of the multidimensional parameter space available in these DMS superlattice systems, in order to identify optimal parameters for realising an antiferromagnetically coupled system. Because the interlayer coupling is mediated by carriers, a $\mathbf{k} \cdot \mathbf{p}$ approach is more practical for exploring a wide range of parameter values. The limitation of this approach is that a single parabolic band approximation is used, sacrificing full quantitative accuracy for qualitative descriptions of a wide range of systems. Subtleties of the band-structure and spin-orbit effects are neglected. However, qualitative agreement with the data published by Sankowski and Kacman (2005) at least partially justifies this approach.

The organisation of this Chapter is as follows: first the details of the theoretical modelling of a DMS based superlattice system and the numerics of the self-consistent mean field calculations will be shown. Next, the results, which will primarily consider (Ga,Mn)As based superlattice systems with either GaAs or (Al,Ga)As non-magnetic spacer layers, will be presented. Finally, in the discussion, suggestions for recipes for superlattice systems in which antiferromagnetic interlayer coupling may occur will be given. These structures will be experimentally investigated in Chapter 6.

Some of the work in this chapter is summarised in Giddings *et al.* (2007) and a more detailed overview can be found in Giddings *et al.* (2008a).

5.2 Theoretical modelling

The calculations are based on the Zener kinetic-exchange model (Zener, 1951) description of magnetic interactions in Mn-doped III-V semiconductor structures. Microscopically, the kinetic-exchange between the local manganese moments and itinerant hole spins originates from the *p*-*d* orbital hybridisation (Jungwirth *et al.*, 2006). This model provides a good description of ferromagnetism in bulk (Ga,Mn)As.

An intuitive picture of the IEC in (III,Mn)V/III-V multilayer structures can be obtained by the perturbative mapping of the kinetic-exchange model onto an effective interaction between local moments, following the RKKY approach (Jungwirth *et al.*, 1999). The RKKY theory can be expected to provide useful predictions for structures close to a model pseudo-1D system consisting of alternating thin ferromagnetic layers and non-magnetic spacer layers such that there is small coupling and low carrier polarisation (Kittel, 1968). The RKKY range function falls off asymptotically with $\sin(2k_F d)/d^2$, where k_F is the carrier wave vector and d is the distance between the magnetic layers. Thus, the RKKY theory shows that the coupling can have an oscillatory form.

The Zener kinetic-exchange model for homogeneous (Ga,Mn)As was generalized by Jungwirth *et al.* (1999) in order to account for the RKKY-like oscillatory effects in the inter-(Ga,Mn)As coupling in (Ga,Mn)As based ferromagnetic/non-magnetic superlattices on a more quantitative level. In this model the band structure was solved using the kinetic-exchange model and a parabolic band $\mathbf{k}\cdot\mathbf{p}$ effective mass approximation. In the Hamiltonian the magnetic moments were accounted for through the *p*-*d* kinetic-exchange interaction between manganese

spins and hole spins which was parametrized by a constant J_{pd}. The value of J_{pd} can be experimentally determined, and modern estimates of this value place it at 55 meV nm^3 (Sinova *et al.*, 2004). To account for the inhomogeneity, a standard formalisation of the local-spin density approximation (LSDA) using the Kohn-Sham equations for inhomogeneous systems was used in the band structure calculations (Vosko *et al.*, 1980). Hole mass was $m^* = 0.5m_e$ and the spin of local manganese moments was $S = \frac{5}{2}$ at $T = 0$ K. Thermodynamics were treated on a mean field level.

In order to find the normalized wavefunction for a given energy, Bloch's theorem was used to solve the one-dimensional time-independent spin-dependent Schrödinger equation

$$(\frac{p^2}{2m^*} + V_\sigma(z))\Psi_{k,n,\sigma}(z) = E_{k,n,\sigma}\Psi_{k,n,\sigma}(z), \tag{5.1}$$

which can be rewritten as

$$\frac{d^2\Psi_{k,n,\sigma}}{dz^2} = \frac{2m^*}{\hbar^2}(V_\sigma(z) - E_{k,n,\sigma})\Psi_{k,n,\sigma}(z), \tag{5.2}$$

where k is the wavevector, n is the subband index, and σ is the spin index.

The Bloch function

$$\Psi_{k,n,\sigma}(z) = u_{k,n,\sigma}(z)e^{(ikz)}, \tag{5.3}$$

gives the solutions of the Schrödinger equation for a periodic potential.

For this system, the explicit form of the Hamiltonian for the spin-dependant potential $V_\sigma(z)$ is given by

$$V_\sigma(z) = V_H + V_{xc,\sigma} + V_b - \frac{\sigma}{2}[g^*\mu_B B + h_{pd}(z)], \tag{5.4}$$

where V_H is the Hartree (electrostatic) potential, given by the Poisson equation, $V_{xc,\sigma}$ is the spin-dependent exchange-correlation potential given by the LSDA equation, V_b is the band-offset, g^* is the free-carrier g-factor and h_{pd} is the mean-field kinetic-exchange interaction (Jungwirth *et al.*, 1999). The IEC energy, E_c, is defined as the difference in energy between the FM and AFM states per superlattice period.

Suppose that the one-dimensional lattice has a period d_{n+m} and consider now

the solution only at N evenly distributed discrete points on the z-axis with a separation h. The wavefunction at each point is denoted as $\Psi(z)$. By Taylor's theorem, the second approximations for $\Psi(z+h)$ and $\Psi(z-h)$ are

$$\Psi(z+h) = \Psi(z) + h\Psi'(z) + \frac{h^2}{2}\Psi''(z); \tag{5.5}$$

$$\Psi(z-h) = \Psi(z) - h\Psi'(z) + \frac{h^2}{2}\Psi''(z). \tag{5.6}$$

Taking the sum of Equations 5.5 and 5.6 obtains

$$h^2\Psi''(z) = \Psi(z+h) + \Psi(z-h) - 2\Psi(z). \tag{5.7}$$

However, from Equation 5.2 the wavefunction can be written as a function of the second derivative, so

$$\Psi''(z) = f\Psi(z), \tag{5.8}$$

where $f = \frac{2m^*}{\hbar^2}(V_\sigma(z) - E)$. Substituting this into Equation 5.7 and rearranging gives the wavefunction at a given point as a linear combination of the wavefunctions at the two previous points:

$$\Psi(z+h) = (h^2 f + 2)\Psi(z) - \Psi(z-h). \tag{5.9}$$

This linear transformation can be represented as a transfer matrix, $\mathbf{M}_n$, [1] such that

$$\mathbf{M}_n \begin{pmatrix} \Psi_n \\ \Psi_{n-1} \end{pmatrix} = \begin{pmatrix} m_{n,11} & m_{n,12} \\ m_{n,21} & m_{n,22} \end{pmatrix} \begin{pmatrix} \Psi_n \\ \Psi_{n-1} \end{pmatrix} = \begin{pmatrix} \Psi_{n+1} \\ \Psi_n \end{pmatrix}, \tag{5.10}$$

where Ψ_n is the wavefunction at the n^{th} z-point. By inspection we see that $m_{n,11} = h^2 f + 2$, $m_{n,12} = -1$, $m_{n,21} = 1$ and $m_{n,22} = 0$. It is worth noting here that the determinant of each $\mathbf{M}_n$, $\det(\mathbf{M}_n) = 1$. The product of the N transfer matrices $\prod_{n=1}^{N} \mathbf{M}_n = \mathbf{M}^T$ represents the transformation from Ψ_0 to Ψ_N. By Bloch theorem's periodic boundary condition, Equation 5.3, this transformation can be written

[1] not to be confused with magnetisation vector $\mathbf{M}$.

$$\mathbf{M}^T \begin{pmatrix} \Psi_1 \\ \Psi_0 \end{pmatrix} = \begin{pmatrix} m_{11}^T & m_{12}^T \\ m_{21}^T & m_{22}^T \end{pmatrix} \begin{pmatrix} \Psi_1 \\ \Psi_0 \end{pmatrix} = \begin{pmatrix} \Psi_{N+1} \\ \Psi_N \end{pmatrix}$$
$$= e^{ika} \begin{pmatrix} \Psi_1 \\ \Psi_0 \end{pmatrix}. \tag{5.11}$$

Therefore,

$$\begin{aligned} 0 &= \det(\mathbf{M}^T - e^{ika}\mathbf{I}_2) \\ &= (m_{11}^T - e^{ika})(m_{22}^T - e^{ika}) - m_{12}^T m_{21}^T \\ &= m_{11}^T m_{22}^T - m_{12}^T m_{21}^T - e^{ika}(m_{11}^T + m_{22}^T) + e^{2ika} \\ &= \det(\mathbf{M}^T) - e^{ika}\mathrm{Tr}(\mathbf{M}^T) + e^{2ika}. \end{aligned} \tag{5.12}$$

Since the determinant of $\mathbf{M}_n$ is 1, then the determinant of any product of $\mathbf{M}_n$, for any n, will also have a determinant of 1, hence $\det(\mathbf{M}^T) = 1$. Substituting this into Equation 5.12 gives

$$1 - e^{ika}\mathrm{Tr}(\mathbf{M}^T) + e^{2ika} = 0 \tag{5.13}$$

$$\begin{aligned} \mathrm{Tr}(\mathbf{M}^T) &= e^{ika} + e^{-ika} \\ &= 2\cos(ka) \end{aligned} \tag{5.14}$$

For a given energy, wavevector k can thus be found by

$$k = \frac{1}{a}\arccos(\frac{1}{2}\mathrm{Tr}(\mathbf{M}^T)), \tag{5.15}$$

and the corresponding wavefunction can be found similarly.

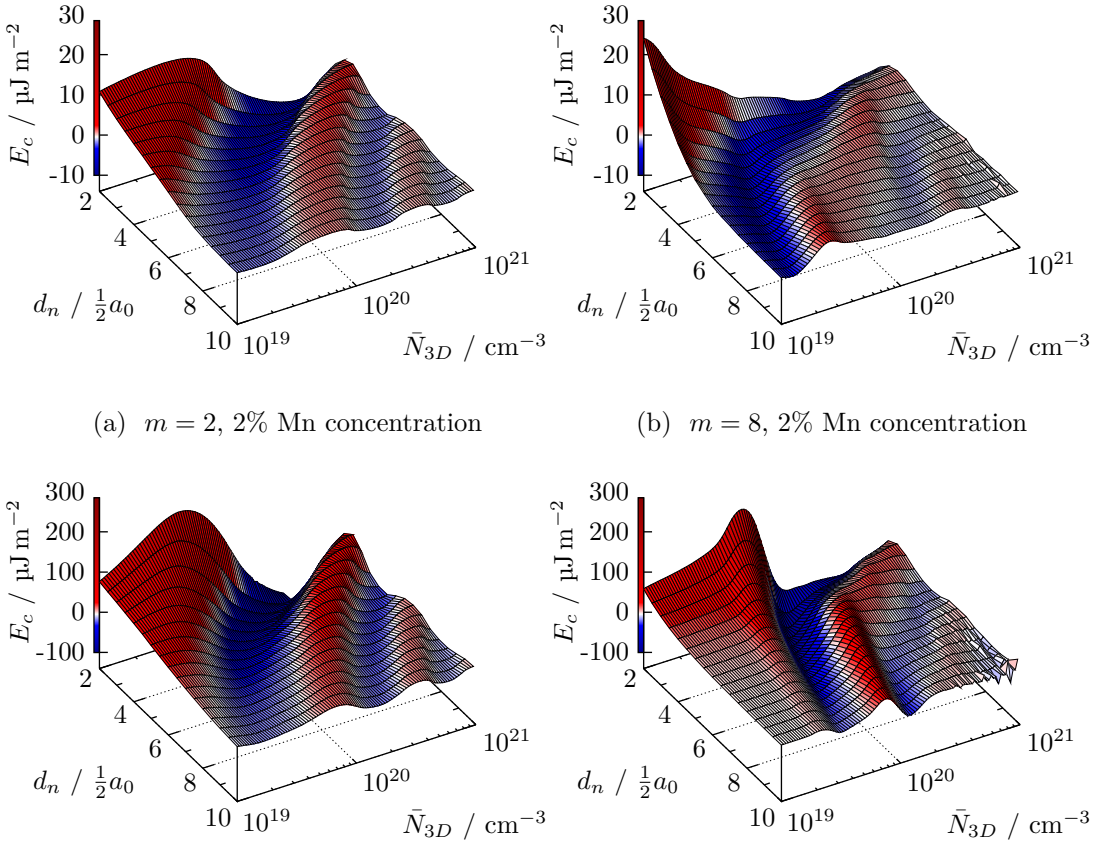

(a) $m = 2$, 2% Mn concentration

(b) $m = 8$, 2% Mn concentration

(c) $m = 2$, 8% Mn concentration

(d) $m = 8$, 8% Mn concentration

Figure 5.1: The IEC energy, E_c, as a function of the average 3D carrier concentration, $\bar{N}_{3D}$, and the number of monolayers of non-magnetic layer, $2d_n/\frac{1}{2}a_0$. Positive values of E_c, coloured red, indicate FM interlayer coupling is energetically favourable and negative values, coloured blue, indicate AFM is favourable. All the superlattices contain a uniform impurity concentration.

5.3 Results

5.3.1 GaAs spacer

In the RKKY model of interlayer exchange the oscillations occur as a function of $k_F d$, where k_F is the Fermi wave vector and d is the separation between the two-dimensional magnetic planes (Yafet, 1987). In this model d_n is used to denote the width of the non-magnetic layers, corresponding to d from the RKKY model, and d_m is the width of the magnetic layers. The length of a GaAsÂăunit cell is labelled a_0 and has a value of 0.565 nm. The average Fermi wave vector $\bar{k}_F$ shall be defined as

$$\bar{k}_F = (3\pi^2 \bar{N}_{3D})^{\frac{1}{3}}, \tag{5.16}$$

corresponding to the Fermi vector k_F in the ideal RKKY model with a parabolic band. The average 3D carrier concentration $\bar{N}_{3D}$ is defined as

$$\bar{N}_{3D} = \frac{1}{d_{n+m}} \int_{\text{unit cell}} N_{3D}(z)\, dz = \frac{N_{2D}}{d_{n+m}}. \tag{5.17}$$

First to be considered is a superlattice structure close to the RKKY limit of infinitely thin magnetic layers surrounded by free unpolarised carriers. This was modelled using thin magnetic layers and a low magnetic moment concentration. In Figure 5.1(a) the IEC energy, E_c, is plotted against the 3D carrier concentration, $\bar{N}_{3D}$, and number of monolayers of GaAs in the non-magnetic spacer, $2d_n/\frac{1}{2}a_0$. The magnetic (Ga,Mn)As layer is 2 monolayers thick and contains 2% manganese local moment doping. There is a uniform acceptor density throughout the structure which gives an average hole concentration of 4.43×10^{20} cm^{-3}. In this case there are oscillations as a function of both parameters, analogous to the $k_F d$ oscillations in the ideal quasi one-dimensional RKKY model. For the calculated IEC energy, E_c, positive values correspond to FM interlayer coupling being energetically favourable, and negative values correspond to AFM interlayer coupling being the favoured configuration.

The RKKY like behaviour observed in Figure 5.1(a) is consistent with the results obtained in the tight-binding approach (Sankowski and Kacman, 2005) when the exchange coupling energy, E_c, is plotted against the two-dimensional carrier concentration, N_{2D}, for fixed layer thicknesses. However, it is worth noting that when the exchange coupling is plotted as a function of the non-magnetic spacer

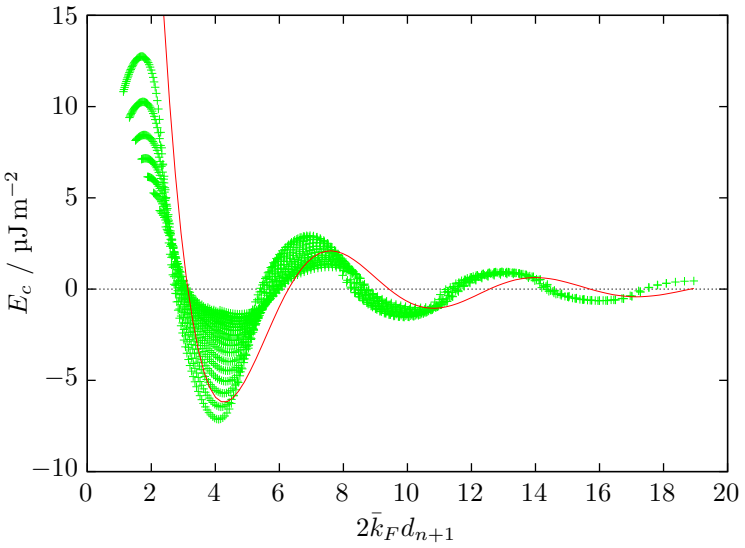

Figure 5.2: The IEC energy, E_c, as a function of $2\bar{k}_F d_{n+1}$ for a superlattice with magnetic layers with a manganese doping of 2% and 2 monolayer thickness, and a uniform impurity concentration. The red curve is an estimate of the ideal RKKY range function.

thickness, d_n, for a fixed N_{2D} there are no apparent RKKY oscillations. Because N_{3D}, and therefore k_F, is a function of d_n these two parameters are not independent when N_{2D} is fixed. This results in the oscillatory behaviour appearing to be suppressed.

There are, however, real physical reasons for deviation from RKKY behaviour. The data from Figure 5.1(a) are replotted in Figure 5.2 as a function of $2\bar{k}_F d_{n+1}$. Also plotted is the function

$$y = \alpha \frac{\sin(x)}{x^2}, \tag{5.18}$$

where α is a scaling factor. This function is the asymptotic limit of the pseudo one-dimensional RKKY range function (Yafet, 1987). The strength of the interaction is expected to scale with the density of states, and in the 1D case $\alpha \sim k_F^2$ (Dietl *et al.*, 1997). The different series of points on the graph correspond to the series of different non-magnetic spacer thicknesses shown in Figure 5.1(a). For a given $2\bar{k}_F d_{n+1}$, the points with the largest magnitude are those with the greatest k_F; this behaviour is consistent with the expected scaling of α with k_F. An important point to note is the fact that, in order to have improved alignment of the curves, the oscillations were plotted with the effective value of the non-magnetic space, d_n, being increased in size by one monolayer, and so is denoted d_{n+1}. This is necessary due to the fact that the magnetic layer in this structure

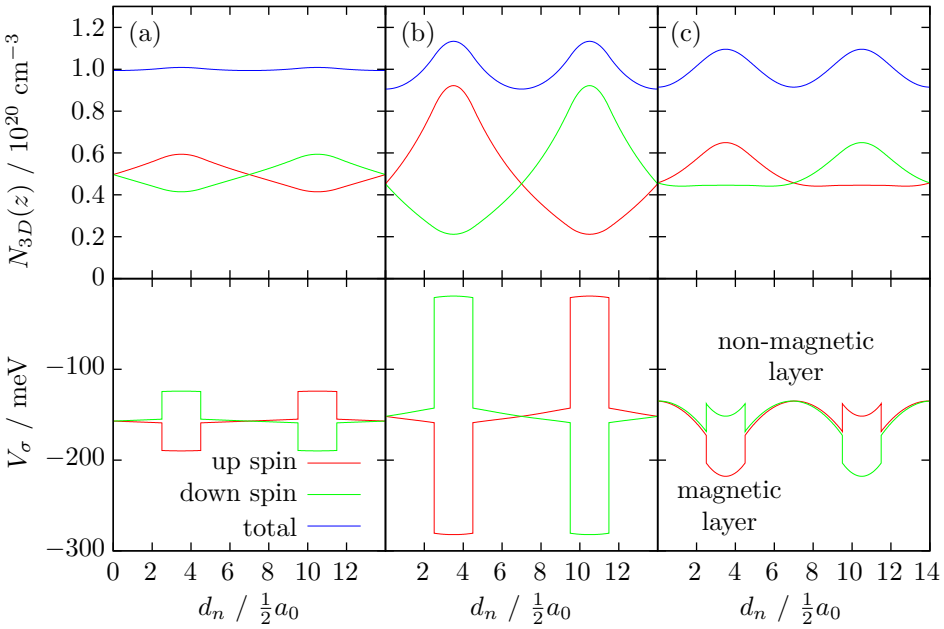

Figure 5.3: The self consistent charge distribution, N_{3D}, and potentials, V_σ, for a double unit cell of three different superlattice structures in an AFM state. $d_m/\frac{1}{2}a_0 = 2$, $d_n/\frac{1}{2}a_0 = 5$ and $\bar{N}_{3D} = 10^{20}$ cm^{-3} in each case. $V_\sigma = 0$ eV corresponds to the Fermi level. (a) 2% manganese doping and a uniform impurity concentration, (b) 8% manganese doping and a uniform impurity concentration and (c) 2% manganese doping but no impurities in the non-magnetic layer.

is not infinitely thin, as per the ideal RKKY case, but has a defined width.

Exploring this deviation from RKKY behaviour further, Figure 5.1(b) shows the IEC for a superlattice system with a thicker magnetic layer, $m = 8$. All other parameters are as with (a). Examining the AFM peak, the reduction in average carrier concentration of the minimum as the spacer thickness is increased occurs more rapidly, evidenced by the large $\frac{d\bar{N}_{3D}}{dd_n}$ of the minimum at low d_n. While at large d_n this is very low, that is the curve has become much more straight. This is consistent with the effects of large magnetic layers increasing the centre-to-centre distance of the magnetic layers, causing the effect of an apparently larger non-magnetic layer. However, in addition to this, increasing the magnetic layer thickness has introduced additional points of inflection, for reasons that are not immediately obvious.

It is also possible to deviate from RKKY-type behaviour through redistribution of charge. There are two primary methods by which this is achieved. The first is that charge is confined to the magnetic layers by the magnetic exchange potential. Figure 5.1(c) shows the IEC where the manganese doping has been increased to

8%. However, when the magnetic layer is thin, significant charge redistribution is opposed by the Coulomb potential and the RKKY character is not significantly affected. As the figure shows, the main effect is that the size of the IEC is increased. Figure 5.3(b) shows the self-consistent potential, V_σ, of a unit cell of this structure, in the case where $2d_n/\frac{1}{2}a_0 = 5$ and $\bar{N}_{3D} = 10^{20}$ cm^{-3} and the system is in an AFM configuration. The Fermi energy is at $V_\sigma = 0$ eV. For comparison, Figure 5.3(a) has the same parameters but with 2% manganese doping, that is, for the structure in Figure 5.1(a). The greater magnetic moment concentration results in a much larger spin splitting in the magnetic layers and a large polarisation of carriers. For 2% the charge distribution is almost uniform; there is appreciable redistribution in the magnetic layers. Despite this, the coupling retains an RKKY character.

When the magnetic layer is made wider the increased quantity of magnetic moments now causes additional changes in the oscillatory behaviour, beyond that of simply increasing d_m. Figure 5.1(d) plots the IEC for a system which now has magnetic layers of 8 monolayers with a manganese doping of 8%. Because of the increased depletion of carriers from the non-magnetic layers, the N_{3D} values at which AFM coupling is expected to occur are now greater for a given non-magnetic layer thickness. Additionally, the damping of the magnitude of the IEC energy with increasing d_n has now significantly changed. While the first FM and AFM maxima are rapidly diminished with increasing non-magnetic spacer, the second FM peak is not greatly affected. The second AFM peak even increases in magnitude with larger d_n, and for large spacer it can even be greater than the first.

Note that when the unit cell becomes large and there is a high carrier concentration, the weak coupling and flat minibands make self-consistent convergence difficult; these regions are visible as rough areas on the figures. No data is shown where the calculations have diverged.

The second method of charge redistribution is via a Coulomb potential. Figure 5.4(a) shows the IEC profile for a system with a magnetic spacer of two monolayers and a manganese concentration of 2%. However, now there is no neutralising background charge in the non-magnetic layer, so self-consistent redistribution results in the formation of an effective barrier. Figure 5.3(c) shows the potentials and charge distribution for a unit cell of this structure in an AFM configuration, again with $n = 5$ and $\bar{N}_{3D} = 10^{20}$ cm^{-3}. The Coulomb barrier formed is comparable in size to the spin splitting caused by the 2% manganese

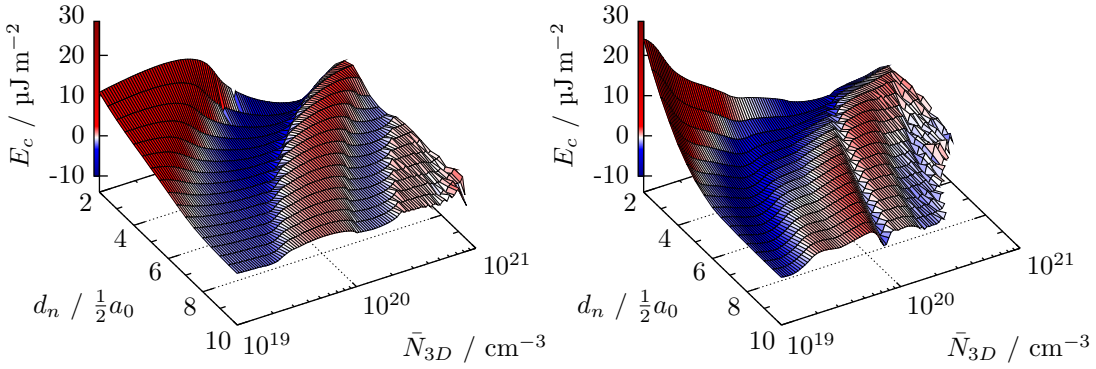

(a) $m = 2$, 2% Mn concentration

(b) $m = 8$, 2% Mn concentration

Figure 5.4: The IEC energy, E_c, as a function of the average 3D carrier concentration, $\bar{N}_{3D}$, and the number of monolayers of non-magnetic layer, $2d_n/\frac{1}{2}a_0$. There is no charge doping in the non-magnetic layer.

doping. This results in a similar charge redistribution as in the 8% doped case, although without such strong carrier polarization. As with that case, there is not a significant deviation from RKKY-type behaviour.

Increasing the magnetic spacer thickness now causes more significant changes than seen with the doped spacers. Figure 5.4(b) shows the IEC profile for a superlattice with $m = 8$ with a 2% manganese doping and no impurities in the non-magnetic spacer. In addition to the extra inflection points there is now an additional AFM region. The magnitude of the local minimum in this region does not decrease much with non-magnetic spacer width, and occurs with an almost linear $\frac{d\bar{N}_{3D}}{dd_n}$. This is now very unlike RKKY behaviour.

To investigate this further, superlattices with (Al,Ga)As non-magnetic spacers will now be considered, so that greater charge redistribution should occur than caused by the magnetic ordering potential of a high magnetic moment concentration, or the Coulomb potential arising from an undoped spacer.

5.3.2 (Al,Ga)As spacer

In the previous section it was demonstrated that interlayer coupling in superlattice structures would have an oscillatory behaviour as a function of parameters $\bar{N}_{3D}$ and d_n, analogous to that of RKKY, when the magnetic layers were thin and surrounded by charge. As the structure of the superlattice is changed the IEC would start to deviate from the ideal RKKY behaviour. This is particularly

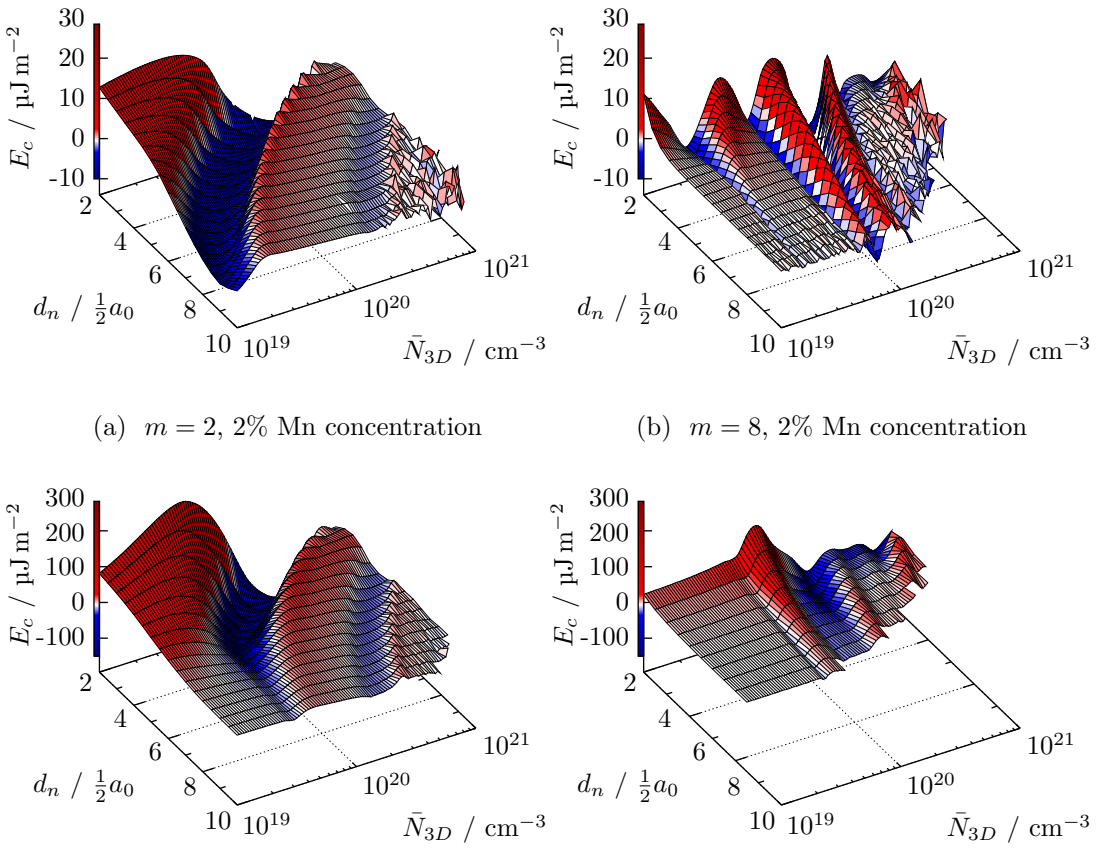

(a) $m = 2$, 2% Mn concentration

(b) $m = 8$, 2% Mn concentration

(c) $m = 2$, 8% Mn concentration

(d) $m = 8$, 8% Mn concentration

Figure 5.5: The IEC energy, E_c, as a function of the average 3D carrier concentration, $\bar{N}_{3D}$, and the number of monolayers of non-magnetic layer, $2d_n/\frac{1}{2}a_0$. The non-magnetic layers are $(Al_{0.3},Ga_{0.7})As$.

apparent with increased magnetic layer thickness. Changing the 3D charge distribution has a more limited effect; neither large magnetic moment concentration nor a self-consistent Coulomb barrier would cause significant confinement of carriers. In order to investigate these effects further, a band offset will be introduced to further confine carriers to the magnetic layers. This will be achieved by using ($Al_{0.3}$,$Ga_{0.7}$)As as the non-magnetic layer material, which has a valence band offset of about 150 meV from GaAs (Batey and Wright, 1986; Vurgaftman *et al.*, 2001).

Figure 5.5(a) shows the IEC profile for a structure with a ($Ga_{0.98}$,$Mn_{0.02}$)As magnetic layer of 2 monolayers and an ($Al_{0.3}$,$Ga_{0.7}$)As non-magnetic layer. There is no doping in the non-magnetic layers. The peak FM and AFM coupling strengths are now stronger than in the case with doped GaAs spacers seen in the otherwise identical structure in Figure 5.1(a). Considering the charge distribution, shown in Figure 5.6(a), the barrier confines carriers to the magnetic layers, as expected. However, the $2\bar{k}_F d_n$ oscillations are damped more rapidly than with the GaAs spacer, resulting in the second FM and AFM peaks being very weak. This additional damping occurs particularly rapidly with increasing carrier density, $\bar{N}_{3D}$. As a result, the first AFM peak barely reduces in magnitude as the non-magnetic layer thickness is increased. This is in stark contrast to the GaAs barrier case, where the largest AFM coupling that can occur when $n = 10$ is less than a quarter of the size of that when $n = 2$.

Increasing the magnetic moment concentration leads to a more interesting alteration than with the GaAs spacer, where the effect was principally to scale up the magnitude of the IEC energy. Figure 5.5(c) shows the IEC for a (Ga,Mn)As/(Al,Ga)As superlattice with an 8% manganese doping in the 2 monolayer magnetic layer. Now the first AFM peak appears to have two stages. The first is at low spacer thicknesses, where the average hole density at which the maximum occurs decreases with increasing spacer thickness. For large spacer thicknesses the curve has straightened out, and there is almost no dependence on d_n for the sign of the coupling. This characteristic is similar to that exhibited in Figure 5.1(b) and (d), where the magnetic layer is 8 monolayers thick. This was attributed to loss of independence of the d_n and $\bar{N}_{3D}$ parameters, as the system became less RKKY-like. Figure 5.6(b) shows the band structure and carrier distribution for this system in an AFM state when $n = 5$ and $\bar{N}_{3D} = 10^{20}$ cm^{-3}. This shows that the band offset and large magnetic ordering causes significant carrier redistribution. Particularly, this means that the carrier concentration in the spacer will decrease as a function of spacer thickness, which accounts for the weak depen-

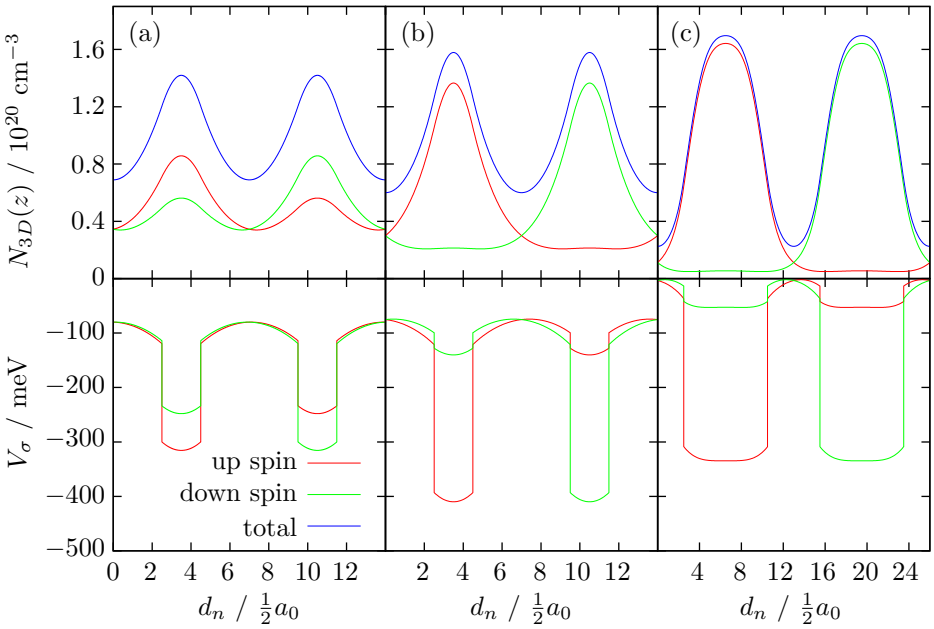

Figure 5.6: The self-consistent charge distribution, N_{3D}, and potentials, V_σ, for a double unit cell of three different superlattice structures in an AFM state. $d_n/\frac{1}{2}a_0 = 5$ and $\bar{N}_{3D} = 10^{20}$ cm^{-3} in each case. $V_\sigma = 0$ eV corresponds to the Fermi level. (a) $d_m/\frac{1}{2}a_0 = 2$ and 2% manganese doping (b) $d_m/\frac{1}{2}a_0 = 2$ and 8% manganese doping (c) $d_m/\frac{1}{2}a_0 = 8$ and 8% manganese doping.

dence of E_c on $k_F d_n$. Also, note that the size of the first AFM peak decreases more rapidly at high spacer thicknesses where the $\bar{N}_{3D}$ at which it occurs is not decreasing. This is consistent with the previous observation of enhanced damping with increasing carrier concentration.

With high magnetic layer thicknesses the RKKY-type oscillations have almost completely disappeared. The beating patterns which were emerging in the $m = 8$ GaAs spacer cases have now come to dominate the IEC. Figure 5.5(b) and (d) shows this for $m = 8$, with respectively 2% and 8% manganese doping. In these cases the oscillations occur almost exclusively as a function of hole density, being almost independent of the spacer thickness. Note, however, as can be seen in Figure 5.6(c), the non-magnetic layer is highly depleted when the magnetic layer is 8 monolayers thick with an 8% manganese doping. This makes computing IEC for larger spacers unfeasible.

5.4 Discussion and recipes

Having explored the parameter spaces, possible structures of a (Ga,Mn)As based superlattice that would exhibit AFM interlayer coupling will now be explored. Each parameter will be considered for feasibility, and, based on the above calculations, suggestions for values can be made.

The first to be considered is the manganese concentration in the (Ga,Mn)As layers. From the viewpoint of simply creating a viable ferromagnet this is an essential parameter; not only does each substitutional manganese provide a magnetic moment, it also acts as an acceptor and thus this factor controls the hole concentration. Calculations (Jungwirth *et al.*, 2005) estimate that the minimum hole density for ferromagnetism is $\sim 10^{20}$ cm^{-3}. Assuming that each manganese provides one hole, this carrier concentration would correspond to a moment concentration of $\sim 0.5\%$. Experimentally, typical manganese concentrations are in the range of 2-8%. In the calculation we considered carrier concentrations in the range of 10^{19} to 10^{21} cm^{-3} (0.045% to 4.5%). While the higher magnetic moment concentration can increase the size of the E_c peak, and thus a high moment concentration is favourable, the high carrier concentrations that would be associated with this would cause the strength of the IEC to become extremely weak. This constraint therefore imposes a practical range for manganese concentrations as being between 2 and 4% (4.4×10^{20} to 8.8×10^{20} cm^{-3} respectively).

For the non-magnetic spacer thickness the general trend is that the strength of the IEC becomes weaker as the non-magnetic layer becomes thicker. Although this effect is somewhat diminished for the cases where there is strong carrier confinement to the magnetic layers, it is a serious consideration and, ideally, to see strong IEC effects, the non-magnetic layer should be as thin as possible. Furthermore, particularly in cases where the $2k_F d$ behaviour is dominant, as carrier concentration increases the spacer thickness at which the AFM IEC is strongest decreases inversely. As discussed above, low carrier concentrations are not possible, so therefore it would seem beneficial to make the spacer layers as thin as practical. Bearing in mind that the average distance between two manganese atoms when the concentration is 3% is of the order of a couple of GaAs unit cells, in order to make the non-magnetic spacer a discernible barrier then 4 monolayers would seem to be a realistic lower bound.

The effect of the magnetic layer thickness on the IEC profile is more subtle, and seems mainly to distort the RKKY behaviour but otherwise in the limits con-

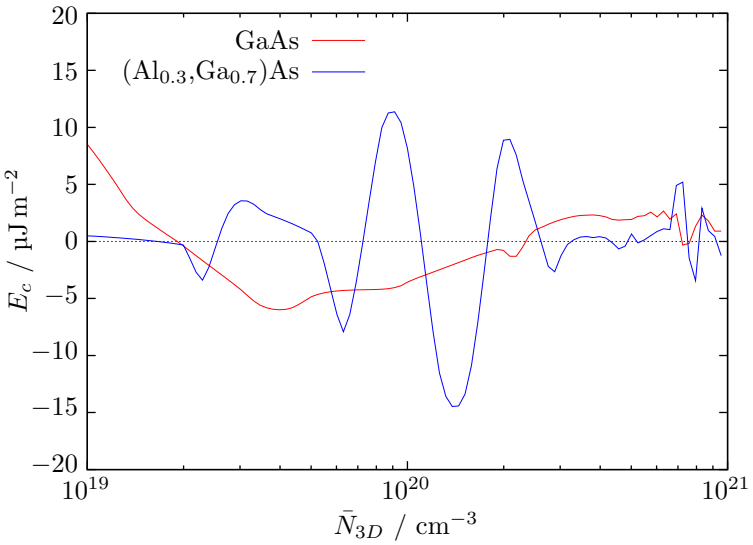

Figure 5.7: A comparison of the IEC energy, E_c, as a function of the average 3D carrier concentration, $\bar{N}_{3D}$, for two specific superlattices with either a GaAs or an $(Al_{0.3},Ga_{0.7})As$ non-magnetic layer. Neither has any doping in the non-magnetic layer. The magnetic layers are 8 monolayers thick and have a manganese concentration of 5×10^{20} cm^{-3} (2.26%) and the non-magnetic layer is 4 monolayers thick.

sidered within this study does not have any negative effects on the interlayer coupling. However again for interlayer coupling to exist it is necessary that each magnetic layer is itself ferromagnetic. Usually (Ga,Mn)As is grown in bulk layers of many nanometres; the thinnest (Ga,Mn)As epilayers for which published literature exists are 5 nm thick (Giddings *et al.*, 2005). It would therefore seem prudent, in order to ensure that the magnetic layers are effective ferromagnets, to prefer to make them thicker. For the 5 nm film some amount of surface depletion should be expected, so a 8 monolayer thick magnetic layer, equivalent to 2.26 nm, is comparable. Of course, if thinner films are shown to be viable then there is no reason not to consider them also.

Based on these constraints, Figure 5.7 shows the IEC profile for two candidate superlattices as a function of carrier concentration, N_{3D}. Both superlattices are identical in structure except for the composition of the non-magnetic layer. The magnetic layer thickness is 8 monolayers and has a magnetic impurity concentration of 5×10^{20} cm^{-3} (2.26%) and the non-magnetic layers are 4 monolayers thick. As expected from the calculations, when the (Al,Ga)As barriers strongly confine carriers to the magnetic layers the IEC energy can have potentially greater magnitudes, although the oscillations have a much higher frequency. In these samples the carrier concentration would be somewhere below the manganese concentration

of 5×10^{20} cm^{-3} (2.26%), however the exact amount would depend on subtleties of the growth conditions. Although this suggests that for AFM IEC to occur the desired carrier concentration should be several times lower, it must be accepted that the calculations are of a more qualitative nature. Additionally, by tailoring the band offset of the non-magnetic layer by altering the aluminium content, the location of the peak can be adjusted somewhat. This at least shows that these designs offer the possibility for AFM interlayer coupling.

Even if the IEC energy were to favour an AFM arrangement, if the AFM coupling is weaker than the anisotropy fields it is possible that, after the application of a field, the superlattice could become locked into a FM spin configuration. This spin-locking behaviour has been observed in EuS/PbS superlattices (Kępa *et al.*, 2001a) and Fe/Nb multilayers (Rehm *et al.*, 1997) studied via neutron scattering.

Comparing, then, the calculated IEC to the magnetocrystalline anisotropic energy of (Ga,Mn)As, we take a typical "worst case" value of the in-plane cubic anisotropy constant to be of the order of 2000 J m^{-3} at 4.2 K (Wang *et al.*, 2005b). Using a value of the interlayer coupling energy $E_c = 10$ µJ m^{-2} from Figure 5.7 and using the bilayer period of 3.4 nm we find the energy density of the IEC energy is 3000 J m^{-3}. Although this is assuming an ideal value of E_c, this compares favourably with the anisotropy energy. Furthermore, larger values for the IEC have been found in the tight-binding approach (Sankowski and Kacman, 2005). Therefore, such a superlattice structure might reasonably be expected to be a candidate to exhibit AFM interlayer coupling.

5.5 Conclusion

The composition and structure of (Ga,Mn)As based superlattices can have profound effects on the expected IEC. By examining possible compositions within the broad parameter space that these structures offer it is possible to identify different recipes for devices that might offer the possibility of demonstrating AFM interlayer coupling. If this could be realised then it could herald a dramatic new MR effect unique to DMS superlattice structures. Experimental efforts aimed towards achieving this are discussed in Chapter 6.

Chapter 6

Multilayers

6.1 Introduction

There is a rich field of study based around the physics of superlattice devices composed of (Al,Ga)As and GaAs. Because the difference in lattice parameters between AlAs and GaAs is less than 1% (Schulman and McGill, 1979) heterostructure interfaces between these materials contain a low density of defects (Adachi, 1985). Applications of this type of structure include modulation doped field effect transistors, heterojunction bipolar transistors, resonant tunnelling transistors and quantum well lasers (Adachi, 1993, p. viii). A particular advantage of this system is that, because GaAs and (Al,Ga)As are lattice matched for all aluminium concentrations, the band structure can be tailored by changing the aluminium concentration without detrimental effects to the other physical properties.

One of the oft-touted benefits of DMSs, such as (Ga,Mn)As, over traditional metal spintronic systems is the fact that it is readily compatible with existing mature semiconductor technologies (Jain *et al.*, 2001; Li *et al.*, 2005). Given the successes of both (Ga,Mn)As and GaAs/(Al,Ga)As heterostructure based devices, the magnetic counterpart to these superlattices becomes an obvious avenue of exploration, exploiting the natural synergy of these two semiconductor technologies.

A particularly promising application of magnetic/non-magnetic semiconductor superlattices is a theoretically predicted MR analogous to GMR in metal superlattices (Jungwirth *et al.*, 1999). This new MR arises from the formation of AFM IEC between the adjacent magnetic layers. A much narrower miniband bandwidth associated with this state, in comparison to a FM state, implies a large

change in conductivity could be possible.

Even without AFM IEC, a (Ga,Mn)As heterostructure potentially offers a further useful spintronic functionality. Because the carriers are bonded antiferromagnetically to the moments, the holes with spin parallel to the average magnetisation will be repelled into the non-magnetic layers and the holes with antiparallel spin will be attracted. As a result the antiparallel to average magnetisation aligned holes will have a much higher mobility (da Cunha Lima, 2003). This would therefore make a (Ga,Mn)As based superlattice an excellent device for creating a spin-polarised current.

Another exciting prediction for ferromagnetic semiconductor superlattices is the enhancement of Curie temperature, T_C, over that of bulk material (Vurgaftman and Meyer, 2001). This prediction concerns a so-called "digital" approach, where the ferromagnetic layers are extremely thin, less than 10 monolayers. The origin of the enhancement is the creation of a potential well for the holes, confining them to the magnetic layers and thus increasing the hole concentration in them. A consequence of this prediction is that the use of a non-magnetic layer with a greater valence band offset, such as (Al,Ga)As, would increase the confinement and thus the T_C. Curie temperatures of over 400 K have been predicted for superlattices with AlAs barriers and (Ga,Mn)As layer thicknesses of 2 monolayers (Vurgaftman and Meyer, 2001).

Several studies have been made into (Ga,Mn)As based superlattices. Initial attempts to create such devices using AlAs non-magnetic layers reported that wide (Ga,Mn)As layers greater than 7 nm ($\sim$ 25 monolayers) were ferromagnetic at low temperatures, while thinner layers less than 5 nm ($\sim$ 18 monolayers) remained paramagnetic even at temperatures as low as 2.0 K (Hayashi *et al.*, 1997). Additionally, evidence of quantum confinement and the formation two-dimensional subbands were demonstrated through magnetic circular dichroism (MCD) measurements.

Further experimental work in this field by Sadowski *et al.* (2002) showed that (Ga,Mn)As/GaAs based superlattices with ultra-thin films as thin as 8 monolayers could be ferromagnetic at low temperatures, for sufficiently thin GaAs spacer layers; when the non-magnetic spacer was larger than 10 monolayers the ferromagnetic phase disappeared. Interestingly, with a 4 monolayer spacer the T_C was reported to be higher than for bulk (Ga,Mn)As with the same manganese concentration, in qualitative agreement with the prediction of Vurgaftman and Meyer (2001).

As for IEC, various studies of ferromagnetic semiconductor superlattices have shown the existence of interlayer coupling between the ferromagnetic layers. Experimental techniques include neutron scattering and polarised neutron reflection (Szuszkiewicz *et al.*, 1998; Kępa *et al.*, 2001b), asymmetric trilayers (Chiba *et al.*, 2000), and the use of a *p*-type dopant in the non-magnetic layer (Chung *et al.*, 2004). However, there has been no reports of AFM coupling.

Further theoretical work into (Ga,Mn)As based superlattice systems (Giddings *et al.*, 2008a) further explored the dependence of IEC on the constituents of the superlattice. Of specific interest was the fact that, as with traditional GaAs/(Al,Ga)As superlattices where specific heterojunction properties could be engineered through the aluminium concentration, the properties of the IEC in the magnetic superlattices could be tailored in the same way. This Chapter represents a continuation of this work into the experimental domain. Described are the initial attempts to study the properties of such superlattices with the intention to show AFM IEC.

6.2 Samples

The design of the superlattice structure was conceived following the recipe proposed in Giddings *et al.* (2008a) and Chapter 5. Based on the mean field calculations, this suggested that the superlattice period sizes at which AFM IEC could be observed would require both the magnetic and non-magnetic layers to be extremely thin. The use of thin layers was supported by the work of Sadowski *et al.* (2002) where (Ga,Mn)As superlattices with magnetic layers of 8 monolayers and non-magnetic layers of 4 monolayers were shown to be viable ferromagnets. These dimensions have extremely good agreement with those favoured by the calculations.

Diffusion of manganese into the barrier is a serious consideration in (Ga,Mn)As/GaAs superlattices (Mikkelsen *et al.*, 2004). Where this happens strong ferromagnetic coupling could be expected throughout the structure, something undesirable for the demonstration of AFM coupling. To attempt to reduce the effect of this to a minimum a low manganese concentration was chosen for the magnetic layers since the proportion of interstitial manganese defects increases with total manganese concentration (Yu *et al.*, 2002). For total concentrations of 2% almost all manganese are expected to be substitutional (Wang *et al.*, 2004). Furthermore, a higher growth temperature can be used for (Ga,Mn)As with a low manganese

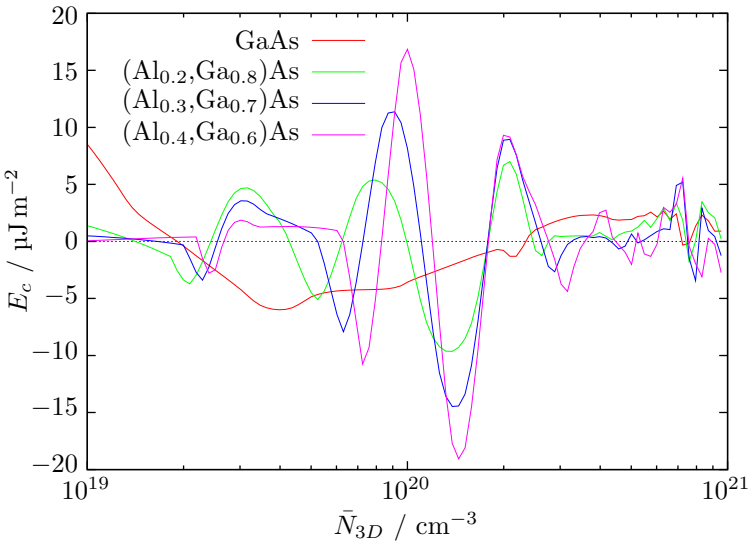

Figure 6.1: A comparison of the IEC energy, E_c, as a function of the average 3D carrier concentration, $\bar{N}_{3D}$, for four specific superlattices when changing the aluminium composition of the (Al,Ga)As non-magnetic layer. The magnetic layers are 8 monolayers thick and have a manganese concentration of 5×10^{20} cm^{-3} (2.26%) and the non-magnetic layer is 4 monolayers thick.

concentration, reducing the number of undesirable arsenic anti-site defects.

As shown in Figure 6.1, the profile of the IEC can be tailored by band-offset engineering through changing the composition of the non-magnetic layer. These simulated superlattices have 8 monolayer magnetic layers and 4 monolayer non-magnetic layers. The manganese concentration is 2.26% and the aluminium concentration in the non-magnetic layers is varied between 0% and 40%. Around 45% Al the bandgap between GaAs and (Al,Ga)As becomes indirect (Ekpunobi and Animalu, 2002). In addition to offering a possibility to explore the IEC, superlattices based on these short period designs could test the prediction of Vurgaftman and Meyer (2001) that increasing the confinement of carriers would improve T_C.

The superlattice samples were grown via low temperature MBE. They each consisted of 50 magnetic (Ga,Mn)As layers separated by a non-magnetic layer, as shown in schematic Figure 6.2. Before the first magnetic layer there was a 2 nm low temperature GaAs layer and a non-magnetic layer, and the samples were topped with a non-magnetic layer and a 10 nm low temperature GaAs cap. The magnetic layers were grown to be 8 monolayers (2.26 nm) and the non-magnetic layers 4 monolayers (1.13 nm).

The first superlattice sample, Mn-279, was grown with with a Veeco Gen-II MBE system. The manganese concentration in the magnetic layers was estimated to

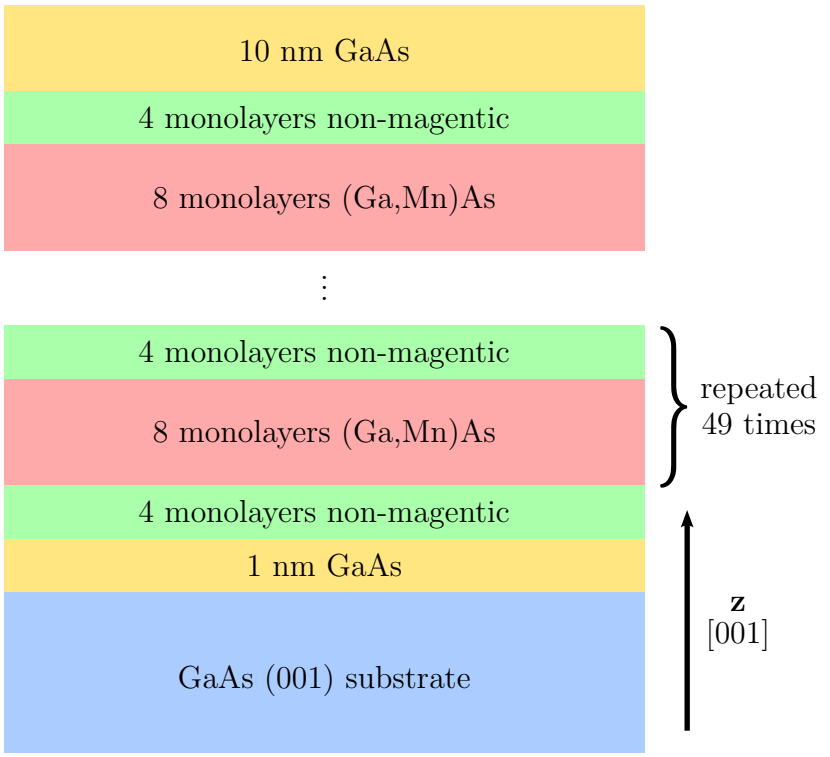

Figure 6.2: Schematic showing the epitaxial growth details of the superlattice layers.

be between 2.2 and 2.4% and the aluminium concentration in the non-magnetic layers was 30%. Subsequent samples Mn-340 through Mn-343 were all grown with the Gen-III system, offering greater control over growth conditions. Manganese concentration in the magnetic layers was intended to be 2.25%. The aluminium concentration in the non-magnetic layers was varied between 0 and 40%. The Gen-II superlattice sample was grown without rotation, resulting in some systematic spatial inhomogeneity in properties over the surface of the wafer.

In addition to these superlattices, two samples were grown to represent an isolated period and a double period. These consisted of a single magnetic layer (Mn-426) and a double magnetic layer with a 4 monolayer GaAs non-magnetic spacer (Mn-427). These ultra-thin layers were embedded in 500 nm of GaAs. The manganese concentration and layer thickness were the same as those of the magnetic layers of the superlattice.

6.3 X-ray

The superlattice samples were characterised via X-ray diffraction (XRD) techniques.

The (004) XRD measurements characterising the structure of the initial superlattice is shown in Figure 6.3. These data are from the central part of that sample. Overlaid on the measured XRD spectra is a simulated fit which reproduces well both the satellite peaks, seen in (a) and the fringes detailed in (b). The good agreement between the measured and fit data indicates that the superlattice is of excellent structural quality and periodicity, with well defined interfaces between the magnetic and non-magnetic layers.

The fitting is based on three principle features in the XRD data. The satellite peaks show the bilayer thickness. The offset from the first fringe and the tall spike caused by the GaAs substrate indicates the strain, from which the manganese concentration can be determined. The secondary or "thickness" fringes show the total thickness. The fitting assumes no interdiffusion of atoms.

Because the initial superlattice sample was not rotated it showed systematic variations over the surface of the quarter wafer in both layer thicknesses and manganese concentration in the magnetic layer. From the simulated fit, the bilayer thickness varied from 3.2 to 3.6 nm, which compares favourably with the intended 12 monolayers (3.4 nm) thickness. For the individual layers, the magnetic layers varied between 2.0 and 2.4 nm and the non-magnetic layers varied between 1.1 and 1.5 nm. The manganese concentration ranged from 2.5 to 3.0%. This value is slightly higher than the expected concentration of 2.2 to 2.4%.

The aluminium concentration was determined from the aluminium flux on the MBE cell, which was calibrated via XRD on a separately grown (Al,Ga)As epilayer. Based on that calibration the aluminium concentration in the non-magnetic layers was assumed for the fitting to be 35%.

The XRD data for the second series of superlattice samples, which were grown in the Gen-III MBE system are plotted, along with the calculated fits, in Figures 6.4. The fits are made assuming an ideal case for the structural parameters, so that the magnetic layers are 2.26 nm thick, the non-magnetic layers are 1.13 nm thick and the aluminium concentration is as intended. From the fits the manganese concentration can be estimated, and these results are shown in Table 6.1. As with the initial Gen-II grown sample, the manganese concentration appears to be slightly higher than the intended value.

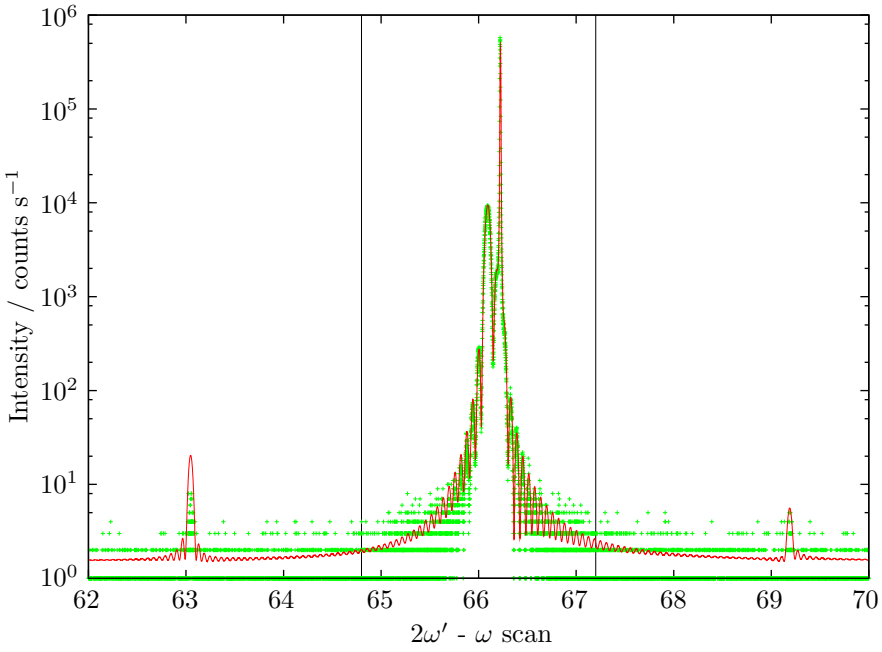

(a)

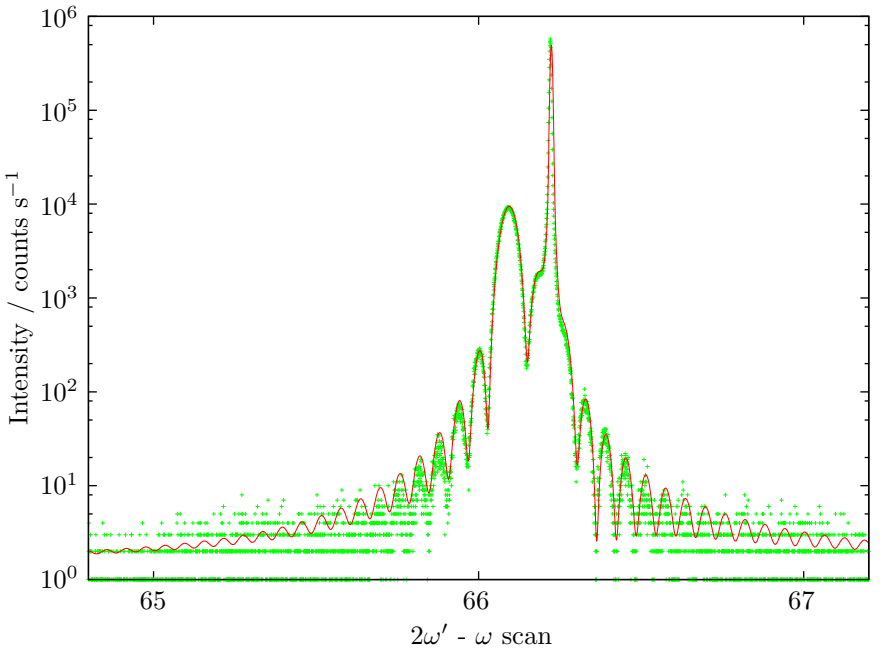

(b)

Figure 6.3: XRD (004) data for the initial superlattice sample. The red curve is the fit. (a) shows the whole range and (b) shows a close up of the central region. ω is the X-ray incident angle and ω' is the X-ray scattering angle.

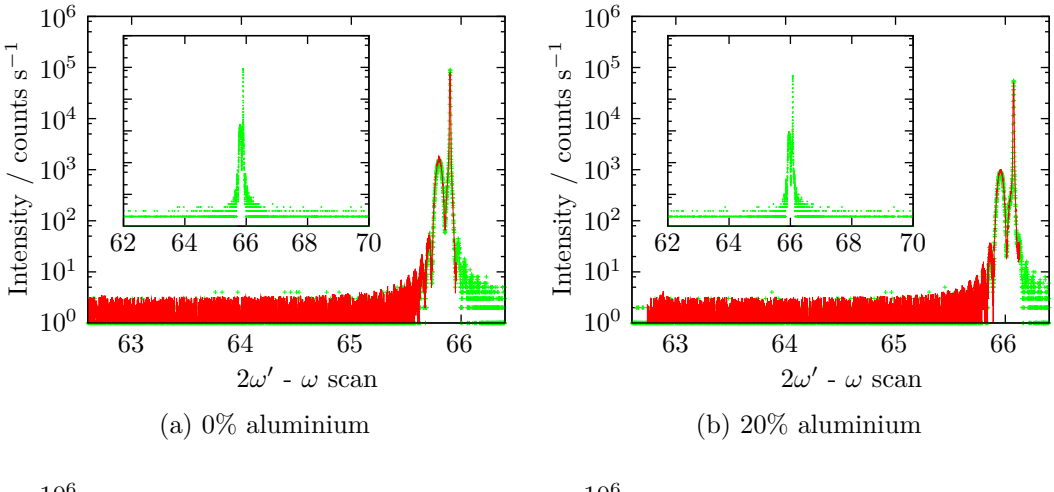

(a) 0% aluminium

(b) 20% aluminium

(c) 30% aluminium

(d) 40% aluminium

Figure 6.4: XRD (004) data for the second series of superlattice samples. The red curve is the fit. The main panel shows the measured data with a half fit; the inset shows the measured data over the full range. ω is the X-ray incident angle and ω' is the X-ray scattering angle.

% Al non-magnetic layer	% Mn concentration
0	2.7
20	3.0
30 (a)	2.5 - 3.0
30 (b)	3.0
40	2.8

Table 6.1: Estimated manganese concentrations obtained from simulated XRD fits.

However, it is important to understand that the fitting is performed by equating the lattice expansion measured by the XRD to the proportion of manganese in the gallium substitutional sites. This is done by assuming that lattice constant obeys Vegard's law and varies linearly with manganese concentration (Zhao *et al.*, 2005a), ranging from that of GaAs with no manganese to that of a hypothetical cubic MnAs, the lattice constant of which is taken as 0.589 nm (Kuryliszyn-Kudelska *et al.*, 2004). There are three points to note, then, concerning the accuracy of these fits. Firstly, the estimated manganese concentration is strongly influenced by the assumed lattice constant for cubic MnAs. Secondly, the fitting assumes that all the manganese were substitutional. Interstitial manganese, as well as arsenic anti-site defects, cause a greater lattice strain than substitutional manganese (Mašek *et al.*, 2003; Zhao *et al.*, 2005b). Therefore the fit is expected to give a higher estimate of the substitutional manganese concentration, with some amount of interstitials causing an overestimate. The final point is that it is assumed that the substitutional manganese are only in the nominal magnetic layers. Simulating the sample with a GaAs spacer layer assuming it is a bulk epilayer with a low uniform manganese concentration gives an equally good fit to the measured XRD data. The inhomogeneous nature of these samples therefore means that caution is required when using such XRD analysis.

6.4 SQUID

6.4.1 Experimental method

Magnetic properties of the superlattices were characterised by magnetisation measurements using a SQUID magnetometer. The superlattice samples were prepared into square 5 mm × 5 mm chips, keeping a careful note of the orientation of the substrate's [110] axis. The chips were mounted onto the sample holder, a length of Silver wire, using diluted GE varnish. Measurements were taken with the field along the principle in-plane axes, depending on how the sample was mounted. The same chip is used in all orientations.

The samples were cooled down to 2 K with a field strength of $\mu_0 H = 0.1$ T and then remanence was measured while the samples were warmed to 150 K. The samples were then cooled back down to 2 K with a field of $\mu_0 H = 1$ T. At 2 K $M(H)$ hysteresis loops would be made. All the measurements were made using the reciprocating sample option (RSO) mode.

% Al non-magnetic layer	T_C / K
0	32
20	26
30 (a)	23
30 (b)	25
40	20

Table 6.2: Curie temperature, T_C, of the superlattice samples obtained from remnant magnetisation measurements.

6.4.2 Results

The measured projections of the remnant magnetisation for the superlattice samples after cooling with a $\mu_0 H = 0.1$ T field are shown in Figure 6.5. The Curie temperature, T_C, extracted from the figures is shown in Table 6.2. The increased concentration of aluminium in the non-magnetic layer has the effect of suppressing T_C.

As a brief aside on the presentation of the SQUID magnetization data, in the interests of consistency SI units are used, rather than the centimetre-gram-second scheme commonly employed in this application. Conversion is simple: $1\ \mathrm{A\,m^{-1}} = 10^{-3}\ \mathrm{emu\,cm^{-3}}$. Due to the non-uniform vertical composition of the material, the volume for these purposes is not so well defined, so it is taken to be that of the magnetic layers only, assuming ideal growth conditions. For the 5×5 mm chip the volume of magnetic material in the 50 period superlattice is $2.83 \times 10^{-12}\ \mathrm{m^3}$.

In all the cases immediately below Curie temperature, T_C, the samples had a uniaxial magnetisation favouring the $[1\bar{1}0]$ axis, while at low temperatures they made a transition to a cubic anisotropy. The transition between uniaxial and cubic occurred at 50%-60% of T_C, but there was no apparent correlation between the aluminium concentration and the temperature at which that happened.

Plotted alongside the measured remnant magnetisation in Figure 6.5 is the calculated spontaneous magnetisation M_S, where

$$M_S^2 = M_{[110]}^2 + M_{[1\bar{1}0]}^2. \tag{6.1}$$

The excellent agreement between M_S and the measured [100] remnant magnetisation, $M_{[100]}$ for the 0% aluminium and second 30% aluminium non-magnetic layer superlattice samples suggests that in those two cases the samples are acting as single domains. For the other three samples there is an offset between M_S and

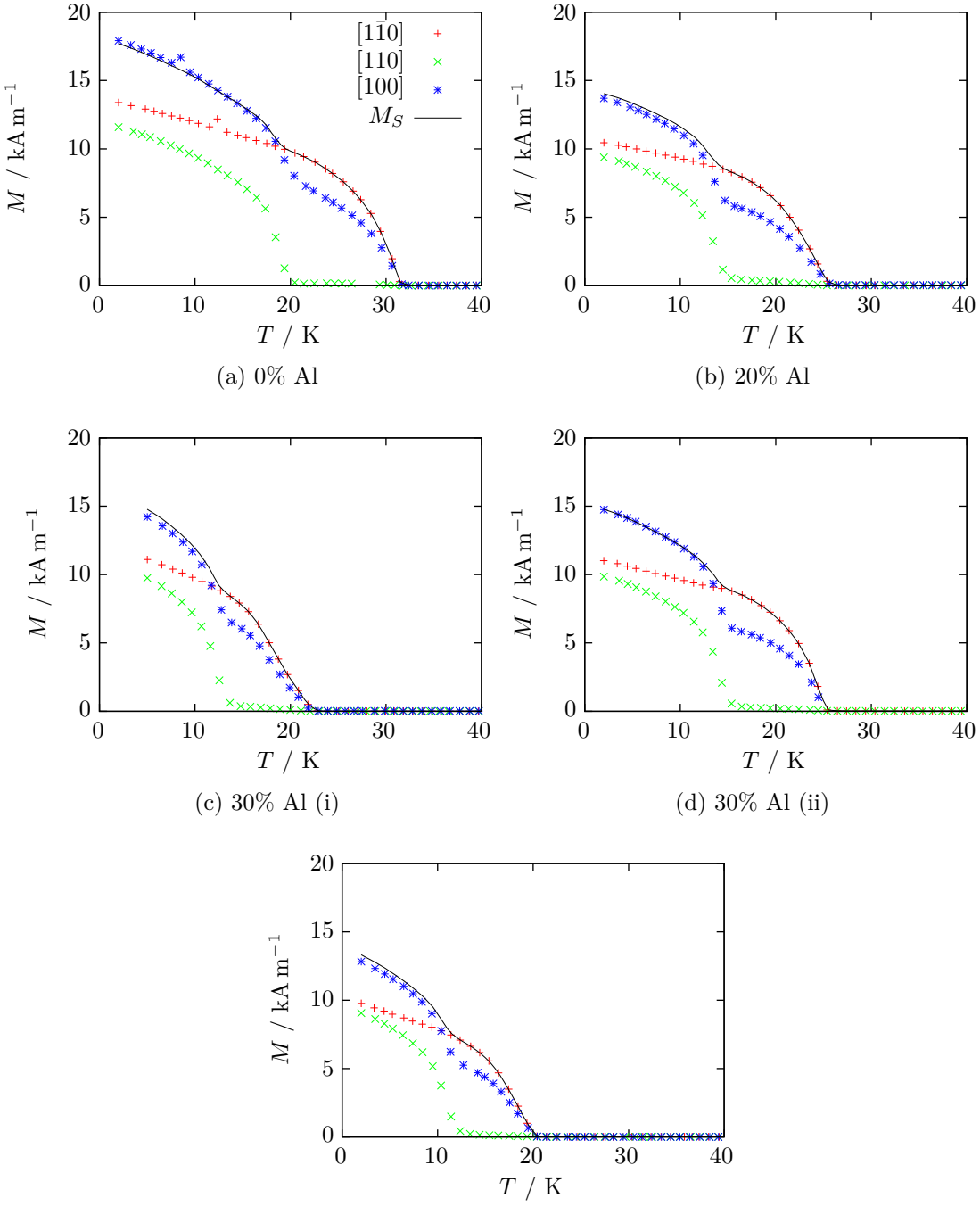

(a) 0% Al

(b) 20% Al

(c) 30% Al (i)

(d) 30% Al (ii)

(e) 40% Al

Figure 6.5: Temperature dependent remnant magnetisation along the principle crystalline axes for the superlattice samples.

$M_{[100]}$, which is probably the result of slight misalignments in the mounting. The single domain model is still likely applicable in these cases, but alternatively the offset could be due to M_S not being in-plane.

Using the experimentally determined moment contribution per manganese of 4.5 μ_B (Edmonds *et al.*, 2005) the effective manganese concentration can be determined from the magnetometry. For the sample with 0% aluminium in the non-magnetic layer, M_S at 2 K is 18 kA m^{-1}, which gives an effective concentration of 4.3×10^{20} cm^{-3}, equivalent to 1.9% doping. This value will be slightly lower than the actual manganese concentration due to the fact that interstitial manganese bond antiferromagnetically to substitutional manganese (Edmonds *et al.*, 2005), thus removing both moments. For comparison, the expected concentration from the growth is 2.25%, and the concentration estimated by XRD, taken from Table 6.1 is 2.7%. The expectation that the concentration calculated from the magnetometry data would be an underestimate while the XRD fits would provide an overestimate is consistent with the data and the concentration expected from the growth conditions is between these two bounds. It is therefore likely that the actual manganese concentration was close to that expected from the growth.

It is not readily feasible to estimate the proportion of interstitial manganese from this data because of the large uncertainties in the parameter values used to make the estimates. It is also likely that the concentration is not uniform but instead proportions could vary between different layer types and also there could be a gradient through the entire structure. However, the general trend between the superlattices is that as the proportion of aluminium in the non-magnetic layer increases the total moment decreases. This suggests that the addition of the aluminium is causing a greater proportion of manganese to become interstitial.

$M(H)$ loops, with the field applied along three different inplane axes, for the second 30% aluminium superlattice sample are shown in Figure 6.6. The background diamagnetic/paramagnetic response has been deducted. This is assumed to be proportional to the field, taking the constant to be the measured moment at 150 K when a field of 1 T was applied. A strong paramagnetic contribution in (Ga,Mn)As is associated with insulating samples (Oiwa *et al.*, 1997). However, very high fields must be applied in order to determine the paramagnetic component.

Following the analysis method used in Wang *et al.* (2005b), the anisotropy constants can be determined from the field at which the magnetisation is fully rotated in the direction in which the field is applied. This will occur when the $M(H)$

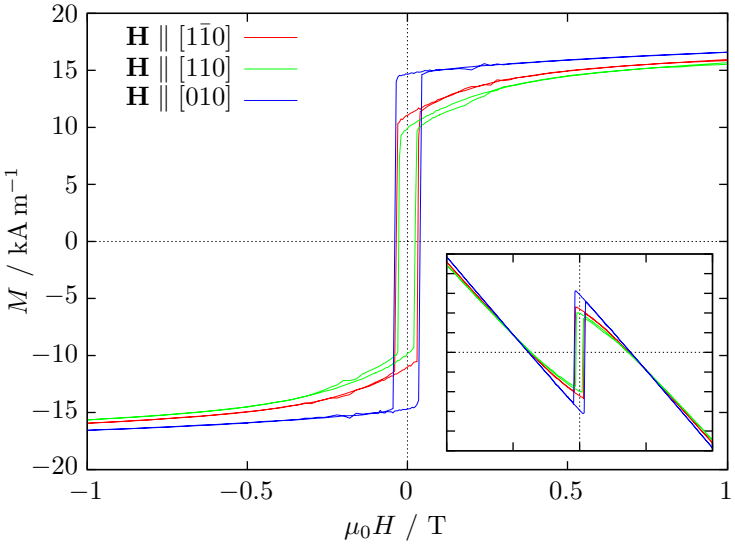

Figure 6.6: $M(H)$ loops for the second 30% aluminium superlattice sample with field applied along the three cardinal inplane axes. The background diamagnetic/paramagnetic response has been subtracted in the main panel; the inset shows the raw data. $T = 2$ K.

loops intersect outside the hysteretic region. The loops in Figure 6.6 do not intersect, making that method of analysis impossible. It does suggest, however, that even with a 1 T field the magnetisation is not fully rotated, indicating extremely strong anisotropies.

6.5 Transport

6.5.1 Experimental method

In order to measure magnetotransport properties, the initial superlattice sample Mn-279 was prepared, via optical lithography, into three Hall bars, based on the Philips mask, with the channels orientated along different crystalline axes. The channel orientations were [110], [100] and [1$\bar{1}$0], so each was 45° apart. As shown in Figure 6.7, the channel width was 50 µm and the centre-to-centre distance between the adjacent voltage probes was 310 µm, giving an aspect ratio of 6.2. Special care was taken not to heat the material during processing.

The samples were measured in a cryostat at $T = 4.2$ K using a MultiMag external magnet capable of rotating a field of up to 1 T in-plane. Standard four-point DC measurement techniques were used with a constant current of 1 µA. Both the longitudinal (diagonal), R_{xx}, and Hall (off-diagonal), R_{xy}, resistances were

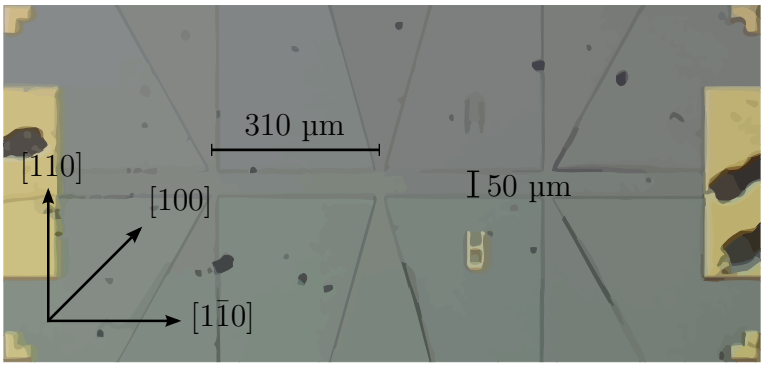

Figure 6.7: Optical image of the Hall bar aligned along the [1$\bar{1}$0] crystal axis. The width of the channel, d_w, and centre-to-centre distance adjacent voltage probes, d_l, are shown.

measured concurrently. Additionally, the [1$\bar{1}$0] Hall bar was measured with a 1 µA constant current on a probe capable of rotating the sample so the field could be applied out-of-plane using an external magnet system capable of fields up to 0.6 T.

6.5.2 Results

In Figure 6.8 the longitudinal resistance, $R_{xx}(T)$, is shown for each of the three devices as they are cooled down in the cryostat. The material started becoming insulating at low temperatures. With thick films, such as 25 nm, the 4.2 K resistance is not significantly greater than at room temperature (Potashnik *et al.*, 2001; Edmonds *et al.*, 2002b). This divergent behaviour is typical of ultra-thin 5 nm (Ga,Mn)As films (Giddings *et al.*, 2005). Although the overall vertical extent of the superlattice structure was over 150 nm, this behaviour could be understood by considering the superlattice as an array of parallel ultra-thin 2.26 nm films.

The differences in $R_{xx}(T)$ between the $\mathbf{I} \parallel [110]$ and $\mathbf{I} \parallel [1\bar{1}0]$ orientations shown in Figure 6.8 can be accounted for by the fact that the 4-point resistance of the $\mathbf{I} \parallel [1\bar{1}0]$ device at room temperature was slightly higher (less than 5%). This is likely due to slight variations in the fabricated structure; the variation in resistance between different combinations of voltage probes on a single sample is comparable. However, $R_{xx}(T)$ for the $\mathbf{I} \parallel [100]$ sample is significantly different, featuring a peak around $T = 10$ K, unlike for the other two orientations where the resistance continuously increases as the temperature is reduced. Such peaks are a typical feature in bulk (Ga,Mn)As epilayers, and approximately correspond to the

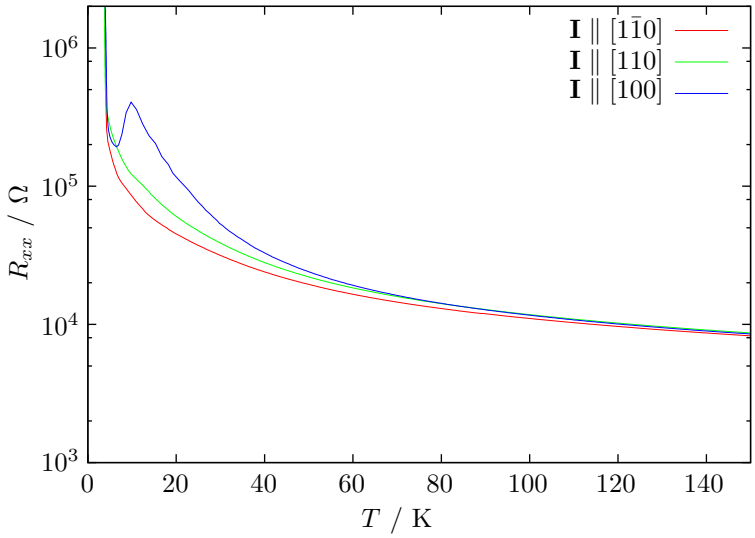

Figure 6.8: Longitudinal resistance, R_{xx}, as a function of temperature, T, as the three Hall bars are cooled down with an applied constant current of 1 µA. $\mu_0 H$ = 0 T.

Curie temperature, T_C (Edmonds *et al.*, 2002b). However, SQUID magnetometry measurements of this superlattice sample show T_C to be around 25 K, with some deviation over the surface of the wafer. Numerically differentiating the curves in Figure 6.8 does not reveal any inflection around the T_C as would be expected as the curves are monotonically decreasing. The resistance is diverging so rapidly that this overwhelms any other response.

The presence of this peak is, then, very hard to interpret, although it is possible that rapid cooling as Helium temperature is approached could cause an offset between the actual sample temperature and that of the temperature sensor, resulting in an apparently lower reading. However, the lack of significant change in resistance once the base temperature was reached suggests that this is not a significant factor. It should also be noted that no field was applied during cool-down, so the magnetisation state of the ferromagnetic layers is not well defined. Therefore this peak could be indicative of an unusual magnetisation arrangement within or between the layers.

By way of juxtaposition, the (Ga,Mn)As/InGaAs superlattice studied by Hernandez *et al.* (2001) showed a second peak in $R_{xx}(T)$ below T_C. Three suggestions were given for this second phase: antiferromagnetic alignment of adjacent magnetic layers, diffused manganese making the spacer layers magnetic but with a different transition or an unspecified effect related to carrier confinement in the non-magnetic layers. Given that there is no magnetometry data to support the

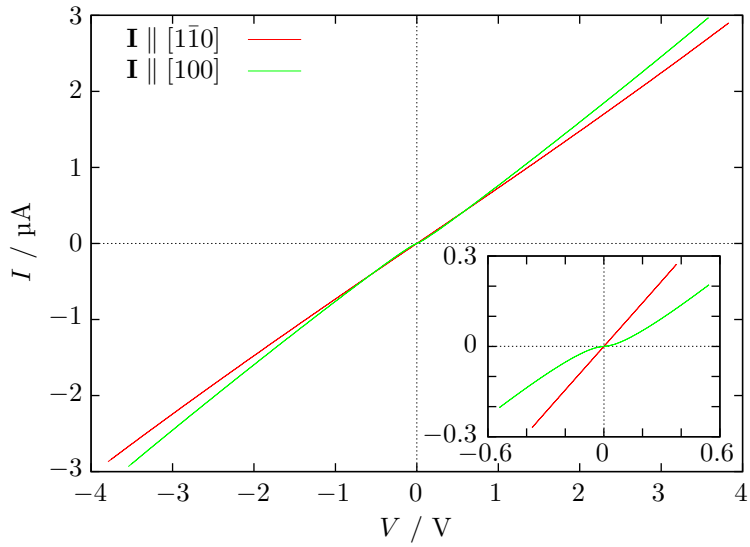

Figure 6.9: Current-voltage (I-V) characteristics for the **I** ∥ [1$\bar{1}$0] and **I** ∥[100] Hall bar samples fabricated from from the initial 30% aluminium superlattice. The inset shows initial measurements over a smaller range. $T = 4.2$ K, $\mu_0 H = 0$ T.

first explanation it is highly unlikely that AFM IEC is the cause. If this second phase were the result of exchange between the interstitial manganese diffused into the space layer this could have interesting ramifications for creation of an n-type DMS. This is a very striking feature and further measurement is required to verify it.

The I-V characteristics at $T = 4.2$ K are shown for the **I** ∥ [1$\bar{1}$0] and **I** ∥ [100] Hall bar samples in Figure 6.9. A linear fit of the **I** ∥ [1$\bar{1}$0] gives the "per square" resistance as 220 kΩ. Because of the presence of vertical barriers the electrical thickness of the superlattice is not well defined, so stating the conductivity is problematic. At one extreme, if the transport is assumed to be going through only a single layer, which has a thickness of 2.26 nm, then the conductivity at 4.2 K is 20 $\Omega^{-1}\,\mathrm{cm}^{-1}$. If, instead, transport is assumed to occur through all 50 layers and they can be considered as a single layer of 113 nm then, at the other extreme, the conductivity would be 0.40 $\Omega^{-1}\,\mathrm{cm}^{-1}$. In either case, the conductivity is very low in comparison with typical 2% (Ga,Mn)As epilayers, suggesting that fewer rather than more of the layers are involved in the transport.

The second anomaly of this material is shown by the inset of Figure 6.9. These I-V curves were taken prior to those shown in the main panel, and are over a smaller range. The striking difference is that over this range the **I** ∥[100] showed strong non-linear behaviour and had significantly higher resistance. After the increased

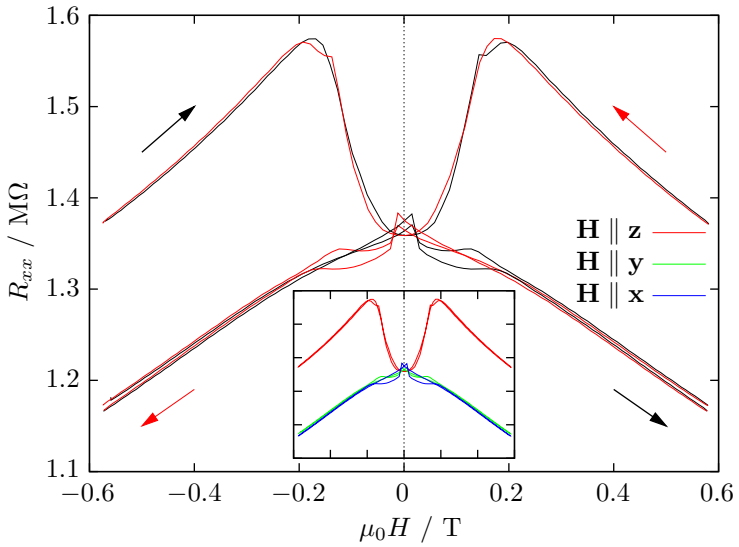

Figure 6.10: MR measurements of Hall bars fabricated from the initial 30% aluminium superlattice sample, with the field swept along the **z** axis perpendicular to plane, the **y** axis perpendicular to current in plane, and **x** parallel to current. $\mathbf{x} \parallel \mathbf{I} \parallel [1\bar{1}0]$. $T = 4.2$ K. In the main panel black represents increasing field and red is decreasing field. In the inset the sweeps for different orientations are differentiated by colour.

excitation used in the larger ranged I-V sweep shown in the main panel the characteristics had changed to show good Ohmic behaviour. A higher resistance state could be (partially) returned to by leaving the sample for a period of time, overnight for example, with no current running through it. This behaviour is explained as being the result of the higher excitation overcoming the vertical barriers, changing the vertical charge distribution and activating more layers through which transport could occur.

It is reasonable to ask why this was not shown in the I-V for the $\mathbf{I} \parallel [1\bar{1}0]$ sample in the inset. That, at least, is easy to explain. The room temperature resistance of the superlattice is very low, about 900 Ω per square, so a higher current was used initially for the first measurement. During the cool down of that sample $R_{xx}(T)$ was measured with a constant 10 µA current but because the sample became so resistive at low temperatures this exceed the compliance of the current source. Ergo, the high excitation activation had already occurred. The fact that the conductivity of the samples can be changed through the applied voltage was of course problematic to measurement. In the in-plane field sweeps, shown later, this was taken into account so that the applied current never exceeded 1 µA. The effect was clear: the resistance was about 50% higher.

The magnetoresistance for the $\mathbf{x} \parallel \mathbf{I} \parallel [1\bar{1}0]$ sample with the field applied in three

orthogonal orientations is shown in Figure 6.10. Unlike in the ultra-thin films with $\mathbf{I} \parallel [110]$ measured in Giddings *et al.* (2005), there was almost no AMR between the parallel to current, $\mathbf{I} \parallel \mathbf{x}$, and in-plane perpendicular to current, $\mathbf{I} \parallel \mathbf{y}$, field orientations. The size of the out-of-plane AMR is very large in comparison with typical bulk epilayer films, a property shared with the ultra-thin epilayers. For this sample it was over 15%.

In order to get a clearer understanding of the AMR, the resistivities of each sample were measured as the magnetic field was rotated in-plane. The data for a 1 T field rotated anticlockwise are shown in Figure 6.11. ϕ is the angle between current $\mathbf{I}$ and field $\mathbf{H}$. Measurements were also taken with a clockwise field sweep; only at fields weaker than 0.2 T is there any hysteresis in the in-plane field sweeps. The figures are plotted in terms of the fractional change in resistivity, $\frac{\Delta\rho_{xx}}{\bar{\rho}_{xx}}$ and $\frac{\Delta\rho_{xy}}{\bar{\rho}_{xx}}$ for longitudinal and lateral directions respectively. $\Delta\rho_{xx} = \rho_{xx} - \bar{\rho}_{xx}$ and $\Delta\rho_{xy} = \rho_{xy} - \bar{\rho}_{xy}$, where $\bar{\rho}$, the average resistivity, is defined as

$$\bar{\rho} = \frac{\sum_{i=0}^{n} \rho(\psi_i)}{n}, \tag{6.2}$$

for measurement points ψ_i evenly distributed around a circle. The average resistances $\bar{R}$ are defined similarly. From the definition of resistivity, $\rho = \frac{\mathcal{E}}{J}$, where current density $J = \frac{I}{d_d d_w}$ and $\mathcal{E}$ is the electric field. Longitudinally $\mathcal{E}_x = \frac{Vxx}{d_l}$, and so the usual resistivity relationship follows $\rho_{xx} = R_{xx}\frac{d_d d_w}{d_l}$. Note, however, that, while length, d_l, and width, d_w, are well defined from the Hall bar geometry shown in Figure 6.7, as previously discussed, the depth, d_d, is not well defined. The presence of the (Al,Ga)As barriers in the (001) plane means that the current density in the z-axis cannot be assumed to be uniform; depending on the size of the barriers the current may have significant vertical confinement. By inspection, $\frac{\Delta\rho_{xx}}{\bar{\rho}_{xx}} = \frac{R_{xx}}{\bar{R}_{xx}} - 1$. Transversely, $\mathcal{E}_y = \frac{Vxy}{d_w}$, and so $\rho_{xy} = R_{xy} d_d$. Therefore, $\frac{\Delta\rho_{xy}}{\bar{\rho}_{xx}} = \frac{R_{xy} - \bar{R}_{xy}}{\bar{R}_{xx}}\frac{d_l}{d_w}$. The aspect ratio of the channel is $\frac{d_l}{d_w}$. For ease of notation, $P_{xx} = \frac{\Delta\rho_{xx}}{\bar{\rho}_{xx}}$ and $P_{xy} = \frac{\Delta\rho_{xy}}{\bar{\rho}_{xx}}$.

The P_{xx} data shown when $\mu_0 H = 1$ T in Figure 6.11(a) have several features that can be identified. The most striking are the spikes in the resistivity, which occur when the field is applied along the $\langle 110 \rangle$ axes. The greater spike is associated with the $[1\bar{1}0]$ direction, and the lesser with the [110] direction. In addition to these spikes there is an underlying $\cos 2\phi$ behaviour. The lack of anisotropy between the $\mathbf{H} \parallel \mathbf{x}$ and $\mathbf{H} \parallel \mathbf{y}$ shown in Figure 6.10 can be understood as being due to the $\mathbf{I} \parallel [1\bar{1}0]$ orientation of that sample; the lesser spike is reinforced by the $\cos 2\phi$

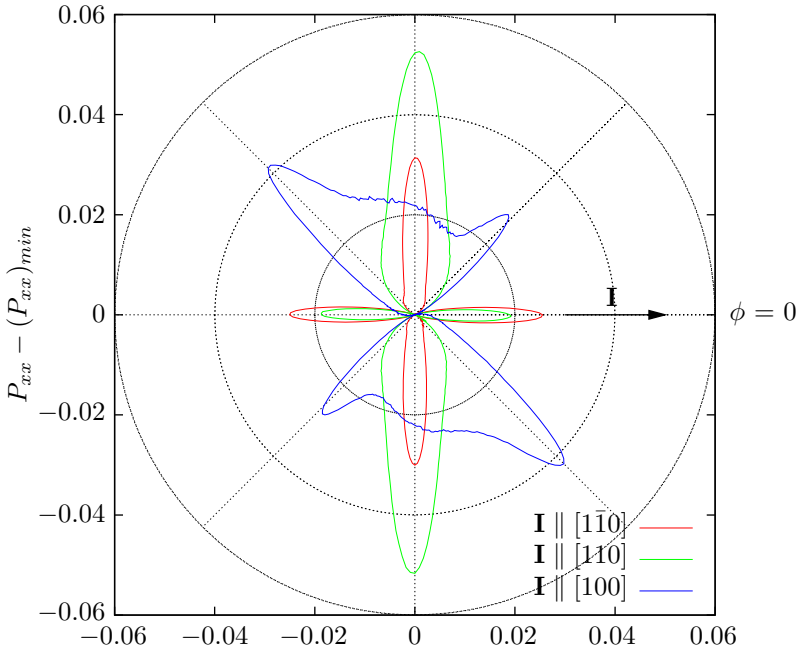

(a) Longitudinal

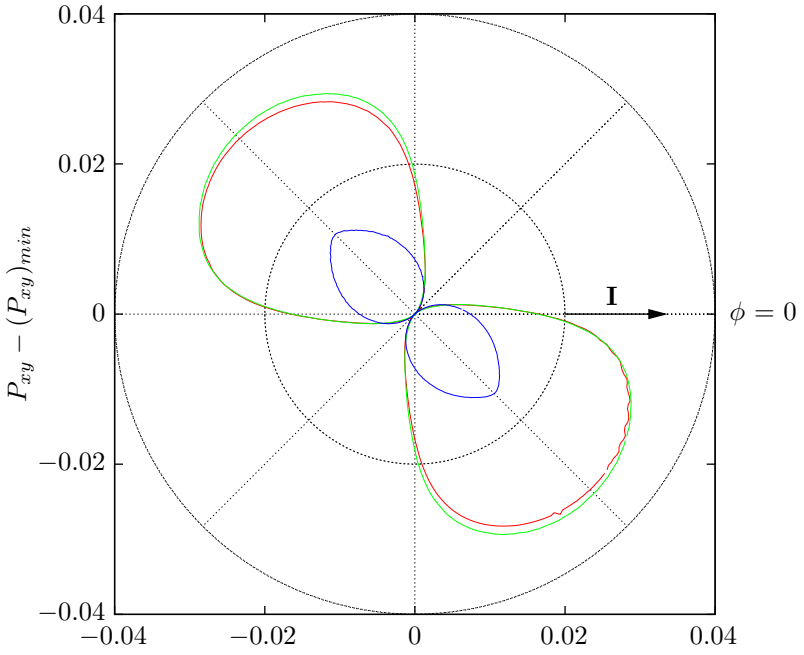

(b) Transverse

Figure 6.11: In plane AMR as a function of ϕ, the angle between **H** and **I**, for the (a) longitudinal and (b) transverse resistivities. The 1 T field is rotated anti-clockwise. The samples are Hall bars fabricated from the initial 30% aluminium superlattice sample. Note polarity of the transverse measurements is assumed. Fractional change in resistivity, P, is defined in the text.

and the greater one diminished, leading to an AMR of only 0.5% between these two directions. When instead $\mathbf{I} \parallel [110]$ the opposite case occurs and so the AMR between the $\mathbf{H} \parallel \mathbf{x}$ and $\mathbf{H} \parallel \mathbf{y}$ is about 3%.

The P_{xy} data in Figure 6.11 (b) shows a heavily distorted $\sin 2\phi$ character. When the channel is aligned along the uniaxial directions the sine function has a convex distortion while in the cubic direction the distortion is concave, resulting in something resembling a triangle wave. This is an observed property of the transverse AMR at low fields Tang *et al.* (2003), sometimes also known as the planar or pseudo Hall effect. However, the fact that there is still significant distortion from a sinusoidal function even when the applied field is as large as 1 T suggests that the anisotropy fields in this material are very large.

One possible interpretation of the spikes in P_{xx} is that they are due to the magnetisation, $\mathbf{M}$, coming out-of-plane. This could occur if [001] were an easier axis than the [110] or $[1\bar{1}0]$ and the applied field of 1 T was not sufficient to saturate the magnetisation along these directions. As shown in Figure 6.10, an out-of-plane magnetisation is a high resistance state, so when the magnetisation moves out-of-plane an increase in resistance is observed. If this is the case then the fact that the resistance increased the most when the field was applied in the $[1\bar{1}0]$ orientation identifies that axis as being the most magnetically hard. An out-of-plane easy axis can be associated with a low carrier concentration (Sawicki *et al.*, 2004) such as in an (Al,Ga,Mn)As alloy (Takamura *et al.*, 2002), through strain engineering a tensile strain (Liu *et al.*, 2003) and also in ultra-thin films (Rushforth *et al.*, 2007a). AlAs and GaAs have lattice constants that differ by less than 1% (Schulman and McGill, 1979), so the (Al,Ga)As non-magnetic spacer will not result in a significant strain, but the other factors may all play a role.

However, the data shown in Figure 6.5 suggest an in-plane single domain model works well. In that case, the magnetisation would not be expected to come out of plane. An alternative explanation could be that as the magnetisation does not rotate coherently through the $[110]/[1\bar{1}0]$ orientations but instead breaks into multiple domains. If this is the case, the domains could be forming inside each individual magnetic layer but also it is also possible that the discrete magnetic layers themselves remain single domain but are switching independently of each other. In either case, an increase in the longitudinal resistance would be expected.

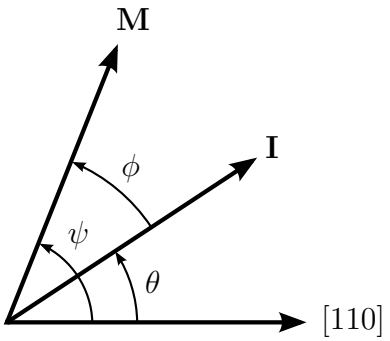

Figure 6.12: Schematic showing the angle definitions of angles θ, ψ and ϕ, assuming that the magnetisation tracks the applied field.

6.5.3 Analysis

Using the analysis method employed by Rushforth *et al.* (2007b), the longitudinal AMR can be written as

$$P_{xx} = \frac{\Delta\rho_{xx}}{\bar{\rho}_{xx}} = C_I \cos 2\phi + C_U \cos 2\psi + C_C \cos 4\psi + C_{I,C} \cos(4\psi - 2\phi), \quad (6.3)$$

and the transverse AMR as

$$P_{xy} = \frac{\Delta\rho_{xy}}{\bar{\rho}_{xx}} = C_I \sin 2\phi - C_{I,C} \sin(4\psi - 2\phi). \quad (6.4)$$

As illustrated in Figure 6.12, ϕ is the in-plane angle between the magnetisation, **M**, and the current, **I**, and ψ is the in-plane angle between **M** and the [110] crystal axis. This analysis assumes that the magnetisation tracks the applied field so that $\mathbf{H} \parallel \mathbf{M}$. The terms C_I, C_U, C_C and $C_{I,U}$ represent the AMR contributions from the non-crystalline, uniaxial crystalline, cubic crystalline and crossed non-crystalline/crystalline components.

As shown in Figure 6.12, $\phi = \psi - \theta$, where θ is the angle between **I** and the [110] crystal axis. From the fact that for the [110] orientated Hall bar, $\theta = 0$, for [100] $\theta = -\frac{\pi}{4}$ and for $[1\bar{1}0]$ $\theta = -\frac{\pi}{2}$ it can be written that

$$\phi_{\mathbf{I}\parallel[110]} = \psi, \quad (6.5)$$

$$\phi_{\mathbf{I}\parallel[100]} = \psi + \frac{\pi}{4}, \quad (6.6)$$

$$\phi_{\mathbf{I}\|[1\bar{1}0]} = \psi + \frac{\pi}{2}. \tag{6.7}$$

By substituting Equation 6.5 into Equations 6.3 and 6.4 the longitudinal and transverse AMR for the [110] orientated bar can be rewritten as

$$P_{xx}(\mathbf{I} \parallel [110]) = (C_I + C_U + C_{I,C}) \cos 2\psi + C_C \cos 4\psi, \tag{6.8}$$

and

$$P_{xy}(\mathbf{I} \parallel [110]) = (C_I - C_{I,C}) \sin 2\psi. \tag{6.9}$$

Similarly, by substituting in Equations 6.6 and 6.7 the following relationships are obtained

$$P_{xx}(\mathbf{I} \parallel [100]) = -(C_I + C_{I,C}) \sin 2\psi + C_U \cos 2\psi + C_C \cos 4\psi, \tag{6.10}$$

$$P_{xy}(\mathbf{I} \parallel [100]) = (C_I + C_{I,C}) \cos 2\psi, \tag{6.11}$$

$$P_{xx}(\mathbf{I} \parallel [1\bar{1}0]) = (C_U - C_I - C_{I,C}) \cos 2\psi + C_C \cos 4\psi, \tag{6.12}$$

$$P_{xy}(\mathbf{I} \parallel [1\bar{1}0]) = (C_{I,C} - C_I) \sin 2\psi. \tag{6.13}$$

It is therefore now possible to take combinations of the AMR data in order to extract the components. Specifically, taking the difference between Equation 6.8 and Equation 6.12 gives

$$P_{xx}(\mathbf{I} \parallel [110]) - P_{xx}(\mathbf{I} \parallel [1\bar{1}0]) = 2(C_I + C_{I,C}) \cos 2\psi. \tag{6.14}$$

Doing the same for Equation 6.9 and Equation 6.13 with the transverse components gives

$$P_{xy}(\mathbf{I} \parallel [110]) - P_{xy}(\mathbf{I} \parallel [1\bar{1}0]) = 2(C_I - C_{I,C}) \sin 2\psi, \tag{6.15}$$

and so C_I and $C_{I,C}$ can be determined. To find C_U and C_C, take the sum of

Equation 6.8 and Equation 6.12 to give

$$P_{xx}(\mathbf{I} \parallel [110]) + P_{xx}(\mathbf{I} \parallel [1\bar{1}0]) = 2C_U \cos 2\psi + 2C_C \cos 4\psi. \tag{6.16}$$

The result of the combinations from Equations 6.14, 6.15 and 6.16 are shown in Figure 6.13 (a) and (b). Although the curves in (a) are distorted from true sinusoidal behaviour, it does at least show the expected periodicity, and so it is possible to try and extract the coefficients C_I and $C_{I,C}$. By fitting Equations 6.14 and 6.15 the extracted components are $C_I = -0.0134$ and $C_{I,C} = 0.0101$, although these values are unlikely to be quantitatively accurate.

It is more difficult to interpret the combination shown in Figure 6.13 (b) as it is strongly dominated by the spikes. However, taking the maximum values of the spikes, the figure shows that the tall spike has caused an increase in resistivity of 3.6% and the short spike an increase of 2.2%. If the sharp increases in resistance are caused by **M** coming out-of-plane then, assuming that the resistivity increases proportionally to the component of magnetisation out-of-plane, up to a maximum of 17% when the magnetisation is perpendicular to the plane, this suggests that the magnetisation is coming out-of-plane by 12° when $\mathbf{H} \parallel [1\bar{1}0]$ and 7° when $\mathbf{H} \parallel [110]$. However, [111] is a cubic hard axis, so the magnetisation would not be expected to move though this orientation. It is therefore unlikely that the magnetisation coming out of plane is responsible for these features.

6.6 Conclusion

The superlattice samples, to the extent that can be measured by XRD, appear to show excellent structural properties. Particularly promising is the close agreement between the otherwise identical samples grown on the old and new MBE systems, indicating a good reproducibility in growth. However, the material offers many challenges to analysis, particularly in attempts to extract the anisotropy constants. This is due to the extremely strong anisotropies inherent in the material preventing it from reaching saturation with fields below 1 T.

From general trends in the magnetometry the superlattices appeared to behave much like typical bulk epilayers with a poor Curie temperature and a transition from uniaxial to cubic anisotropy at low temperatures. Despite the prediction otherwise, it is clear that the Curie temperature was not improved through the increased confinement of carriers in the magnetic layer due to the incorporation of

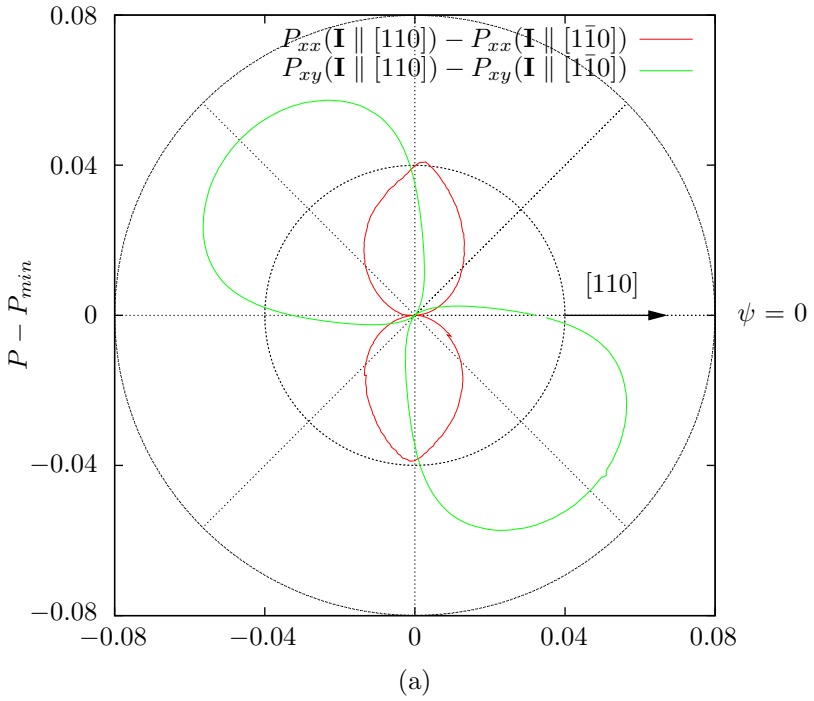

(a)

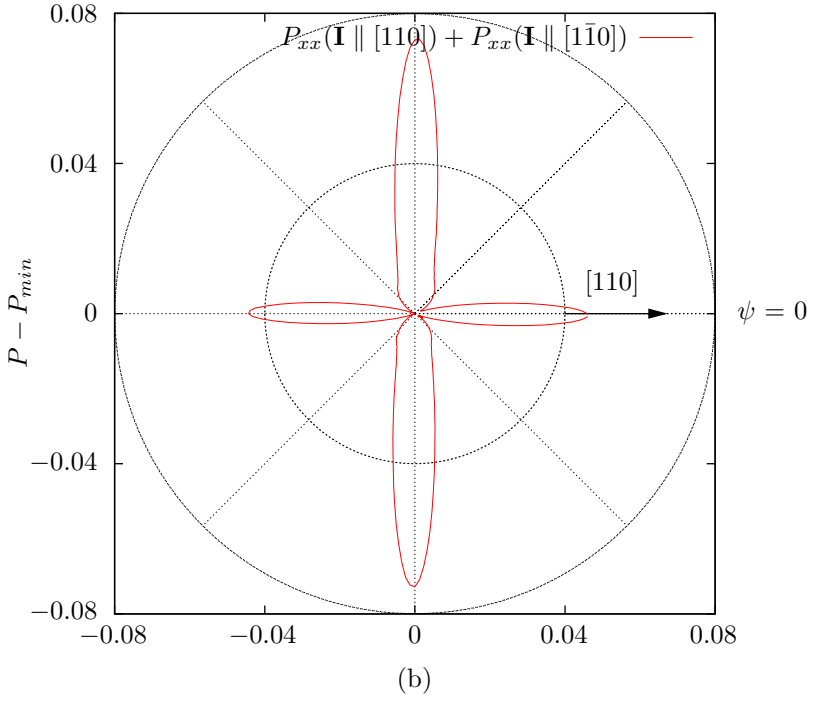

(b)

Figure 6.13: Combinations of the fractional changes in resistivities, P_{xx} and P_{xy} for different orientated Hall bars as a function of ψ, the angle between the magnetisation, **M**, and [110] axis.

aluminium in the non-magnetic layers. However, this deterioration may be caused by an increased occurrence of interstitial manganese. Taking magnetotransport data was particularly problematic due to insulating nature of the material at low temperatures. From the data gathered the indication is that the transport anisotropies are similar to that of a bulk epilayer.

One thing that is not clear is whether there is strong coupling between the layers, or whether they are acting independently, albeit with almost identical properties. If there were some diffusion of manganese into the supposed "non-magnetic" layers then this could result in a strong coupling between all the layers. However, due to the band offset, carriers are confined to the magnetic layers resulting in the high resistance.

It would be of interest to repeat these measurement with greater applied fields. A further avenue of exploration is the isolated embedded ultra-thin film which offers an interesting comparison and could indicate whether or not the magnetic layers can be intrinsically ferromagnetic or whether exchange between the layers is necessary.

Chapter 7

Conclusion

7.1 Summary

In this work DMS (Ga,Mn)As has been used as a basis for attempting to demonstrate novel MR effects which could be of interest in spintronic applications. Two device geometries were considered, lateral and vertical, highlighting the versatility of the magnetic semiconductor material.

Creating nanodevices offers significant challenges. In Chapter 2 the methodology for fabricating (Ga,Mn)As nanostructures was outlined, along with a discussion of the pertinent issues and considerations. Through the use of e-beam lithography it was possible to create nanoconstrictions with lateral sizes in the order of tens of nanometers. The choice of resist type offered very different approaches to making such structures, and thus the desired device geometry would determine the most appropriate methodology. Due to its excellent resolution and sensitivity, positive resist PMMA was found to be suitable for defining both small channels as well as larger areas. A detailed recipe was given for the nanoconstriction fabrication.

The properties of unstructured ultra-thin 5 nm (Ga,Mn)As were examined in the first part of Chapter 3. Unlike good quality thicker layers, the thin films were found to be insulating at low temperatures. They also showed significant anisotropies in the MR between the two perpendicular-to-current field orientations. Specifically, when the field was applied out of the plane of the epilayer the MR was particularly large in comparison to that found in bulk epilayers. These differences were attributed to strong vertical confinement breaking the symmetry between the perpendicular-to-current orientations.

Using a series of devices featuring Hall bars with pairs of nanoconstrictions of

differing widths it was found that as the lateral sizes became less than 100 nm transport characteristics started to alter. This change was associated with the formation of a tunnel junction across the nanoconstriction. In the 30 nm device the size of the hysteretic features became many times greater in size and also the orientation of the features reversed in sign. Depending on the orientation of the field both spin-valve and inverted spin-valve like characteristics could be observed. This precluded the possibility that the mechanism behind this effect was TMR, which can only show positive hysteretic features in (Ga,Mn)As. Therefore, the observed magnetoresistances were interpreted as TAMR. This had previously only been observed in vertical (Ga,Mn)As based devices and originated from the anisotropies in the tunnelling DOS. Because of the geometry of the nanoconstriction and the vertical confinement of the thin film, the number of k_y and k_z states from which tunnelling could occur was restricted. Therefore, changes in the magnetic field could significantly change the local DOS either side of the nanoconstriction and so dramatically change the tunnelling probabilities. As a consequence of this, TAMR was shown to be a generic property of ferromagnetic tunnel structures, and it was predicted that TAMR could be observed in ferromagnetic metal systems.

The nanoconstriction devices were revisited in Chapter 4 using a cleaner device structure and better measurement apparatus. By now being able to rotate the field with the sample *in situ* the close relationship between the AMR of the epilayer and the nanoconstriction was shown. It was also demonstrated that TMR-like spin-valve behaviour was possible with only a single tunnel barrier. However, because the magnetisation either side of the constriction should always be parallel then some other mechanism must be responsible. This highlighted the difficulty in analysing measurements of these tunnelling devices as there are many MR effects that could be competing. To further emphasise this point, when the magnetic field was aligned along one of the uniaxial directions a switching behaviour was observed, something reminiscent of early SET structures. Between these two states or between different thermal cycles the anisotropies could be very different, leading to extremely large observed MRs. This behaviour was interpreted as a manifestation of CBAMR. Because of inhomogeneities in the structure resulting from the fabrication, the chemical potential would change differently at different parts of the structure depending on the applied field. Due to the formation of islands in which charge can be trapped, something inferred from the telegraphic noise, the differential changes in the chemical potentials would result in differing transmission probabilities through the islands. This particularly highlights how

fabrication methods and device design can significantly affect observed phenomena.

In Chapter 5 a self-consistent simulation based on the Zener $\mathbf{k}\cdot\mathbf{p}$ kinetic-exchange model was used to examine IEC between magnetic layers in a (Ga,Mn)As/GaAs based superlattice. The sign of the IEC energy, E_c, would oscillate as a function of the non-magnetic spacer layer thickness and the carrier density, something predicted by RKKY theory. When E_c was positive the adjacent magnetic layers would have a parallel alignment, while a negative E_c would indicate an AFM arrangement. In the latter case the miniband bandwidth was much narrower than in the former, hence the resistance could be much greater. The multidimensional parameter space offered by these systems was explored in order to find arrangements optimal for the exhibition of AFM interlayer coupling. It was found that in systems with thin magnetic layers and a large concentration of unpolarised carriers in the non-magnetic layers the oscillatory behaviour was similar to that of RKKY. However, if the non-magnetic layers were depleted, either through self-consistent charge redistribution caused by magnetic order or because of the introduction of a band offset between the magnetic and non-magnetic layers, the oscillatory pattern became far more complex, and additionally became less dependent on non-magnetic layer thickness. This therefore suggested structural parameters that might be suitable for realising a new MR effect in these superlattice systems.

Due to the close lattice match between (Al,Ga)As and GaAs for all aluminium concentrations, superlattice structures can be made with different electric properties by altering the band offsets without compromising the structural properties. This very useful property was used in Chapter 6 where (Ga,Mn)As based superlattices with different aluminium concentrations, based on the calculated parameters of Chapter 5, were measured using low temperature transport and magnetometry techniques. In addition to AFM interlayer coupling, other properties of short period magnetic superlattices, such as high Curie temperatures, had been predicted to arise as a consequence of the enhanced confinement of carriers to the magnetic layers. While XRD showed the superlattices to have excellent structural properties, it appeared that increasing the aluminium concentration had a detrimental effect on the magnetic properties, probably due to an increased partial concentration of interstitial manganese. The superlattice also showed somewhat unusual anisotropic magnetotransport properties. However, analysis of these proved difficult due to the anisotropy field being larger than the available measurement fields. These strong anisotropies may be another

consequence of the strong vertical confinement.

In the next section, all these ideas about fabrication, lateral tunnelling devices and vertical heterostructures will be brought together with the proposal of future experimental devices.

7.2 Future work

There is clearly a vast scope for future DMS devices and the rich physical playground that such systems offer will no doubt lead to the discovery of further novel effects, exhibited as an MR or otherwise. As improvements are made in the control of growth and fabrication of the material, it is strongly hoped that the further study of (Ga,Mn)As nanostructures will improve the understanding of the origin of these effects, both in DMSs and also for wider spintronic functionalities.

The ability to accurately define and create the lateral nanoconstrictions is the key to achieving further progress in that type of device. Indeed, if such work was to be taken forward, emphasis would have to be placed on improving fabrication techniques to ensure that processing is not inadvertently introducing defects that cause a significant contribution to anisotropies and MR effects. Naturally, any future devices would ideally have gates in order to allow fine tuning of the electrostatic conditions around the constriction. This could be potentially be achieved by using a back gate created from from a conductive layer defined via MBE. This approach would have the advantage that the gate can be very close to the device without placing significant additional burden on the already problematic lithographic processes. An example of a future basis for a device is spin blockade, which is an effect that promises large MRs (Zhuravlev *et al.*, 2003) and this lateral geometry would be well suited for exploring this prospect.

Unless growth techniques can improve the quality of the ultra-thin epilayers, these would not be recommended for use in future work due to their inherent problems. Using better characterised and well-behaved thicker layers would help differentiate the interplay between intrinsic effects of the thin films such as spacial inhomogeneity, strong atypical anisotropies, divergent resistance characteristics and non-linear hopping transport and the extrinsic effects produced by the nanoconstriction.

Turning now to the superlattice based devices, the obvious point for future work is that as yet AFM IEC has still not been observed. Additionally, it would be highly

desirable to re-examine the material used in this work with the ability to apply higher fields. There is the indication from the transport measurements that these heterostructures possess some unusual properties. These need to be confirmed, and the origins explored. However, the difficulty in creating (Ga,Mn)As based structures, in comparison to normal non-magnetic semiconductor heterostructures, means there is some uncertainty about the material's structural characteristics, which makes interpretation problematic. Perhaps future attempts on this kind of structure should start with larger period structures where interface effects are less likely to dominate. It is notable that there has been in the past several attempts by other groups to create (Ga,Mn)As based superlattices and they have seen similar results.

The purpose of the rest of this section is to give a detailed outline of a proposal for a novel class of (Ga,Mn)As device based on n-type material. These ideas have been developed in collaboration with Oleg Makarovsky.

In typical semiconductor technology, such as the complementary metal oxide semiconductor (CMOS) transistor, both n- and p-channels are used by devices in complementary roles (Campbell, 2001). Dilute magnetic semiconductors, such as (Ga,Mn)As, offer the potential to move beyond conventional CMOS designs by offering a rich variety of physical phenomena other than the field effect employed in CMOS transistors. However, (Ga,Mn)As is a p-type material; the itinerant carriers that mediate the magnetic exchange are holes, thus necessitating that any devices based on this material have only a p-channel. Although a true spintronic device would utilise spin-valve effects to control switching based on spin-state rather than charge state, the lack of an n-type complementary material prevents the utilisation of techniques employed in traditional semiconductor devices such as the field effect or bipolar transistor and light emitting or laser diodes. Therefore, the development of an n-type material to complement the p-type (Ga,Mn)As could open many interesting avenues of exploration. It is therefore of little surprise that the possibility of making an n-type DMSs exhibiting similar properties to (Ga,Mn)As has been being considered recently (Mašek *et al.*, 2007a).

The usual picture of ferromagnetism in (Ga,Mn)As has exchange mediated by p-d orbital hybridisation of valence band states. As a result, it is generally believed that conduction band s-states cannot mediate the ferromagnetism. However, calculations by Mašek *et al.* (2007b) show that hybridisation of d-states is sufficient for ferromagnetic coupling by either holes or electrons. In the case of the conduction band, it is possible only when there is sufficiently strong doping. Based

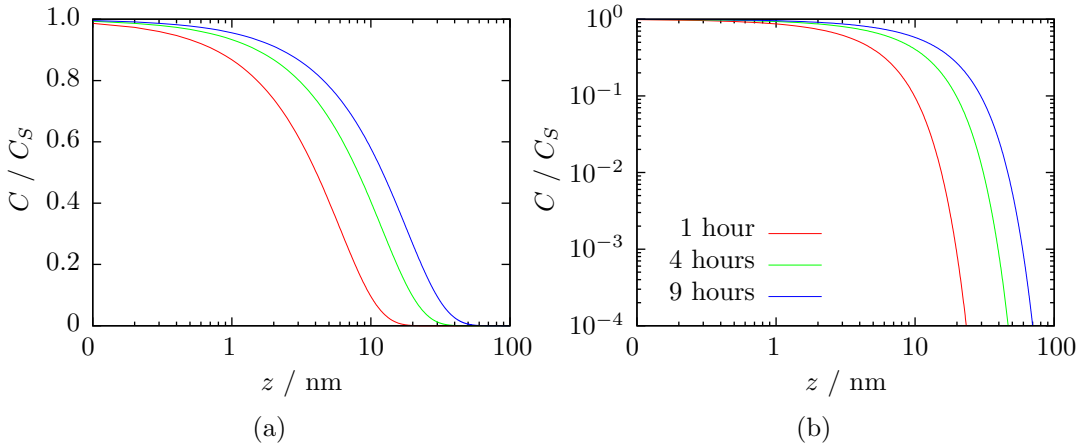

Figure 7.1: The ratio of impurity concentration, C, to surface concentration, C_S, as a function of depth, z after annealing for 1, 4 and 9 hours. The temperature is 180°C. The data in both figures are identical but plotted on different scales to show the expected concentrations (a) close to the interface and (b) deep into the substrate.

on this evidence it appears that an n-type DMS is feasible.

The site in which a manganese dopant is placed in the GaAs lattice has profound effects on its properties. In a gallium substitutional position the manganese acts as an acceptor, while interstitial manganese is a double donor (Wang *et al.*, 2004). Typically, because of the negative effects they have on the magnetic properties, the interstitials are unwanted in (Ga,Mn)As. Fortunately, because of their high mobility they may be removed through low temperature annealing. The removal occurs as a two step process. Firstly, the interstitial manganese diffuse to the surface and secondly they are electrically passivated by oxidation (Edmonds *et al.*, 2004).

Utilising this process in reverse, the intention is to create GaAs with a high concentration of interstitial manganese. This is to be achieved by diffusing the interstitials from a layer containing a high concentration into an adjacent GaAs layer or substrate.

A one-dimensional diffusion profile for the interstitial manganese can be calculated using the error function complement (Jakiela *et al.*, 2006; Sze, 1981, p. 67)

$$C(z,t) = C_S \operatorname{erfc}\left(\frac{z}{2\sqrt{Dt}}\right), \tag{7.1}$$

where C is the impurity concentration at depth z and time t. C_S is the surface

concentration and D is the diffusion coefficient. The value of D used for the interstitial manganese in GaAs at 180°C is 5×10^{-21} $\mathrm{m^2\,s^{-1}}$, estimated from measured annealing experiments (Edmonds *et al.*, 2004). Although this model does not include the electrostatic barrier that will arise between the oppositely charged interstitial and substitutional manganese, the calculated diffusion profile shown in Figures 7.1(a) and (b) suggests that there is likely to be a very high concentration of interstitials to a depth of several nanometres formed during the annealing process.

In the model in Equation 7.1 the surface concentration C_S is assumed to be constant, and thus an infinite source. In actuality, when the (Ga,Mn)As is annealed in air the interstitials are passivated and as a result the concentration will be reduced until effectively they are all removed. Therefore, in order to prevent, or at least retard this process the manganese that come to the surface must be prevented from being oxidised. Two methods are proposed to achieve this. The first is to anneal in an ultra-high vacuum, which has been shown to be inefficient in comparison to air or a nitrogen atmosphere, suggesting that under the right conditions the passivation could be a rate-limiting process (Adell *et al.*, 2005). Although this can be performed in a vacuum oven, annealing *in situ* in the MBE machine post-growth would be ideal, although of course practicalities may not allow this option. However, it is worth noting that during a long growth some amount of annealing will have already taken place deeper in the epilayer. Therefore, depending on the details of the growth, there will already be some concentration of interstitials in the GaAs substrate in the as-grown material. The second method is simply to put an unreactive metal layer, such as gold, on the top of the material prior to annealing. This would not only remove the surface for oxygen (or else) to reach and passivate the interstitials, but the metal layer could be utilised as part of a device structure, for example, for bond pads or an etch mask.

Appropriate choice of material to form the p-type layer can assist greatly in the formation of the n-type layer. Specifically, it is desirable that there is a high concentration of interstitial manganese in the host layer. This can be achieved simply by having a high doping concentration for the (Ga,Mn)As layer which will increase both the number of substitutional and interstitial manganese. However, *ab-initio* calculations have shown that in (Al,Ga)As the manganese doping has a greater partial concentration of interstitials for increasing aluminium concentration (Mašek *et al.*, 2007c). Therefore, a highly doped (Al,Ga)As host layer would seem ideal for initial experimentation.

As will have been noted from Figure 7.1, the depth that the interstitial reservoir is expected to extend is only a few nanometres, and as such in order to remove the host layer and utilise the n-type layer the etch will have to be extremely accurate. This introduces a second benefit of using (Al,Ga,Mn)As as the host layer, namely that for high aluminium concentrations it can be selectively etched easily (Hjort, 1996). Assuming that the presence of manganese does not significantly affect the etching process, for concentrations of aluminium greater than 50% an HF:H_2O etchant offers high etch rates and a selectivity greater than 10^7 (Yablonovitch *et al.*, 1987), which, for all intents and purposes, can be considered total selectivity. As an alternative, HCl also offers an excellent selectivity between (Al,Ga)As and GaAs for high aluminium concentration (Guan *et al.*, 2006).

There are some potential hurdles with attempting to create an n-type GaAs layer in this manner. For the selective etches it is not known what the impact would be of a high manganese concentration in the sacrificial layer. The efficacy of the selective etches is highly dependent on both the ratio of aluminium to gallium and also the etch solution (Kim *et al.*, 1998). Introducing manganese into the alloy could adversely effect the etch mechanism. If a non-selective etch is being used then achieving precisely the desired etch depth may prove a technical challenge. Insufficient etching would leave an unwanted p-type layer whilst too much etching would remove the material with the highest concentration of interstitial manganese. Another key problem is ensuring that the surface formed after etching is even and free of damage, something that will be dependent on the details of the etch. It is important that the top layer, which would be the most n-type, is of good quality.

Having outlined a methodology to introduce interstitial manganese into a GaAs layer, it is now interesting to consider the experiments that can be performed. An obvious thing that could be tried is to simply remove the p-type layer, and examine what remains. If the layer has sufficient carriers to be conductive the carrier type can be determined via AC-rectification. Ideally, it may even exhibit ferromagnetic properties similar to (Ga,Mn)As. However, a large concentration of interstitials would be required for the material to be conductive enough to enable effective contacts to be made to it and it is likely an even higher concentration would be required for ferromagnetism.

A more interesting idea is to etch away only part of the p-type layer so that a channel is formed, as illustrated in Figure 7.2. This scheme takes advantage a gold layer placed to limit manganese passivation, using it as both an etch mask

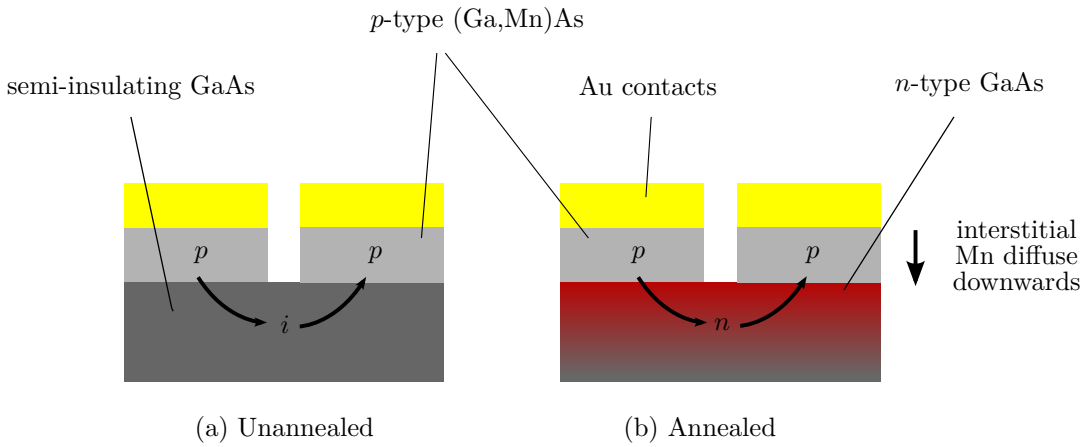

(a) Unannealed (b) Annealed

Figure 7.2: Schematic for the creation of *p*-*n*-*p* junction using the hypothetical manganese doped *n*-type GaAs.

and for contacts. If there are interstitials in the substrate then a *p*-*n*-*p* junction will exist; if not, or in an unannealed material, the junction will be *p*-*i*-*p*. The existence of the *n*-type GaAs could then be inferred from differences in the *I*-*V* characteristics of the two structures. While this is highly speculative, it is clear that such a structure could offer the basis for a variety of devices such as field-effect/bipolar spin-transistors or spin-LEDs, making it of significant interest and an exciting future project.

Appendix A

List of acronyms

AC alternating current

AFM antiferromagnetic

AMR anisotropic magnetoresistance

CBAMR Coulomb blockade anisotropic magnetoresistance

CMOS complementary metal oxide semiconductor

DC direct current

DMS dilute magnetic semiconductor

DOF depth of focus

DOS density of states

FM ferromagnetic

GMR giant magnetoresistance

HMDS Hexamethyldisilazane

HSQ hydrogen silsequioxane

IEC interlayer exchange coupling

IPA isopropyl alcohol

LSDA local-spin density approximation

MBE molecular beam epitaxy

MCD magnetic circular dichroism

MIBK methyl isobutyl ketone

MR magnetoresistance

NA numerical aperture

NAMR normal AMR

PMMA poly(methyl methacrylate)

QD quantum dot

RKKY Ruderman-Kittel-Kasuya-Yosida

RIE reactive ion etch

RSO reciprocating sample option

SEM scanning electron microscope

SET single electron transistor

SIMS secondary ion mass spectroscopy

SO spin-orbit

SOC spin-orbit coupling

SQUID superconducting quantum interference device

TAMR tunnelling anisotropic magnetoresistance

TMR tunnelling magnetoresistance

XRD X-ray diffraction

Appendix B

List of symbols

Notation

$\mathbf{k}$	Wavevector
k	Wavenumber
$\bar{k}$	Average wavenumber

Symbols

% AMR_{ip}	Percentage in-plane NAMR
% AMR_{op}	Percentage out-of-plane NAMR
% MR	Percentage MR
a_0	GaAs unit cell length
B	Magnetic field
C	Impurity concentration
c	Speed of light in free space
C_C	Cubic crystalline term
C_I	Non-crystalline term
C_S	Surface concentration
C_U	Uniaxial crystalline term
$C_{I,U}$	Crossed non-crystalline/crystalline term
D	Diffusion coefficient
d	Separation of adjacent magnetic layers
d_d	Electrical depth of stripe
d_l	Electrical length of stripe

d_m	Width of magnetic layer
d_n	Width of non-magnetic layer
d_w	Electrical width of stripe
d_{n+m}	Superlattice period
$\mathcal{E}$	Electric field
E	Energy
e	Elementary charge
E_c	IEC energy
g^*	Free-carrier g-factor
$\hbar$	The Planck constant
$\mathcal{H}$	Hamiltonian
H	Magnetic field strength
h_{pd}	Mean-field kinetic-exchange interaction
I	Current
J	Current density
J_{pd}	p-d coupling constant
k_F	Fermi wavenumber
L	Angular momentum
M	Magnetisation
m^*	Hole mass
m_e	Electron mass
M_S	Spontaneous remnant magnetisation
N_{2D}	2 dimensional carrier concentration
N_{3D}	3 dimensional carrier concentration
p	Momentum
R	Resistance
r	Orbital radius
R_{max}	Maximum resistance
R_{min}	Minimum resistance
R_{sheet}	Sheet resistance
S	Spin
T	Temperature
t	Time
T_C	Curie temperature
V	Potential
V_b	Band-offset
V_G	Hartree potential

V_{2pt}	Two-point voltage
V_{xc}	Exchange-correlation potential
x	Axis parallel to current
y	Axis in-plane perpendicular to current
z	Axis perpendicular to plane
α	Arbitrary scaling factor
ϵ_0	Electric constant
μ	Magnetic moment
μ_0	Magnetic constant
ρ	Resistivity
P	Fractional change in resistivity
Ψ	Wavefunction

Angles

θ	In-plane angle between [110] and **I**
ϕ	In-plane angle between **I** and **M**
ψ	In-plane angle between [110] and **M**
ω	X-ray incident angle
ω'	X-ray scattering angle

Subscripts

[100]	Component parallel to [100] orientation
[110]	Component parallel to [110] orientation
$[1\bar{1}0]$	Component parallel to $[1\bar{1}0]$ orientation
n	Subband index
x	Component parallel to **x**
xx	Longitudinal (diagonal) measurement
xy	Hall (off-diagonal) measurement
y	Component parallel to **y**
z	Component parallel to **z**
σ	Spin index

Bibliography

Abolfath, M., T. Jungwirth, J. Brum, and A. H. MacDonald, "Theory of magnetic anisotropy in $III_{1-x}Mn_xV$ ferromagnets", *Phys. Rev. B* **63**, 054418 (2001).

Adachi, Sadao, "GaAs, AlAs, and $Al_xGa_{1-x}As$ material parameters for use in research and device applications", *J. Appl. Phys.* **58**, R1–R29 (1985).

Adachi, Sadao, editor, *Properties of Aluminium Gallium Arsenide* (London: INSPEC, 1993).

Adell, M., J. Kanski, L. Ilver, J. Sadowski, V. Stanciu, and P. Svedlindh, "Comment on "Mn interstitial diffusion in (Ga,Mn)As"", *Phys. Rev. Lett.* **94**, 139701 (2005).

Allwood, D. A., G. Xiong, C. C. Faulkner, D. Atkinson, D. Petit, and R. P. Cowburn, "Magnetic domain-wall logic", *Science* **309**, 1688–1692 (2005).

Baek, In-Bok, Jong-Heon Yang, Won-Ju Cho, Chang-Geun Ahn, Kiju Im, and Seongjae Lee, "Electron beam lithography patterning of sub-10 nm line using hydrogen silsesquioxane for nanoscale device applications", *J. Vac. Sci. Technol. B* **23**, 3120–3123 (2005).

Baibich, M. N., J. M. Broto, A. Fert, F. Nguyen Van Dau, F. Petroff, P. Eitenne, G. Creuzet, A. Friederich, and J. Chazelas, "Giant magnetoresistance of (001)Fe/(001)Cr magnetic superlattices", *Phys. Rev. Lett.* **61**, 2472 (1988).

Batey, J. and S. L. Wright, "Energy band alignment in GaAs:(Al,Ga)As heterostructures: The dependence on alloy composition", *J. Appl. Phys.* **59**, 200–209 (1986).

Baxter, David V., Dmitry Ruzmetov, Julia Scherschligt, Y. Sasaki, X. Liu, J. K. Furdyna, and C. H. Mielke, "Anisotropic magnetoresistance in $Ga_{1-x}Mn_xAs$", *Phys. Rev. B* **65**, 212407 (2002).

Binasch, G., P. Grünberg, F. Saurenbach, and W. Zinn, "Enhanced magnetoresistance in layered magnetic structures with antiferromagnetic interlayer exchange", *Phys. Rev. B* **39**, 4828 (1989).

Bolotin, Kirill I., Ferdinand Kuemmeth, and D. C. Ralph, "Anisotropic magnetoresistance and anisotropic tunneling magnetoresistance due to quantum interference in ferromagnetic metal break junctions", *Phys. Rev. Lett.* **97**, 127202 (2006).

Bruno, P., "Theory of interlayer magnetic coupling", *Phys. Rev. B* **52**, 411 (1995).

Buhlmann, S., P. Muralt, P.-A. Kuenzi, and U. Staufer, "Electron beam lithography with negative calixarene resists on dense materials: Taking advantage of proximity effects to increase pattern density", *J. Vac. Sci. Technol. B* **23**, 1895–1900 (2005).

Campbell, I. A., A. Fert, and O. Jaoul, "The spontaneous resistivity anisotropy in Ni-based alloys", *J. Phys. C* **3**, S95–S101 (1970).

Campbell, Stephen A., *The Science and Engineering of Microelectronic Fabrication*, 2nd edition (New York: Oxford University Press, 2001).

Campion, R. P., K. W. Edmonds, L. X. Zhao, K. Y. Wang, C. T. Foxon, B. L. Gallagher, and C. R. Staddon, "High-quality GaMnAs films grown with arsenic dimers", *J. Cryst. Growth* **247**, 42–48 (2003).

Chen, Z. W., G. A. C. Jones, and H. Ahmed, "Nanowriter: A new high-voltage electron beam lithography system for nanometer-scale fabrication", *J. Vac. Sci. Technol. B* **6**, 2009–2013 (1988).

Chiba, D., N. Akiba, F. Matsukura, Y. Ohno, and H. Ohno, "Magnetoresistance effect and interlayer coupling of (Ga,Mn)As trilayer structures", *Appl. Phys. Lett.* **77**, 1873–1875 (2000).

Chiba, D., Y. Sato, T. Kita, F. Matsukura, and H. Ohno, "Current-driven magnetization reversal in a ferromagnetic semiconductor (Ga,Mn)As/GaAs/(Ga,Mn)As tunnel junction", *Phys. Rev. Lett.* **93**, 216602 (2004).

Chiba, D., K. Takamura, F. Matsukura, and H. Ohno, "Effect of low-temperature annealing on (Ga,Mn)As trilayer structures", *Appl. Phys. Lett.* **82**, 3020–3022 (2003a).

Chiba, D., M. Yamanouchi, F. Matsukura, T. Dietl, and H. Ohno, "Domain-wall resistance in ferromagnetic (Ga,Mn)As", *Phys. Rev. Lett.* **96**, 096602–4 (2006).

Chiba, D., M. Yamanouchi, F. Matsukura, and H. Ohno, "Electrical manipulation of magnetization reversal in a ferromagnetic semiconductor", *Science* **301**, 943–945 (2003b).

Chun, S. H., S. J. Potashnik, K. C. Ku, P. Schiffer, and N. Samarth, "Spin-polarized tunneling in hybrid metal-semiconductor magnetic tunnel junctions", *Phys. Rev. B* **66**, 100408 (2002).

Chung, S. J., S. Lee, I. W. Park, X. Liu, and J. K. Furdyna, "Possible indication of interlayer exchange coupling in GaMnAs/GaAs ferromagnetic semiconductor superlattices", *J. Appl. Phys.* **95**, 7402–7404 (2004).

Ciorga, M., A. Einwanger, J. Sadowski, W. Wegscheider, and D. Weiss, "Tunneling anisotropic magnetoresistance effect in a p^+-(Ga,Mn)As/n^+-GaAs Esaki diode", *Phys. Status Solidi A* **204**, 186–190 (2007a).

Ciorga, M., M. Schlapps, A. Einwanger, S. Geißler, J. Sadowski, W. Wegscheider, and D. Weiss, "TAMR effect in (Ga,Mn)As-based tunnel structures", *New J. Phys.* **9**, 351 (2007b).

Cui, Zheng, *Micro-Nanofabrication: Technologies and Applications*, 1st edition (Beijing: Higher Education Press, 2005).

Cullity, B. D., *Introduction to Magnetic Materials* (Reading, MA: Addison-Wesley, 1972).

da Cunha Lima, I. C., "Spin-polarized transport in low-dimensional systems", *Microelectron. J.* **34**, 475–480 (2003).

Davies, Paul C. W. and David S. Betts, *Quantum Mechanics*, 2nd edition (Cheltenham, UK: Stanley Thornes, 1999).

De Teresa, Jose Maria, Agnès Barthélémy, Albert Fert, Jean Pierre Contour, François Montaigne, and Pierre Seneor, "Role of metal-oxide interface in determining the spin polarization of magnetic tunnel junctions", *Science* **286**, 507–509 (1999).

DeSimone, D., C. E. C. Wood, and C. A. Evans Jr., "Manganese incorporation behavior in molecular beam epitaxial gallium arsenide", *J. Appl. Phys.* **53**, 4938–4942 (1982).

Devoret, Michel H. and Robert J. Schoelkopf, "Amplifying quantum signals with the single-electron transistor", *Nature* **406**, 1039–1046 (2000).

Dietl, T., "III-V and II-VI Mn-based ferromagnetic semiconductors", in *Advances in Solid State Physics*, edited by B. Kramer, 413–426 (Berlin: Springer, 2003).

Dietl, T., A. Haury, and Y. Merle d'Aubigné, "Free carrier-induced ferromagnetism in structures of diluted magnetic semiconductors", *Phys. Rev. B* **55**, R3347 (1997).

Dietl, T., Jürgen König, and A. H. MacDonald, "Magnetic domains in III-V magnetic semiconductors", *Phys. Rev. B* **64**, 241201 (2001a).

Dietl, T., H. Ohno, and F. Matsukura, "Hole-mediated ferromagnetism in tetrahedrally coordinated semiconductors", *Phys. Rev. B* **63**, 195205 (2001b).

Dietl, T., H. Ohno, F. Matsukura, J. Cibert, and D. Ferrand, "Zener model description of ferromagnetism in zinc-blende magnetic semiconductors", *Science* **287**, 1019–1022 (2000).

Edmonds, K. W., P. Bogusławski, K. Y. Wang, R. P. Campion, S. N. Novikov, N. R. S. Farley, B. L. Gallagher, C. T. Foxon, M. Sawicki, T. Dietl, M. Buongiorno Nardelli, and J. Bernholc, "Mn interstitial diffusion in (Ga,Mn)As", *Phys. Rev. Lett.* **92**, 037201 (2004).

Edmonds, K. W., N. R. S. Farley, T. K. Johal, G. van der Laan, R. P. Campion, B. L. Gallagher, and C. T. Foxon, "Ferromagnetic moment and antiferromagnetic coupling in (Ga,Mn)As thin films", *Phys. Rev. B* **71**, 064418–5 (2005).

Edmonds, K. W., K. Y. Wang, R. P. Campion, A. C. Neumann, N. R. S. Farley, B. L. Gallagher, and C. T. Foxon, "High-Curie-temperature $Ga_{1-x}Mn_xAs$ obtained by resistance-monitored annealing", *Appl. Phys. Lett.* **81**, 4991–4993 (2002a).

Edmonds, K. W., K. Y. Wang, R. P. Campion, A. C. Neumann, C. T. Foxon, B. L. Gallagher, and P. C. Main, "Hall effect and hole densities in $Ga_{1-x}Mn_xAs$", *Appl. Phys. Lett.* **81**, 3010–3012 (2002b).

Ekpunobi, A. J. and A. O. E. Animalu, "Band offsets and properties of AlGaAs/GaAs and AlGaN/GaN material systems", *Superlattices Microstruct.* **31**, 247–252 (2002).

Esch, A. Van, L. Van Bockstal, J. De Boeck, G. Verbanck, A. S. van Steenbergen, P. J. Wellmann, B. Grietens, R. Bogaerts, F. Herlach, and G. Borghs, "Interplay between the magnetic and transport properties in the III-V diluted magnetic semiconductor $Ga_{1-x}Mn_xAs$", *Phys. Rev. B* **56**, 13103 (1997).

Fernández-Rossier, J., R. Aguado, and L. Brey, "Anisotropic magnetoresistance in single electron transport", *Phys. Status Solidi C* **3**, 4231–4234 (2007).

Foxon, C. T., "Principles of molecular beam epitaxy", in *Handbook of Crystal Growth*, edited by Donald T. J. Hurle, 157–181 (Amsterdam: Elsevier, 1994).

Foxon, C. T. and B. A. Joyce, "Fundamental aspects of molecular beam epitaxy", in *Current Topics in Materials Science*, volume 7, edited by E. Kaldis, 3–68 (Amsterdam: North-Holland, 1981).

Fujita, J., Y. Ohnishi, Y. Ochiai, E. Nomura, and S. Matsui, "Nanometer-scale resolution of calixarene negative resist in electron beam lithography", *J. Vac. Sci. Technol. B* **14**, 4272–4276 (1996).

Fukumura, T., T. Shono, K. Inaba, T. Hasegawa, H. Koinuma, F. Matsukura, and H. Ohno, "Magnetic domain structure of a ferromagnetic semiconductor (Ga,Mn)As observed with scanning probe microscopes", *Physica E* **10**, 135–138 (2001).

Furdyna, J. K., "Diluted magnetic semiconductors", *J. Appl. Phys.* **64**, R29–R64 (1988).

Gao, Li, Xin Jiang, See-Hun Yang, J. D. Burton, Evgeny Y. Tsymbal, and Stuart S. P. Parkin, "Bias voltage dependence of tunneling anisotropic magnetoresistance in magnetic tunnel junctions with MgO and Al_2O_3 tunnel barriers", *Phys. Rev. Lett.* **99**, 226602 (2007).

García, N., M. Muñoz, and Y.-W. Zhao, "Magnetoresistance in excess of 200% in ballistic Ni nanocontacts at room temperature and 100 Oe", *Phys. Rev. Lett.* **82**, 2923–2926 (1999).

Giddings, A. D., T. Jungwirth, and B. L. Gallagher, "Interlayer exchange coupling in (Ga,Mn)As based multilayers", *Phys. Status Solidi C* **3**, 4070–4073 (2007).

Giddings, A. D., T. Jungwirth, and B. L Gallagher, "(Ga,Mn)As based superlattices and the search for antiferromagnetic interlayer coupling", *arXiv:0802.0275* (2008a).

Giddings, A. D., M. N. Khalid, T. Jungwirth, J. Wunderlich, S. Yasin, R. P. Campion, K. W. Edmonds, J. Sinova, K. Ito, K.-Y. Wang, D. Williams, B. L. Gallagher, and C. T. Foxon, "Large tunneling anisotropic magnetoresistance in (Ga,Mn)As nanoconstrictions", *Phys. Rev. Lett.* **94**, 127202 (2005).

Giddings, A. D., O. N. Makarovsky, M. N. Khalid, S. Yasin, K. W. Edmonds, R. P Campion, J. Wunderlich, T. Jungwirth, D. A. Williams, B. L. Gallagher, and C. T. Foxon, "Huge tunnelling anisotropic magnetoresistance in (Ga,Mn)As nanoconstrictions", *arXiv:0803.3416* (2008b).

Gould, C., K. Pappert, G. Schmidt, and L. W. Molenkamp, "Magnetic anisotropies and (Ga,Mn)As-based spintronic devices", *Adv. Mater.* **19**, 323–340 (2007).

Gould, C., C. Rüster, T. Jungwirth, E. Girgis, G. M. Schott, R. Giraud, K. Brunner, G. Schmidt, and L. W. Molenkamp, "Tunneling anisotropic magnetoresistance: A spin-valve-like tunnel magnetoresistance using a single magnetic layer", *Phys. Rev. Lett.* **93**, 117203 (2004).

Grandidier, B., J. P. Nys, C. Delerue, D. Stievenard, Y. Higo, and M. Tanaka, "Atomic-scale study of GaMnAs/GaAs layers", *Appl. Phys. Lett.* **77**, 4001–4003 (2000).

Griffiths, David J., *Introduction to Quantum Mechanics* (Upper Saddle River, NJ: Prentice Hall, 1995).

Gritz, Michael A, Meredith Metzler, Joel Moser, David Spencer, and Glenn D. Boreman, "Fabrication of air bridges using electron beam lithography", *J. Vac. Sci. Technol. B* **21**, 332–334 (2003).

Guan, Baolu, Xia Guo, Ting Liang, Xiaoling Gu, Jun Deng, Jing Guo, Hao Yang, Qiaoming Lin, and Guangdi Shen, "Sacrificial $Al_{0.8}Ga_{0.2}As$ etching for microstructures in integrated optoelectronic devices", *J. Appl. Phys.* **100**, 113508 (2006).

Gupta, J. A., R. Knobel, N. Samarth, and D. D. Awschalom, "Ultrafast manipulation of electron spin coherence", *Science* **292**, 2458–2461 (2001).

Hamaya, Kohei, Rai Moriya, Akira Oiwa, Tomoyasu Taniyama, Yoshitaka Kitamoto, Yohtaro Yamazaki, and Hiroo Munekata, "Contribution of shape anisotropy to the magnetic configuration of (Ga, Mn)As", *Jpn. J. Appl. Phys.* **43**, L306–L308 (2004).

Han, S-J., J. W. Song, C.-H. Yang, S. H. Park, J.-H. Park, Y. H. Jeong, and K. W. Rhie, "A key to room-temperature ferromagnetism in Fe-doped ZnO: PCu", *Appl. Phys. Lett.* **81**, 4212–4214 (2002).

Hayashi, T., M. Tanaka, K. Seto, T. Nishinaga, and K. Ando, "III-V based magnetic(GaMnAs)/nonmagnetic(AlAs) semiconductor superlattices", *Appl. Phys. Lett.* **71**, 1825–1827 (1997).

Hernandez, C., F. Terki, S. Charar, J. Sadowski, D. Maude, V. Stanciu, and P. Svedlindh, "Magnetic properties of GaMnAs single layers and GaInMnAs superlattices investigated at low temperature and high magnetic field", *Acta Phys. Pol. A* **103**, 613 (2001).

Hjort, Klas, "Sacrificial etching of III - V compounds for micromechanical devices", *J. Micromech. Microeng.* **6**, 370–375 (1996).

Holleitner, A. W., H. Knotz, R. C. Myers, A. C. Gossard, and D. D. Awschalom, "Manipulating a domain wall in (Ga,Mn)As", *J. Appl. Phys.* **97**, 10D314 (2005).

Honolka, J., S. Masmanidis, H. X. Tang, M. L. Roukes, and D. D. Awschalom, "Domain-wall dynamics at micropatterned constrictions in ferromagnetic (Ga,Mn)As epilayers", *J. Appl. Phys.* **97**, 063903 (2005).

Hua, Susan Z. and Harsh Deep Chopra, "100,000 % ballistic magnetoresistance in stable Ni nanocontacts at room temperature", *Phys. Rev. B* **67**, 060401 (2003).

Hwang, E. H. and S. Das Sarma, "Transport properties of diluted magnetic semiconductors: Dynamical mean-field theory and boltzmann theory", *Phys. Rev. B* **72**, 035210–15 (2005).

Jain, Manish, Leeor Kronik, James R. Chelikowsky, and Vitaliy V. Godlevsky, "Electronic structure and spin polarization of Mn-containing dilute magnetic III-V semiconductors", *Phys. Rev. B* **64**, 245205 (2001).

Jakiela, R., A. Barcz, E. Wegner, and A. Zagojski, "Diffusion of Mn in gallium arsenide", *J. Alloys Compd.* **423**, 132–135 (2006).

Jaoul, O., I. A. Campbell, and A. Fert, "Spontaneous resistivity anisotropy in Ni alloys", *J. Magn. Magn. Mat.* **5**, 23–34 (1977).

Joyce, B. A., J. H. Neave, J. Zhang, P. J. Dobson, P. Dawson, K. J. Moore, and C. T. Foxon, "Dynamic RHEED techniques and interface quality in MBE-grown GaAs/(Al,Ga)As structures", in *Thin Film Growth Techniques for Low-Dimensional Structures*, edited by R. F. C. Farrow, S. S. P. Parkin, P. J. Dobson, J. H. Neave, and A. S. Arrott, 19–36 (New York: Plenum Press, 1987).

Joyce, Bruce A. and Tim B. Joyce, "Basic studies of molecular beam epitaxy–past, present and some future directions", *J. Cryst. Growth* **264**, 605–619 (2004).

Jungwirth, T., M. Abolfath, Jairo Sinova, J. Kučera, and A. H. MacDonald, "Boltzmann theory of engineered anisotropic magnetoresistance in (Ga,Mn)As", *Appl. Phys. Lett.* **81**, 4029–4031 (2002a).

Jungwirth, T., W. A. Atkinson, B. H. Lee, and A. H. MacDonald, "Interlayer coupling in ferromagnetic semiconductor superlattices", *Phys. Rev. B* **59**, 9818–9821 (1999).

Jungwirth, T., Jürgen König, Jairo Sinova, J. Kučera, and A. H. MacDonald, "Curie temperature trends in (III,Mn)V ferromagnetic semiconductors", *Phys. Rev. B* **66**, 012402 (2002b).

Jungwirth, T., Jairo Sinova, J. Mašek, J. Kučera, and A. H. MacDonald, "Theory of ferromagnetic (III,Mn)V semiconductors", *Rev. Mod. Phys.* **78**, 809–864 (2006).

Jungwirth, T., Jairo Sinova, K. Y. Wang, K. W. Edmonds, R. P. Campion, B. L. Gallagher, C. T. Foxon, Qian Niu, and A. H. MacDonald, "Dc-transport properties of ferromagnetic (Ga,Mn)As semiconductors", *Appl. Phys. Lett.* **83**, 320–322 (2003).

Jungwirth, T., K. Y. Wang, J. Mašek, K. W. Edmonds, Jürgen König, Jairo Sinova, M. Polini, N. A. Goncharuk, A. H. MacDonald, M. Sawicki, R. P. Campion, L. X. Zhao, C. T. Foxon, and B. L. Gallagher, "Prospects of high temperature ferromagnetism in (Ga,Mn)As semiconductors", *Phys. Rev. B* **72**, 165204 (2005).

Kępa, H., J. Kutner-Pielaszek, J. Blinowski, A. Twardowski, C. F. Majkrzak, T. Story, P. Kacman, R. R. Gałazka, K. Ha, H. J. M. Swagten, W. J. M. de Jonge, A. Yu. Sipatov, V. Volobuev, and T. M. Giebultowicz, "Antiferromagnetic interlayer coupling in ferromagnetic semiconductor EuS/PbS(001) superlattices", *Europhys. Lett.* **56**, 54–60 (2001a).

Kępa, H., J. Kutner-Pielaszek, A. Twardowski, C. F. Majkrzak, J. Sadowski, T. Story, and T. M. Giebultowicz, "Ferromagnetism of GaMnAs studied by polarized neutron reflectometry", *Phys. Rev. B* **64**, 121302(R) (2001b).

Khalid, M. N., S. Yasin, A. D. Giddings, J. Wunderlich, R. Campion, K. Edmonds, C. T. Foxon, D. Walliams, and B. Gallagher, "Fabrication of nanoconstriction to study the change in magnetoresistance of a (Ga,Mn)As strip as a function of construction size", in *Digest of Papers: Microprocesses and Nanotechnology 2004*, 166–167 (Osaka, Japan: Japan Society of Applied Physics, 2004).

Kim, Jong-Hee, Dae Ho Lim, and Gye Mo Yang, "Selective etching of AlGaAs/GaAs structures using the solutions of citric acid/H_2O_2 and de-ionized H_2O/buffered oxide etch", *J. Vac. Sci. Technol. B* **16**, 558–560 (1998).

Kittel, C., "Indirect exchange interactions in metals", in *Solid State Physics: Advances in Research Applications*, volume 22, edited by Frederick Seitz, David Turnbull, and Henry Ehrenreich, 1–26 (New York: Academic Press, 1968).

König, J., J. Schliemann, T. Jungwirth, and A. MacDonald, "Ferromagnetism in (III,Mn)V semiconductors", in *Electronic Structure and Magnetism of Complex Materials*, edited by David J. Singh and Dimitrios A. Papaconstantopoulos, 1st edition, chapter 4, 163–212 (Berlin: Springer-Verlag, 2003).

König, Jürgen, T. Jungwirth, and A. H. MacDonald, "Theory of magnetic properties and spin-wave dispersion for ferromagnetic (Ga,Mn)As", *Phys. Rev. B* **64**, 184423 (2001).

Kretz, J., L. Dreeskornfeld, G. Ilicali, T. Lutz, and W. Weber, "Comparative study of calixarene and HSQ resist systems for the fabrication of sub-20 nm MOSFET device demonstrators", *Microelectron. Eng.* **78-79**, 479–483 (2005).

Ku, K. C., S. J. Potashnik, R. F. Wang, S. H. Chun, P. Schiffer, N. Samarth, M. J. Seong, A. Mascarenhas, E. Johnston-Halperin, R. C. Myers, A. C. Gossard, and D. D. Awschalom, "Highly enhanced Curie temperature in low-temperature annealed [Ga,Mn]As epilayers", *Appl. Phys. Lett.* **82**, 2302–2304 (2003).

Kuryliszyn-Kudelska, I., J. Z. Domagała, T. Wojtowicz, X. Liu, E. Łusakowska, W. Dobrowolski, and J. K. Furdyna, "Effect of Mn interstitials on the lattice parameter of $Ga_{1-x}Mn_xAs$", *J. Appl. Phys.* **95**, 603–608 (2004).

Lee, B., T. Jungwirth, and A. H. MacDonald, "Ferromagnetism in diluted magnetic semiconductor heterojunction systems", *Semicond. Sci. Technol.* **17**, 393–403 (2002).

Li, A. P., J. Shen, J. R. Thompson, and H. H. Weitering, "Ferromagnetic percolation in Mn_xGe_{1-x} dilute magnetic semiconductor", *Appl. Phys. Lett.* **86**, 152507 (2005).

Liu, X., Y. Sasaki, and J. K. Furdyna, "Ferromagnetic resonance in $Ga_{1-x}Mn_xAs$: Effects of magnetic anisotropy", *Phys. Rev. B* **67**, 205204 (2003).

López-Sancho, M. P. and L. Brey, "Temperature dependence of the dielectric constant and resistivity of diluted magnetic semiconductors", *Phys. Rev. B* **68**, 113201 (2003).

Matsukura, F., M. Sawicki, T. Dietl, D. Chiba, and H. Ohno, "Magnetotransport properties of metallic (Ga,Mn)As films with compressive and tensile strain", *Physica E* **21**, 1032–1036 (2004).

Matsumoto, K., M. Ishii, K. Segawa, Y. Oka, B. J. Vartanian, and J. S. Harris, "Room temperature operation of a single electron transistor made by the scanning tunneling microscope nanooxidation process for the TiO_x/Ti system", *Appl. Phys. Lett.* **68**, 34–36 (1996).

Matsumoto, Yuji, Makoto Murakami, Tomoji Shono, Tetsuya Hasegawa, Tomoteru Fukumura, Masashi Kawasaki, Parhat Ahmet, Toyohiro Chikyow, Shin ya Koshihara, and Hideomi Koinuma, "Room-temperature ferromagnetism in transparent transition metal-doped titanium dioxide", *Science* **291**, 854–856 (2001).

Mašek, J., J. Kudrnovský, and F. Máca, "Lattice constant in diluted magnetic semiconductors (Ga,Mn)As", *Phys. Rev. B* **67**, 153203 (2003).

Mašek, J., J. Kudrnovský, F. Máca, B. L. Gallagher, R. P. Campion, D. H. Gregory, and T. Jungwirth, "Dilute moment n-type ferromagnetic semiconductor Li(Zn,Mn)As", *Phys. Rev. Lett.* **98**, 067202 (2007a).

Mašek, J., J. Kudrnovský, F. Máca, and T. Jungwirth, "Interstitial Mn in (Ga,Mn)As: Hybridization with conduction band and electron mediated exchange coupling", *Acta Phys. Pol. A* **112**, 215 (2007b).

Mašek, J., J. Kudrnovský, F. Máca, Jairo Sinova, A. H. MacDonald, R. P. Campion, B. L. Gallagher, and T. Jungwirth, "Mn-doped Ga(As,P) and (Al,Ga)As ferromagnetic semiconductors: Electronic structure calculations", *Phys. Rev. B* **75**, 045202–7 (2007c).

McGuire, T. and R. Potter, "Anisotropic magnetoresistance in ferromagnetic 3*d* alloys", *IEEE Trans. Magn.* **11**, 1018–1038 (1975).

Mikkelsen, A., L. Ouattara, H. Davidsson, E. Lundgren, J. Sadowski, and O. Pacherova, "Mn diffusion in $Ga_{1-x}Mn_xAs$/GaAs superlattices", *Appl. Phys. Lett.* **85**, 4660–4662 (2004).

Munekata, H., H. Ohno, S. von Molnar, Armin Segmüller, L. L. Chang, and L. Esaki, "Diluted magnetic III-V semiconductors", *Phys. Rev. Lett.* **63**, 1849 (1989).

Nunez, V., T. M. Giebultowicz, W. Faschinger, G. Bauer, H. Sitter, and J. K. Furdyna, "Helical spin ordering and interlayer correlations in superlattices", *J. Magn. Magn. Mater.* **140-144**, 633–634 (1995).

Ochiai, Yukinori, Shoko Manako, Jun-ichi Fujita, and Eiichi Nomura, "High resolution organic resists for charged particle lithography", *J. Vac. Sci. Technol. B* **17**, 933–938 (1999).

Ohno, H., "Making nonmagnetic semiconductors ferromagnetic", *Science* **281**, 951–956 (1998).

Ohno, H., D. Chiba, F. Matsukura, T. Omiya, E. Abe, T. Dietl, Y. Ohno, and K. Ohtani, "Electric-field control of ferromagnetism", *Nature* **408**, 944–946 (2000).

Ohno, H., H. Munekata, T. Penney, S. von Molnár, and L. L. Chang, "Magnetotransport properties of *p*-type (In,Mn)As diluted magnetic III-V semiconductors", *Phys. Rev. Lett.* **68**, 2664 (1992).

Ohno, H., A. Shen, F. Matsukura, A. Oiwa, A. Endo, S. Katsumoto, and Y. Iye, "(Ga,Mn)As: A new diluted magnetic semiconductor based on GaAs", *Appl. Phys. Lett.* **69**, 363–365 (1996).

Ohno, Y., D. K. Young, B. Beschoten, F. Matsukura, H. Ohno, and D. D. Awschalom, "Electrical spin injection in a ferromagnetic semiconductor heterostructure", *Nature* **402**, 790–792 (1999).

Oiwa, A., S. Katsumoto, A. Endo, M. Hirasawa, Y. Iye, H. Ohno, F. Matsukura, A. Shen, and Y. Sugawara, "Nonmetal-metal-nonmetal transition and large negative magnetoresistance in (Ga, Mn)As/GaAs", *Solid State Commun.* **103**, 209–213 (1997).

Pappert, K., M. J. Schmidt, S. Hümpfner, C. Ruster, G. M. Schott, K. Brunner, C. Gould, G. Schmidt, and L. W. Molenkamp, "Magnetization-switched metal-insulator transition in a (Ga,Mn)As tunnel device", *Phys. Rev. Lett.* **97**, 186402 (2006).

Park, B. G., J. Wunderlich, D. A. Williams, S. J. Joo, K. Y. Jung, K. H. Shin, K. Olejnik, A. B. Shick, and T. Jungwirth, "Tunneling anisotropic magnetoresistance in multilayer-(Co/Pt)/AlO_x/Pt structures", *Phys. Rev. Lett.* **100**, 087204 (2008).

Peercy, Paul S., "The drive to miniaturization", *Nature* **406**, 1023–1026 (2000).

Pinto, N., L. Morresi, M. Ficcadenti, R. Murri, F. D'Orazio, F. Lucari, L. Boarino, and G. Amato, "Magnetic and electronic transport percolation in epitaxial $Ge_{1-x}Mn_x$ films", *Phys. Rev. B* **72**, 165203–7 (2005).

Potashnik, S. J., K. C. Ku, S. H. Chun, J. J. Berry, N. Samarth, and P. Schiffer, "Effects of annealing time on defect-controlled ferromagnetism in $Ga_{1-x}Mn_xAs$", *Appl. Phys. Lett.* **79**, 1495–1497 (2001).

Prinz, Gary A., "Magnetoelectronics", *Science* **282**, 1660–1663 (1998).

Reed, M. L., N. A. El-Masry, H. H. Stadelmaier, M. K. Ritums, M. J. Reed, C. A. Parker, J. C. Roberts, and S. M. Bedair, "Room temperature ferromagnetic properties of (Ga, Mn)N", *Appl. Phys. Lett.* **79**, 3473–3475 (2001).

Rehm, Ch., D. Nagengast, F. Klose, H. Maletta, and A. Weidinger, "Magnetic coupling in Fe/Nb multilayers: A neutron reflectivity study", *Europhys. Lett.* **38**, 61–72 (1997).

Rushforth, A. W., A. D. Giddings, K. W. Edmonds, R. P. Campion, C. T. Foxon, and B. L. Gallagher, "AMR and magnetometry studies of ultra thin GaMnAs films", *Phys. Status Solidi C* **3**, 4078–4081 (2007a).

Rushforth, A. W., K. Výborný, C. S. King, K. W. Edmonds, R. P. Campion, C. T. Foxon, J. Wunderlich, A. C. Irvine, P. Vašek, V. Novák, K. Olejník, Jairo Sinova, T. Jungwirth, and B. L. Gallagher, "Anisotropic magnetoresistance components in (Ga,Mn)As", *Phys. Rev. Lett.* **99**, 147207 (2007b).

Rüster, C., T. Borzenko, C. Gould, G. Schmidt, L. W. Molenkamp, X. Liu, T. J. Wojtowicz, J. K. Furdyna, Z. G. Yu, and M. E. Flatté, "Very large magnetoresistance in lateral ferromagnetic (Ga,Mn)As wires with nanoconstrictions", *Phys. Rev. Lett.* **91**, 216602 (2003).

Rüster, C., C. Gould, T. Jungwirth, J. Sinova, G. M. Schott, R. Giraud, K. Brunner, G. Schmidt, and L. W. Molenkamp, "Very large tunneling anisotropic magnetoresistance of a (Ga,Mn)As/GaAs/(Ga,Mn)As stack", *Phys. Rev. Lett.* **94**, 027203 (2005).

Sadowski, J. and J. Z. Domagala, "Influence of defects on the lattice constant of GaMnAs", *Phys. Rev. B* **69**, 075206 (2004).

Sadowski, J., J. Z. Domagala, J. Bak-Misiuk, S. Kolesnik, M. Sawicki, K. Swiatek, J. Kanski, L. Ilver, and V. Strom, "Structural and magnetic properties of molecular beam epitaxy grown GaMnAs layers", *J. Vac. Sci. Technol. B* **18**, 1697–1700 (2000).

Sadowski, J., R. Mathieu, P. Svedlindh, M. Karlsteen, J. Kanski, Y. Fu, J. T. Domagala, W. Szuszkiewicz, B. Hennion, D. K. Maude, R. Airey, and G. Hill, "Ferromagnetic GaMnAs/GaAs superlattices-MBE growth and magnetic properties", *Thin Solid Films* **412**, 122–128 (2002).

Sailer, H., A. Ruderisch, D. P. Kern, and V. Schurig, "Evaluation of calixarene – derivatives as high-resolution negative tone electron-beam resists", *J. Vac. Sci. Technol. B* **20**, 2958–2961 (2002).

Saito, H., V. Zayets, S. Yamagata, and K. Ando, "Room-temperature ferromagnetism in a II-VI diluted magnetic semiconductor $Zn_{1-x}Cr_xTe$", *Phys. Rev. Lett.* **90**, 207202 (2003).

Sankowski, P. and P. Kacman, "Interlayer exchange coupling in (Ga,Mn)As-based superlattices", *Phys. Rev. B* **71**, 201303(R) (2005).

Sarma, S. Das, E. H. Hwang, and A. Kaminski, "How to make semiconductors ferromagnetic: a first course on spintronics", *Solid State Commun.* **127**, 99–107 (2003).

Sawicki, M., F. Matsukura, A. Idziaszek, T. Dietl, G. M. Schott, C. Ruester, C. Gould, G. Karczewski, G. Schmidt, and L. W. Molenkamp, "Temperature dependent magnetic anisotropy in (Ga,Mn)As layers", *Phys. Rev. B* **70**, 245325 (2004).

Sawicki, M., K.-Y. Wang, K. W. Edmonds, R. P. Campion, C. R. Staddon, N. R. Farley, C. T. Foxon, E. Papis, E. Kamińska, A. Piotrowska, T. Dietl, and B. L. Gallagher, "In-plane uniaxial anisotropy rotations in (Ga,Mn)As thin films", *Phys. Rev. B* **71**, 121302 (2005).

Schlapps, Markus, Matthias Doeppe, Konrad Wagner, Matthias Reinwald, Werner Wegscheider, and Dieter Weiss, "Transport through (Ga,Mn)As nanoconstrictions", *Phys. Status Solidi A* **203**, 3597–3601 (2006).

Schulman, J. N. and T. C. McGill, "Electronic properties of the AlAs-GaAs (001) interface and superlattice", *Phys. Rev. B* **19**, 6341 (1979).

Sharma, Manish, Shan X. Wang, and Janice H. Nickel, "Inversion of spin polarization and tunneling magnetoresistance in spin-dependent tunneling junctions", *Phys. Rev. Lett.* **82**, 616 (1999).

Sharma, Parmanand, Amita Gupta, K. V. Rao, Frank J. Owens, Renu Sharma, Rajeev Ahuja, J. M. Osorio Guillen, Borje Johansson, and G. A. Gehring, "Ferromagnetism above room temperature in bulk and transparent thin films of Mn-doped ZnO", *Nat. Mater.* **2**, 673–677 (2003).

Shi, S.-F., K. I. Bolotin, F. Kuemmeth, and D. C. Ralph, "Temperature dependence of anisotropic magnetoresistance and atomic rearrangements in ferromagnetic metal break junctions", *Phys. Rev. B* **76**, 184438 (2007).

Shick, A. B., F. Máca, J. Mašek, and T. Jungwirth, "Prospect for room temperature tunneling anisotropic magnetoresistance effect: Density of states anisotropies in CoPt systems", *Phys. Rev. B* **73**, 024418 (2006).

Sinova, Jairo, T. Jungwirth, and John Černe, "Magneto-transport and magneto-optical properties of ferromagnetic (III,Mn)V semiconductors: a review", *Int. J. Mod. Phys. B* **18**, 1083–1118 (2004).

Slonczewski, J. C., "Current-driven excitation of magnetic multilayers", *J. Magn. Magn. Mater.* **159**, L1–L7 (1996).

Smith, H. I., "Fabrication techniques for surface-acoustic-wave and thin-film optical devices", *IEEE Proc.* **62**, 1361–1387 (1974).

Smith, R. A. and H. Ahmed, "Gate controlled Coulomb blockade effects in the conduction of a silicon quantum wire", *J. Appl. Phys.* **81**, 2699–2703 (1997).

Sørensen, B. S., P. E. Lindelof, J. Sadowski, R. Mathieu, and P. Svedlindh, "Effect of annealing on carrier density and Curie temperature in epitaxial (Ga,Mn)As thin films", *Appl. Phys. Lett.* **82**, 2287–2289 (2003).

Stern, M. B. and P. F. Liao, "Reactive ion etching of GaAs and InP using $SiCl_4$", *J. Vac. Sci. Technol. B* **1**, 1053–1055 (1983).

Sze, Simon M., *Physics of Semiconductor Devices*, 2nd edition (New York: Wiley-Interscience, 1981).

Szuszkiewicz, W., E. Dynowska, B. Hennion, F. Ott, M. Jouanne, and J. F. Morhange, "Interlayer exchange coupling in short period GaMnAs/GaAs superlattices", *Acta Phys. Pol. A* **100**, 335 (1998).

Takamura, K., F. Matsukura, D. Chiba, and H. Ohno, "Magnetic properties of (Al,Ga,Mn)As", *Appl. Phys. Lett.* **81**, 2590–2592 (2002).

Tanaka, M. and Y. Higo, "Large tunneling magnetoresistance in GaMnAs/AlAs/GaMnAs ferromagnetic semiconductor tunnel junctions", *Phys. Rev. Lett.* **87**, 026602 (2001).

Tang, H. X., R. K. Kawakami, D. D. Awschalom, and M. L. Roukes, "Giant planar Hall effect in epitaxial (Ga,Mn)As devices", *Phys. Rev. Lett.* **90**, 107201 (2003).

Tang, H. X., S. Masmanidis, R. K. Kawakami, D. D. Awschalom, and M. L. Roukes, "Negative intrinsic resistivity of an individual domain wall in epitaxial (Ga,Mn)As microdevices", *Nature* **431**, 52–56 (2004).

Taur, Yuan, D. A. Buchanan, Wei Chen, D. J. Frank, K. E. Ismail, Shih-Hsien Lo, G. A. Sai-Halasz, R. G. Viswanathan, H.-J. C. Wann, S. J. Wind, and Hon-Sum Wong, "CMOS scaling into the nanometer regime", *IEEE Proc.* **85**, 486–504 (1997).

Thomson, W., "On the electro-dynamic qualities of metals: Effects of magnetization on the electric conductivity of nickel and of iron", *Proc. R. Soc. Lond.* **8**, 546–550 (1857).

Vélu, E., C. Dupas, D. Renard, J. P. Renard, and J. Seiden, "Enhanced magnetoresistance of ultrathin $(Au/Co)_n$ multilayers with perpendicular anisotropy", *Phys. Rev. B* **37**, 668 (1988).

Vosko, S. H., L. Wilk, and M. Nusair, "Accurate spin-dependent electron liquid correlation energies for local spin density calculations: a critical analysis", *Can. J. Phys.* **58**, 1200 (1980).

Vurgaftman, I. and J. R. Meyer, "Curie-temperature enhancement in ferromagnetic semiconductor superlattices", *Phys. Rev. B* **64**, 245207 (2001).

Vurgaftman, I., J. R. Meyer, and L. R. Ram-Mohan, "Band parameters for III-V compound semiconductors and their alloys", *J. Appl. Phys.* **89**, 5815–5875 (2001).

Wang, K. Y., R. P. Campion, K. W. Edmonds, M. Sawicki, T. Dietl, C. T. Foxon, and B. L. Gallagher, "Magnetism in (Ga,Mn)As thin films with T_C up to 173K", in *Proceedings of the 27th International Conference on the Physics of Semiconductors*, volume 772, edited by José Menéndez and Chris G. Van de Walle, 333–334 (Flagstaff, AZ: AIP, 2005a).

Wang, K. Y., K. W. Edmonds, R. P. Campion, B. L. Gallagher, N. R. S. Farley, C. T. Foxon, M. Sawicki, P. Boguslawski, and T. Dietl, "Influence of the Mn interstitial on the magnetic and transport properties of (Ga,Mn)As", *J. Appl. Phys.* **95**, 6512–6514 (2004).

Wang, K.-Y., M. Sawicki, K. W. Edmonds, R. P. Campion, S. Maat, C. T. Foxon, B. L. Gallagher, and T. Dietl, "Spin reorientation transition in single-domain (Ga,Mn)As", *Phys. Rev. Lett.* **95**, 217204 (2005b).

Wenisch, J., C. Gould, L. Ebel, J. Storz, K. Pappert, M. J. Schmidt, C. Kumpf, G. Schmidt, K. Brunner, and L. W. Molenkamp, "Control of magnetic anisotropy in (Ga,Mn)As by lithography-induced strain relaxation", *Phys. Rev. Lett.* **99**, 077201 (2007).

Williams, Ralph E., *Modern GaAs Processing Methods*, 2nd edition (Boston: Artech House, 1990).

Wolf, S. A., D. D. Awschalom, R. A. Buhrman, J. M. Daughton, S. von Molnar, M. L. Roukes, A. Y. Chtchelkanova, and D. M. Treger, "Spintronics: A spin-based electronics vision for the future", *Science* **294**, 1488–1495 (2001).

Wunderlich, J., T. Jungwirth, B. Kaestner, A. C. Irvine, A. B. Shick, N. Stone, K.-Y. Wang, U. Rana, A. D. Giddings, C. T. Foxon, R. P. Campion, D. A.

Williams, and B. L. Gallagher, "Coulomb blockade anisotropic magnetoresistance effect in a (Ga,Mn)As single-electron transistor", *Phys. Rev. Lett.* **97**, 077201 (2006).

Yablonovitch, Eli, T. Gmitter, J. P. Harbison, and R. Bhat, "Extreme selectivity in the lift-off of epitaxial GaAs films", *Appl. Phys. Lett.* **51**, 2222–2224 (1987).

Yafet, Y., "Ruderman-Kittel-Kasuya-Yosida range function of a one-dimensional free-electron gas", *Phys. Rev. B* **36**, 3948 (1987).

Yamanouchi, M., D. Chiba, F. Matsukura, and H. Ohno, "Current-induced domain-wall switching in a ferromagnetic semiconductor structure", *Nature* **428**, 539–542 (2004).

Yasin, Shazia, M. N. Khalid, Y. Zhang, and D. G. Hasko, "UVIII for combined e-beam and optical exposure hybrid lithography", *Microelectron. Eng.* **78-79**, 47–50 (2005).

Yu, K. M., W. Walukiewicz, T. Wojtowicz, I. Kuryliszyn, X. Liu, Y. Sasaki, and J. K. Furdyna, "Effect of the location of Mn sites in ferromagnetic $Ga_{1-x}Mn_xAs$ on its Curie temperature", *Phys. Rev. B* **65**, 201303 (2002).

Yu, K. M., W. Walukiewicz, T. Wojtowicz, W. L. Lim, X. Liu, U. Bindley, M. Dobrowolska, and J. K. Furdyna, "Curie temperature limit in ferromagnetic $Ga_{1-x}Mn_xAs$", *Phys. Rev. B* **68**, 041308 (2003).

Zailer, I., J. E. F. Frost, V. Chabasseur-Molyneux, C. J. B. Ford, and M. Pepper, "Crosslinked PMMA as a high-resolution negative resist for electron beam lithography and applications for physics of low-dimensional structures", *Semicond. Sci. Technol.* **11**, 1235–1238 (1996).

Zener, C., "Interaction between the d shells in the transition metals", *Phys. Rev.* **81**, 440 (1951).

Zhao, L. X., R. P. Campion, P. F. Fewster, R. W. Martin, B. Ya Ber, A. P. Kovarsky, C. R. Staddon, K. Y. Wang, K. W. Edmonds, C. T. Foxon, and B. L. Gallagher, "Determination of the Mn concentration in GaMnAs", *Semicond. Sci. Technol.* **20**, 369–373 (2005a).

Zhao, L. X., C. R. Staddon, K. Y. Wang, K. W. Edmonds, R. P. Campion, B. L. Gallagher, and C. T. Foxon, "Intrinsic and extrinsic contributions to the lattice parameter of GaMnAs", *Appl. Phys. Lett.* **86**, 071902 (2005b).

Zhuravlev, M. Ye., E. Y. Tsymbal, S. S. Jaswal, A. V. Vedyayev, and B. Dieny, "Spin blockade in ferromagnetic nanocontacts", *Appl. Phys. Lett.* **83**, 3534–3536 (2003).

Zorin, A. B., F.-J. Ahlers, J. Niemeyer, T. Weimann, H. Wolf, V. A. Krupenin, and S. V. Lotkhov, "Background charge noise in metallic single-electron tunneling devices", *Phys. Rev. B* **53**, 13682 (1996).